

https://dspace.org/

Fine structure of the Isoscalar giant monopole resonance in 58Ni and 90Zr using alpha inelastic scattering at zero degrees

Moodley, Chane' Simone

2019

https://hdl.handle.net/10539/28815

Moodley, Chane Simone (2019) Fine structure of the Isoscalar Giant Monopole Resonance in 58Ni and 90Zr using alpha inelastic scattering at zero degrees, University of the Witwatersrand, Johannesburg, <http://hdl.handle.net/10539/28815>

Downloaded from a DSpace repository. https://dspace.org/

Fine structure of the Isoscalar Giant Monopole Resonance in ^{58}Ni and ^{90}Zr using alpha inelastic scattering at zero degrees

Chané Simone Moodley



UNIVERSITY OF THE
WITWATERSRAND,
JOHANNESBURG

A dissertation submitted to the Faculty of Science,
University of the Witwatersrand,
in fulfilment of the requirements for the degree of
Master of Science.

Johannesburg, 2019

Declaration

I, the undersigned, hereby declare that the work contained in this dissertation is my own original work. It is being submitted for the Degree of Master of Science at the University of the Witwatersrand, Johannesburg. In its entirety or in part, it has not previously been submitted for any degree or examination at any other institution.



Chané Simone Moodley

29 May 2019

Abstract

The last few decades have proved to be quite exciting in the field of nuclear-structure physics. High energy-resolution (≤ 30 keV) proton inelastic-scattering experiments have revealed that giant resonances carry fine structure as a signature of the damping mechanisms involved. For the first time, it is now possible to perform high energy-resolution (≤ 70 keV) experiments with intermediate-energy (specifically 200 MeV) alpha-particle inelastic-scattering reactions at zero degrees. This particular combination of the scattering angle and projectile was selected since it results in the preferential excitation of the Isoscalar Giant Monopole Resonance (ISGMR). These experiments were performed for a range of nuclei, including ^{24}Mg, ^{58}Ni, and ^{90}Zr, using the Separated Sector Cyclotron and the K600 magnetic spectrometer at the iThemba Laboratory for Accelerator Based Sciences. The data were extracted and extensive optimisation procedures were performed. Particle identification was carried out to obtain accurate spectra for the (α, α') reaction. Accurate focal-plane position spectra were obtained following the implementation of several techniques including, amongst others, the use of look-up-table offsets, and an angle calibration to convert the focal-plane angle to the scattering angle. Lineshape correction was performed to obtain the best-possible resolution. An instrumental-background subtraction was performed and the individual data files were offset to ensure the peak positions were aligned when the data were chained by isotope. ISGMR distributions were obtained for ^{58}Ni and ^{90}Zr. The data underwent a Discrete Wavelet Transform background subtraction to ensure a pure ISGMR distribution. The centroid and width of the resonance for both nuclei were

extracted. Continuous Wavelet Transforms (CWTs) were applied to the data in order to extract the characteristic energy scales. Theoretical calculations were analysed with the CWT so as to compare the theoretical and experimental energy scales. A good correspondence between theory and experiment was found, and a dominant damping mechanism was found for the ISGMR.

Dedication

for my father - when I lost you my world shattered,

I still haven't picked up the pieces. This one's for you dad.

Yani Moodley

24 September 1946 - 22 June 2018

"*Do not pray for an easy life, pray for the strength to endure a difficult one*"

– Bruce Lee

Acknowledgements

My principal supervisor Dr Iyabo Usman, thank you for sticking by me. Thank you for the support and guidance you have provided me with throughout this journey. As a woman in science you have taught me some valuable life lessons and ultimately played a vital role in shaping the type of researcher I would like to be one day.

Dr Lindsay Donaldson, thank you for providing round the clock technical support! You have no idea how your instant help and support has sustained my work through some rough patches. Thank you for believing in me even when I did not believe in myself. Thank you for providing me with chocolates and calming me down before presentations, without you I would be a nervous wreck. Thank you for reading my dissertation about a million times and for never getting frustrated with me. Not only are you an amazing supervisor but also a friend.

Professor John Carter, thank you for seeing the potential in me that I did not think existed. Thank you for supporting me, guiding me, continuously assisting me, and also thank you for telling me to remain strong. You have always remained calm even when I was panicking, and absorbed a lot of the frustration I would have otherwise had to face if you were not around. Words do not do justice to the amount of gratitude I have for all the help and support you have always provided me with. Thank you for always being available for questions, comments, and discussions. Thank you for getting me through this when I had given up.

To our collaborator Dr Nikolay Arsenyev, from the Joint Institute of Nuclear Research in Russia, thank you very much for providing me with the much needed theoretical calculations for this project. Thank you for always being open to any questions and discussions and for providing extremely valuable insight into the theoretical calculations and their correspondence to the experimental data.

Thank you to the Wits Nuclear Structure Research Group and the researchers at iThemba LABS. Particularly to Sunday Olorunfunmi, Pheladi Molema, Lerato Baloyi, Harshna Jivan, Luna Pellegri and Professor Elias Sideras-Haddad. Thank you for all the advice and support throughout my degree.

To Ntombi Kheswa, the iThemba LABS target maker, thank you for preparing all the targets required for this study.

I would like to acknowledge all the financial support I received throughout the duration of this degree. The NRF Masters Scholarship, the NRF Grantholders bursary, iThemba LABS top-up funding and the University of the Witwatersrand Postgraduate Merit Award.

To my mentors and confidants from other fields, who were always willing to lend an ear or to provide advice, thank you. Dr Deepak Kar, thank you for being proud of me even when I felt there was nothing to be proud of, your support, understanding and motivation played a huge role. Dr 'Maletšabisa Molapo, thank you for showing me compassion and understanding, thank you for always providing me with the support I needed and providing me with a strong, yet humble, woman researcher in my life. I aspire to be half the person that you are one day. Sibongile Gumede, thank you for listening to me, for letting me talk and cry. Thank you for being a constant in my life and always providing support. Naweed Khan, thank you for always letting me talk your ear off, for letting me get my frustrations out and for adapting to the volatility of my moods. Joan Byamugisha, you simply amaze me, thank you for the constant support, guidance and for always offering to be an extra pair of eyes.

You give me lots of hope!

To my best friends: Joyful Mdhluli, thank you is not enough. You always provided help and support. Thank you for being a constant! Trishan Gounden, my day one. You have been there through thick and thin, always encouraging and supporting me while also shouting at me, thank you for being a constant structure of support in my life.

Thank you to siblings; Malini, Devan, Vicky and Ross, you have always played a vital role in my life, thank you for the constant support. My pets have always played a huge role in my life and have always made me feel better, Max, Prince (who is sadly in heaven) and Mia so it is only fair that I acknowledge them as well.

Julian Govender, thank you for getting me through this! Thank you for getting frustrated for me all while sorting out the little things that I did not have time for. Thank you for standing by me and encouraging me to continue. Thank you for always listening, for staying up with me while I worked, for waking me up extra early, for driving me around and most importantly thank you for supporting me through one of the toughest times of my life. Thank you for never giving up on this degree or on me.

Mum, saying thank you is not enough. You've been through the worst that life has to offer and yet you still found the strength to encourage and support me. You constantly look after me and are always there to listen to me. Thank you from the bottom of my heart for everything that you do for me, getting me through this degree is just the tip of the iceberg.

Dad, even though you are no longer with us I felt your presence this entire time. It was you who provided me with the much needed strength to get to this point. You wanted to see this degree bear fruit and hopefully, with your blessings, it will. I love and miss you. Thank you!

Contents

List of Figures **xi**

List of Tables **xviii**

1 Introduction **1**

1.1 ^{90}Zr(α, α') and the ISGMR 3

1.2 ^{58}Ni(α, α') and the ISGMR 6

1.3 Present work 9

2 Theoretical considerations **11**

2.1 Basic theory of giant resonances 11

2.2 Damping of giant resonances 14

2.2.1 Width Γ of the resonance 14

2.3 Isoscalar Giant Monopole Resonance 16

2.3.1 ISGMR in different mass regions 18

2.3.1.1 ISGMR in light nuclei 19

2.3.1.2 ISGMR in medium mass nuclei 20

2.4 Choice of projectile 21

2.4.1 General α-particle considerations 21

2.4.2 Alpha-particle scattering 22

2.5 Rutherford approach 22

2.6 Theoretical model predictions 24

2.6.1 Random Phase Approximation (RPA) 25

2.6.2 Quasiparticle Random Phase Approximation (QRPA) . . 25

2.6.3 Phonon-phonon coupling 27

2.7 Distorted Wave Born Approximation (DWBA) and nuclear potentials 28

2.8 Fine structure . . . 31
2.9 Extraction of characteristic energy scales . . . 32
2.9.1 Continuous Wavelet Transform (CWT) . . . 34
2.9.2 Power spectrum . . . 35
2.9.3 Discrete Wavelet Transform (DWT) . . . 35
2.9.4 DWT background determination . . . 36

3 Experimental details, data extraction and optimisation 38
3.1 Accelerator facility . . . 39
3.2 K600 magnetic spectrometer . . . 41
3.2.1 Zero-degree mode of the K600 magnetic spectrometer . . . 42
3.2.2 Focal-plane detectors . . . 44
3.2.2.1 Multi-wire drift chambers . . . 44
3.2.2.2 Plastic scintillator detectors . . . 45
3.3 Data acquisition system and electronics . . . 46
3.4 Target preparation . . . 47
3.5 Experimental techniques and methods . . . 48
3.5.1 Kinematic correction . . . 48
3.5.2 Dispersion matching . . . 49
3.5.3 Faint-beam technique . . . 51
3.5.4 Background contributions . . . 51
3.5.4.1 Beam-related background . . . 52
3.5.4.2 Target-related background . . . 53
3.6 Data extraction . . . 54
3.6.1 Particle identification . . . 54
3.6.1.1 Time-Of-Flight selection . . . 54
3.6.2 MWDC data extraction . . . 57
3.6.2.1 MWDC operation and focal-plane position determination . . . 57
3.6.2.2 Position resolution . . . 60
3.6.2.3 MWDC efficiency . . . 60
3.6.2.4 Angle calibration . . . 61
3.7 Data optimisation . . . 63
3.7.1 Lineshape correction . . . 63

3.7.2 Background subtraction 68
3.7.3 Data offsets 74
3.7.4 Energy resolution 77
3.7.5 Energy calibration 78
3.7.5.1 Position-to-rigidity calibration 78
3.7.5.2 Rigidity-to-energy calibration 79
3.7.5.3 Excitation-energy spectra 80
3.7.6 Double-differential cross sections 82

4 Analysis of results and discussion **84**
4.1 Experimental data 85
4.2 Isoscalar Giant Monopole Resonance in ^{90}Zr 89
4.2.1 ^{90}Zr ISGMR distribution 89
4.2.2 Multipole decomposition and DOS method 90
4.2.3 ISGMR ^{90}Zr background subtraction, DOS and DWT . . 92
4.2.4 ISGMR width and centroid for ^{90}Zr 98
4.2.5 ^{90}Zr ISGMR fine structure 100
4.3 Isoscalar Giant Monopole Resonance in ^{58}Ni 105
4.3.1 ^{58}Ni ISGMR distribution 105
4.3.2 Multipole decomposition and DOS method 106
4.3.3 ISGMR ^{58}Ni background subtraction, DOS and DWT . . 106
4.3.4 ISGMR width and centroid for ^{58}Ni 108
4.3.5 ^{58}Ni ISGMR fine structure 109
4.4 Discussion 113

5 Conclusions **117**

References **119**

List of Figures

1.1 Hypothetical strength distributions and centroid energies for various giant resonances. The overlap of the different modes should be noted (taken from [7]). 3

1.2 Angular distributions for α-particle inelastic scattering from ^{90}Zr at an excitation energy of 16 MeV. The black solid line through the data (filled circles) shows the sum of various multipole components. The dash-dotted (red), dashed (brown), and dash-double-dotted (green) curves indicate contributions from $L = 0$, 1, and 2, respectively. The solid gray line shows the IVGDR component (taken from [10]). 5

1.3 *Upper*: Excitation-energy spectra measured at an average angle of 0.7° for ^{90}Zr, ^{92}Zr and ^{92}Mo. *Lower*: Difference spectra of angles 0.7° and 2.0° for the same nuclei (taken from [10]). 6

1.4 Excitation-energy spectrum for the ^{58}Ni(α, α') reaction at $E_\alpha =$ 386 MeV (taken from [13]). The black line corresponds to the intermingling of the ISGMR and the ISGQR while the blue line represents the intermingling of the ISGDR and the HEOR. . . . 7

1.5 Angular distributions of selected 1 MeV bins for the ^{58}Ni(α, α') reaction at 386 MeV. *Upper*: Results for $E_x = 18.5$ MeV. The open circles are the experimental data and the solid line is the Multipole Decomposition Analysis fit to the data. Also shown are the contributions from $L = 0$ (dotted line), $L = 1$ (dashed line), $L = 2$ (dot-dashed line), $L = 3$ (double-dot-dashed line), and other higher-multipole components, including the IVGDR (double-dash-dotted line), respectively. *Lower*: Same as the upper panel, except for $E_x = 29.5$ MeV (taken from [13]). 8

2.1 A schematic illustration of the different oscillation modes of a nucleus (taken from [7]). 12

2.2 A schematic illustration of the electric multipole transitions between states of the shell model of a hypothetical nucleus (taken from [14]). 14

2.3 Giant-resonance spectra for the inelastic-scattering reaction of 120 MeV α particles at scattering angles of 12° and 14° for ^{208}Pb (taken from [4]). 17

2.4 Alpha inelastic-scattering spectra for ^{24}Mg with $E_\alpha = 120$ MeV at small scattering angles (taken from [30]). 20

2.5 A schematic representation of the Coulomb-excitation process. . 24

2.6 Wavelet functions used in this study. *Left*: Complex-Morlet Mother wavelet used for CWT. Both real (*upper*) and imaginary (*lower*) parts are shown. *Right*: Biorthogonal level 6.8 Mother wavelet used for DWT. Both the decomposition (*upper*) and reconstruction (*lower*) functions are shown (taken from [45]). . . 34

2.7 A schematic representation of the DWT. Band-pass filters are applied so that the signal is decomposed into components of various frequencies (taken from [45]). 37

3.1 Schematic diagram of the layout of iThemba LABS showing the ECR, SPC1, SPC2, the SSC, and the K600 magnetic spectrometer as well as the isotope production and radiotherapy vaults. The enlarged section illustrates the position of the object slit 9X, the emittance slit 12X and the energy-definition slit 1P. . . 40
3.2 Schematic diagram of the K600 magnetic spectrometer at iThemba LABS [62]. 42
3.3 Schematic diagram of the zero-degree facility of the K600 magnetic spectrometer (taken from [3]). 43
3.4 Schematic diagram of the three different dispersion-matching modes (taken from [71]). 50
3.5 Time-Of-Flight before particle identification for particles of interest in ^{24}Mg. 55
3.6 The pulse height in paddle 1 plotted as a function of Time-Of-Flight (ns). The black line indicates the selected region of interest for ^{24}Mg(α, α') 56
3.7 Time-Of-Flight (ns) plotted as a function of x_{fp} (mm). The black line indicates the selected region of interest for ^{24}Mg(α, α') 57
3.8 Two-dimensional resolution spectra before (*upper*) and after (*lower*) LUT offsets for U1. 59
3.9 θ_{fp} plotted as a function of x_{fp} (mm) used for the reconstruction of the horizontal scattering angle (θ_{scat}). 62
3.10 The conversion of focal-plane angle (θ_{fp}) to scattering angle (θ_{scat}) for spectra with different focal-plane positions. 63
3.11 *Left*: The slope as a function of the focal-plane position (x_{fp}). *Right*: The offset as a function of the focal-plane position (x_{fp}). 63
3.12 The points used to reproduce the lineshape of a chosen state. The fit parameters are given in the bottom-right corner. 65

3.13 The effect of lineshape correction. *Upper*: Prominent excited states in the $x_{\rm fp}$ *versus* $\theta_{\rm scat}$ scatterplot with no lineshape correction applied. *Lower*: The scatterplot of the prominent excited states after the application of the lineshape correction. 66
3.14 *Upper*: Focal-plane position spectrum before lineshape correction for ^{24}Mg. *Lower*: Focal-plane position spectrum after the application of the lineshape correction for ^{24}Mg. 67
3.15 *Upper*: The two-dimensional $x_{\rm fp}$ (mm) *versus* $y_{\rm fp}$ (mm) scatterplot for the calibration target ^{24}Mg. *Lower*: The $y_{\rm fp}$ projection of the focal-plane events show a shift owing to a change in the vertical beam position on the target. 70
3.16 *Upper*: The two-dimensional $x_{\rm fp}$ (mm) *versus* $y_{\rm fp}$ (mm) scatterplot for ^{58}Ni. *Lower*: The $y_{\rm fp}$ projection of the focal-plane events show a shift owing to a change in the vertical beam position on the target. 71
3.17 *Upper*: The two-dimensional $x_{\rm fp}$ (mm) *versus* $y_{\rm fp}$ (mm) scatterplot for ^{90}Zr. *Lower*: The $y_{\rm fp}$ projection of the focal-plane events show events of interest centered around $y_{\rm fp} = 0$. 72
3.18 The focal-plane position spectra showing the components involved in the background-subtraction procedure. *Upper*: ^{58}Ni. *Lower*: ^{90}Zr 73
3.19 The background-subtracted focal-plane position spectrum for ^{24}Mg after the application of the lineshape correction 74
3.20 The focal-plane position spectrum without position and TOF offsets for ^{24}Mg. 76
3.21 The focal-plane position spectrum with both position and TOF offsets for ^{24}Mg. 76
3.22 An example of a Gaussian-plus-polynomial fit of the most-prominent peak in calibration target ^{24}Mg. 77
3.23 The rigidity calibration curve. 79

3.24 The calibrated excitation-energy spectrum for ^{24}Mg (*upper*); A magnification of the identified states (*lower*). 81

4.1 Excitation-energy spectra for α-particle inelastic scattering at $E_\alpha = 200$ MeV for ^{24}Mg (*upper*), ^{58}Ni (*middle*), and ^{90}Zr (*lower*). Measurements were taken at $\theta_{\rm lab} = 0^\circ$ where the cross section of the ISGMR is at a maximum. 87

4.2 Excitation energy (MeV) *versus* double-differential cross section (mb/sr MeV) for α-particle inelastic scattering at $E_\alpha = 200$ MeV for ^{24}Mg (*upper*), ^{58}Ni (*middle*), and ^{90}Zr (*lower*). . . 88

4.3 Multipole Decomposition Analysis: angular distributions for DWBA α-particle inelastic scattering on ^{90}Zr(α, α'). *Upper*: $E_\alpha = 385$ MeV. *Lower*: $E_\alpha = 200$ MeV. 91

4.4 Excitation-energy spectrum of ^{90}Zr(α, α') at E$_\alpha = 385$ MeV. See upper panel of Fig. 1.3 (data obtained from the NNDC [83]). . . 94

4.5 DWT background subtraction of the non-resonant component for the ^{90}Zr(α, α') at $E_\alpha = 385$ MeV excitation-energy spectrum. *Upper*: Spectrum containing background components taken from [83] and then limited to the 10-25 MeV excitation-energy range. *Middle*: DWT background contribution. *Lower*: DWT background-subtracted excitation-energy spectrum. 95

4.6 Decomposition of the ^{90}Zr(α, α') excitation-energy spectrum at $E_\alpha = 385$ MeV into approximations (A_i) and details (D_i), where i represents the integers from 1 to 7. 96

4.7 DWT background subtraction of the non-resonant component for the ^{90}Zr(α, α') at $E_\alpha = 200$ MeV excitation-energy spectrum. *Upper*: Spectrum containing background components. *Middle*: DWT background contribution. *Lower*: DWT background-subtracted excitation-energy spectrum. 97

4.8 Decomposition of the ^{90}Zr(α, α') excitation energy spectrum at $E_\alpha = 200$ MeV into approximations (A_i) and details (D_i), where i represents the integers from 1 to 10. 98
4.9 DWT background-subtracted excitation-energy spectra for ^{90}Zr showing the application of a Lorentzian curve fit (green). 99
4.10 *Upper*: Experimental excitation-energy spectra for ^{90}Zr at $E_\alpha = 200$ MeV. *Lower*: Solid line represents PPC strength distribution, filled circles represent data from Gupta et al. [10], dashed line represents the results of QRPA. 102
4.11 Experimental and theoretical CWT analysis for ^{90}Zr between the excitation-energy region of 12.5 - 19.5 MeV. Red arrows indicate the presence of equivalent scales. 103
4.12 Experimental and theoretical CWT analysis for ^{90}Zr between the excitation-energy region of 19.5 - 25 MeV. Red arrows indicate the presence of equivalent scales. 104
4.13 DWT background subtraction of the non-resonant component for the ^{58}Ni(α, α') at $E_\alpha = 200$ MeV excitation-energy spectrum. Upper: Spectrum containing background components. Middle: DWT background contribution. Lower: DWT background-subtracted excitation-energy spectrum. 107
4.14 Decomposition of the ^{58}Ni(α, α') excitation-energy spectrum at $E_\alpha = 200$ MeV into approximations (A_i) and details (D_i) where i represents the integers from 1 to 10. 108
4.15 DWT background-subtracted excitation-energy spectra for ^{58}Ni showing the application of a Lorentzian curve fit (green). . . . 109
4.16 *Upper*: Experimental excitation-energy spectra for ^{58}Ni at $E_\alpha = 200$ MeV. *Lower*: Solid line represents PPC strength distribution, filled circles represent data from Nayak et al. [13], dashed line represents the results of QRPA. 111

4.17 Experimental and theoretical CWT analysis for ^{58}Ni between the excitation-energy region of 12 - 23 MeV. Red arrows indicate the presence of equivalent scales. 112

List of Tables

3.1 Details of targets used in this study 48

3.2 Position and energy resolutions for the isotopes associated with the ^{24}Mg calibration target 78

3.3 A comparison of the energy values obtained in this work and those that are well documented for ^{24}Mg. 80

4.1 Optical model potential parameters for ^{90}Zr(α, α') calculated using the method of Kumar and Kailas [80] using the code OM-Alpha [81]. The parameters refer to the real and imaginary Woods-Saxon volume potentials presented in Section 2.7. 92

4.2 Experimentally extracted centroids and widths of the ISGMR for ^{90}Zr. 99

4.3 Characteristic energy scales of the ISGMR for ^{90}Zr: 12.5 - 19.5 MeV. The numbers in red correspond to the red arrows in Fig. 4.11 indicating the corresponding scales. 105

4.4 Characteristic energy scales for $E0$ strength above the ISGMR for ^{90}Zr: 19.5 - 25 MeV. The numbers in red correspond to the red arrows in Fig. 4.12 indicating the corresponding scales. . . . 105

4.5 Experimentally extracted centroids and widths of the ISGMR for ^{58}Ni. 109

4.6 Characteristic energy scales of the ISGMR for ^{58}Ni. The numbers in red correspond to the red arrows in Fig. 4.17 indicating the corresponding scales. 113

Chapter 1

Introduction

The ground- and excited-state properties of atomic nuclei are yet to be understood in their entirety even though the strong and weak nuclear forces have been investigated extensively over the past few decades. Considerable effort has been made to establish a confluence of experimental and theoretical efforts. Advances have been made at state-of-the-art experimental facilities while the growth in computational power has allowed for complex calculations to be solved or, at the very least, to reveal where gaps in knowledge exist.

Much attention has been given to nuclear giant resonances, which are small-amplitude, high-frequency, simple collective modes of excitation of nuclei [1]. A study into the properties of giant resonances provides information about the bulk properties of the nucleus as well as the non-equilibrium dynamics [2, 3]. The Isoscalar Giant Monopole Resonance (ISGMR) was first directly observed with the inelastic scattering of 120 MeV alpha (α) particles on a ^{208}Pb target in 1997 [4]. The existence of this resonance was then confirmed with the use of α-particle inelastic scattering measurements at very-forward scattering angles [5]. The ISGMR is the focus of this study and will be discussed in depth in the sections to follow.

Giant resonances correlate to a collective motion of many (if not all) particles

within a nucleus and are a common occurrence of many-body quantum systems [1, 6]. Quantum mechanically, a resonance is seen as a transition that occurs between the ground-state and the collective-state of the nucleus [1]. The transition amplitude describes the transition strength, which is dependent on the basic properties of the system, including the size of the system as well as the number of particles that participate in the response of the system [1, 6]. A well-established method to study the properties of the system is to subject the system to a weak perturbation and measure the response of the system [1].

It is important to note that the total transition strength is restricted by what is known as a sum rule. The sum rule is again dependent on the ground-state properties of the nucleus. If more than 50% of the Energy-Weighted Sum Rule (EWSR) is exhausted by a resonance, the resonance is referred to as a Giant Resonance (GR) [1, 7].

Giant resonances are also described as a coherent superposition of particle-hole excitations and, as such, if the nuclear shell model is considered, the single-particle wave functions of successive states carry opposite polarity [7]. The lowest excitations correspond to rearrangements and transitions between the highest unoccupied major shell and the ground state and, therefore, are only possible in open-shell nuclei [8]. However, it is important to note residual particle-hole (p-h) interactions give rise to a strong collective state. For a given multipolarity (and parity), this collective state is coherently a superposition of all possible particle-hole interactions [7]. The p-h residual interaction is positive for isoscalar transitions and repulsive for isovector excitations [7]. This results in an excitation-energy overlap of the various resonances as shown in Fig. 1.1. The large resonance widths arise from the mixing of the simple collective 1p-1h state with more complex 2p-2h states of the same spin and parity [1, 7]. It should be noted that the ISGMR, the so-called "breathing mode" is a second-order effect. To first-order, the transition operator for the ISGMR is a constant and can, therefore, not induce any ground- to excited-state transitions.

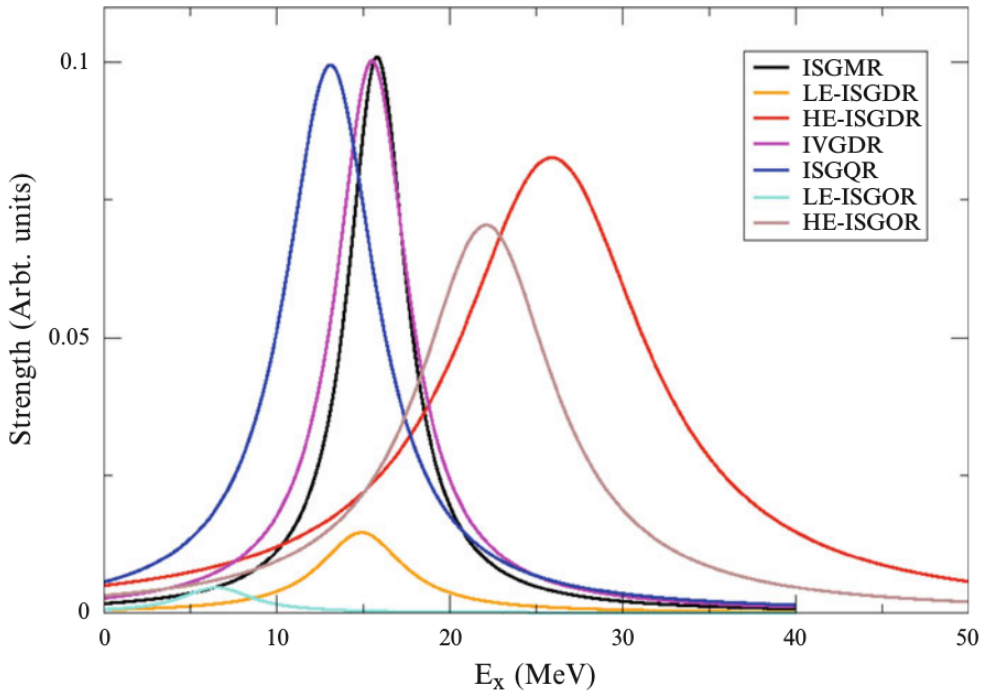

Figure 1.1: Hypothetical strength distributions and centroid energies for various giant resonances. The overlap of the different modes should be noted (taken from [7]).

In order to study a specific GR, the choice of probe (projectile) is extremely important as it determines the mode that will be excited during the reaction. The choice of projectile for this particular study is detailed in Chapter 2.

1.1 ^{90}Zr(α, α') and the ISGMR

Youngblood et al. [9] studied the ISGMRs in ^{90,92,94}Zr and ^{92,96,98,100}Mo with the inelastic scattering of 240 MeV α particles at small scattering angles including zero degrees, while Gupta et al. [10], conducted a similar study using a beam energy of 385 MeV in ^{90,92}Zr and ^{92}Mo. In Ref. [9], it was claimed that "the ISGMR strength distributions vary in a rather dramatic manner in nuclei in the A $\sim$ 90 region". However, Ref. [10] established that the strength distributions for the nuclei investigated coincide with each other, pointing to an unsatisfactory background subtraction in Ref. [9] to the measured experi-

mental excitation energy spectra. Coinciding strength distributions establish clearly that the nuclear incompressibility is not influenced by the nuclear shell structure near $A \sim 90$ [10]. Additionally, Gupta et al. [10], using the Distorted-Born Wave Approximation (DWBA) calculated $^{90}\mathrm{Zr}(\alpha, \alpha')$ inelastic scattering for low-order L-transfers at the maximum of the ISGMR ($E_\mathrm{x} = 16$ MeV) to produce what is called a multipole decomposition of the measured inelastic-scattering cross section (see Fig. 1.2). In Gupta et al. [10], calculated cross sections for different multipoles, and the linear combinations thereof, are used to express the experimental cross sections as follows:

$$\frac{d^2\sigma^{\mathrm{exp}}\left(\theta_{\mathrm{c.m.}}, E_\mathrm{x}\right)}{d\Omega dE} = \sum_{L=0}^{6} a_L\left(E_\mathrm{x}\right) \frac{d^2\sigma_L^{\mathrm{DWBA}}\left(\theta_{\mathrm{c.m.}}, E_\mathrm{x}\right)}{d\Omega dE}, \tag{1.1}$$

where the EWSR fraction, $a_L\left(E_\mathrm{x}\right)$, for the Lth component and the calculated DWBA cross section correspond to 100% of the EWSR for multipole L at specified excitation energy, E_x [10]. It should be noted that the fitted $a_L\left(E_\mathrm{x}\right)$ can, in turn, be related to the strengths, $S_L\left(E_\mathrm{x}\right)$.

Crucially in Ref. [10] identical ISGMR responses were found in the nuclei ^{90}Zr, ^{92}Zr and ^{92}Mo investigated thus revealing no influence of open or closed shells for protons or neutrons on the ISGMR [10]. Figure 1.3 shows the excitation-energy spectra at $\theta_{\mathrm{avg}} = 0.7^\circ$ (upper) and the "difference spectrum" (lower) for all nuclei under investigation. The difference spectrum is obtained by subtracting the inelastic-scattering spectrum at the first minimum for $L = 2$ from that of the 0° spectrum [10]. This is done at a point where the ISGMR strength is at a maximum and is, therefore, representative of only the ISGMR strength. The use of the "difference spectrum" technique allows for the background contributions of other multipolarities (which are uniformly flat close to 0°) to be subtracted. Gupta et al. [10] reported a centroid energy of 16.55 MeV, while the width of the resonance was reported to be 4.2 MeV.

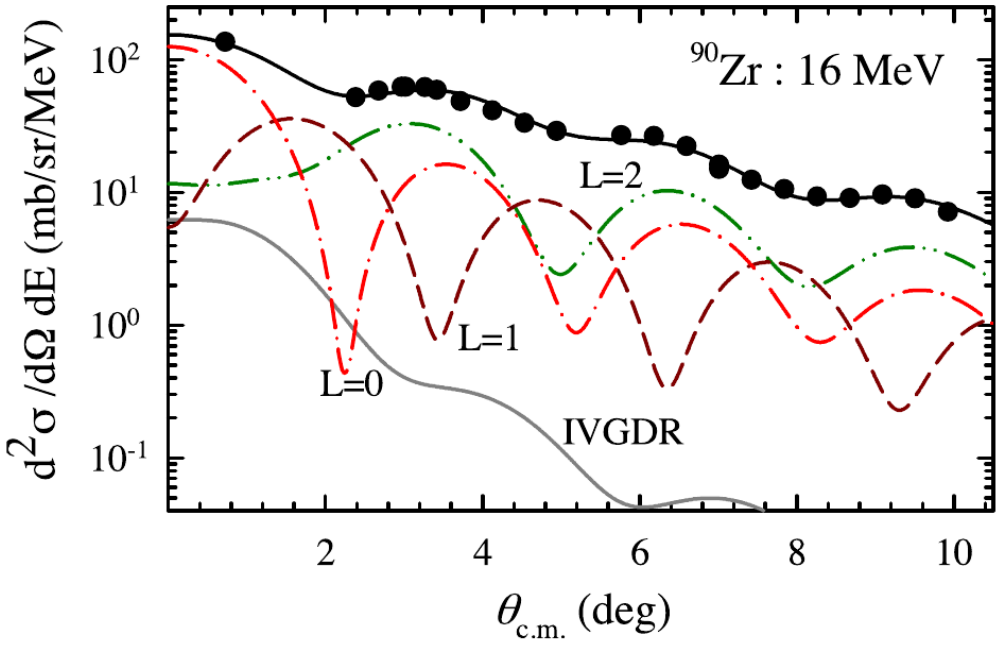

Figure 1.2: Angular distributions for α-particle inelastic scattering from ^{90}Zr at an excitation energy of 16 MeV. The black solid line through the data (filled circles) shows the sum of various multipole components. The dash-dotted (red), dashed (brown), and dash-double-dotted (green) curves indicate contributions from $L = 0$, 1, and 2, respectively. The solid gray line shows the IVGDR component (taken from [10]).

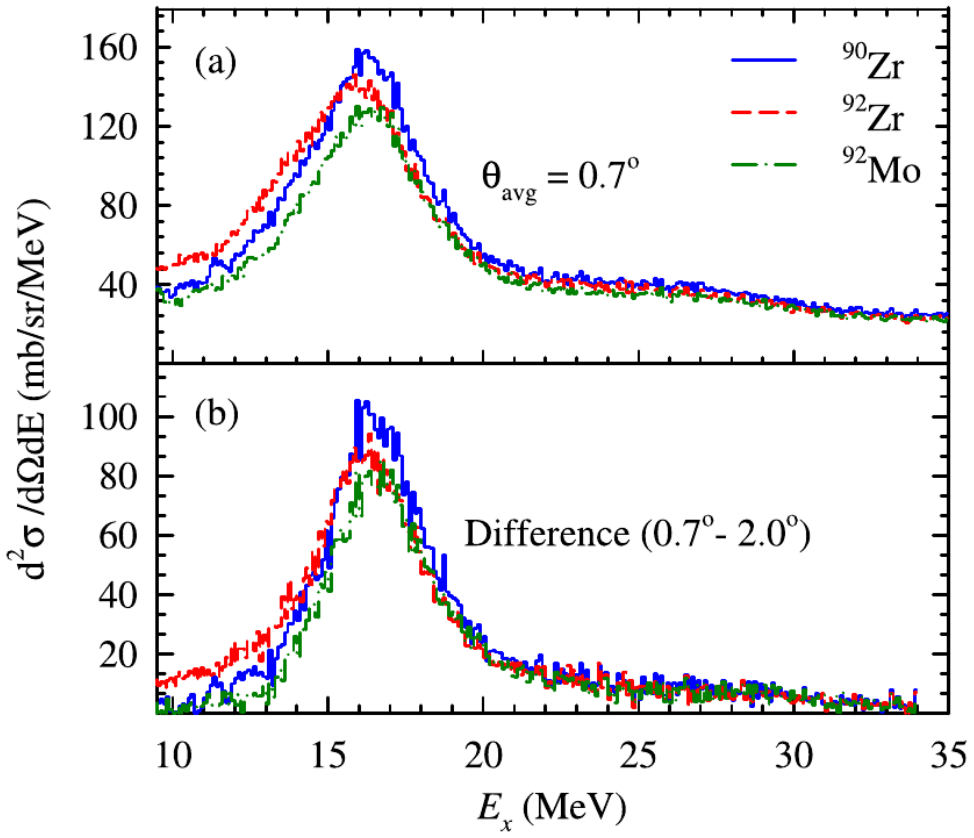

Figure 1.3: *Upper*: Excitation-energy spectra measured at an average angle of 0.7° for ^{90}Zr, ^{92}Zr and ^{92}Mo. *Lower*: Difference spectra of angles 0.7° and 2.0° for the same nuclei (taken from [10]).

1.2 ^{58}Ni(α, α') and the ISGMR

Studies of the excitation of the ISGMR in ^{58}Ni have been conducted using 129 MeV and 240 MeV α-particle inelastic-scattering reactions [11, 12], respectively. Exciting the ISGMR as well as extracting its strength was the focus with a multipole decomposition technique being used [12]. Based on cross-section analysis [12], nearly 100% of the EWSR is present in ^{58}Ni below 40 MeV excitation energy and there exists a significant difference between the theoretical and experimental EWSR [12].

Nayak et al. [13] studied the strength distribution of the Isoscalar Giant Dipole

Resonance (ISGDR) in ^{58}Ni over an excitation-energy range of 10.5 - 49.5 MeV via extreme forward-angle scattering of 386 MeV α particles. A "bi-modal" strength distribution of the ISGDR was observed in an $A < 90$ nucleus for the first time [13]. Figure 1.4 shows the excitation-energy spectrum for the ^{58}Ni(α, α') reaction. A prominent peak corresponding to the intermingling of the ISGMR and the Isoscalar Giant Quandrupole Resonance (ISGQR) is observed between 10 MeV and 25 MeV. The ISGDR and the High-Energy Octupole Resonance (HEOR) intermingling can be see as a shoulder at 33 MeV [13]. DWBA calculations were performed for various multipoles and can be seen in Fig. 1.5 with a distinct resemblance to the ISGMR results for ^{90}Zr (see Fig. 1.2).

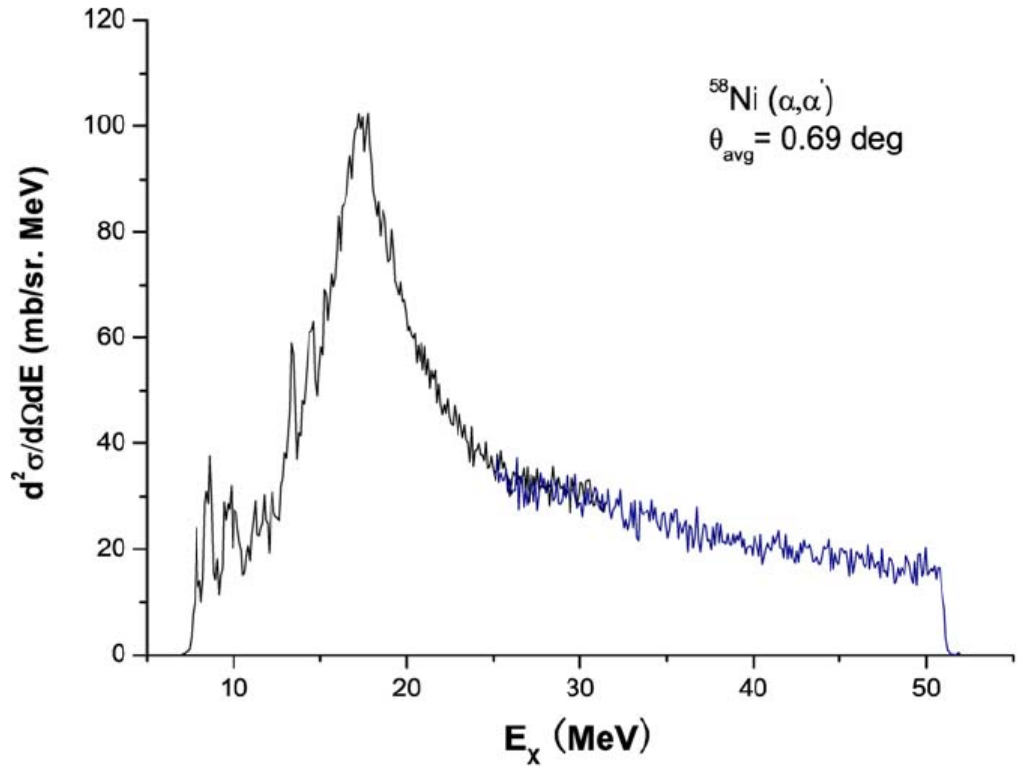

Figure 1.4: Excitation-energy spectrum for the ^{58}Ni(α, α') reaction at $E_\alpha =$ 386 MeV (taken from [13]). The black line corresponds to the intermingling of the ISGMR and the ISGQR while the blue line represents the intermingling of the ISGDR and the HEOR.

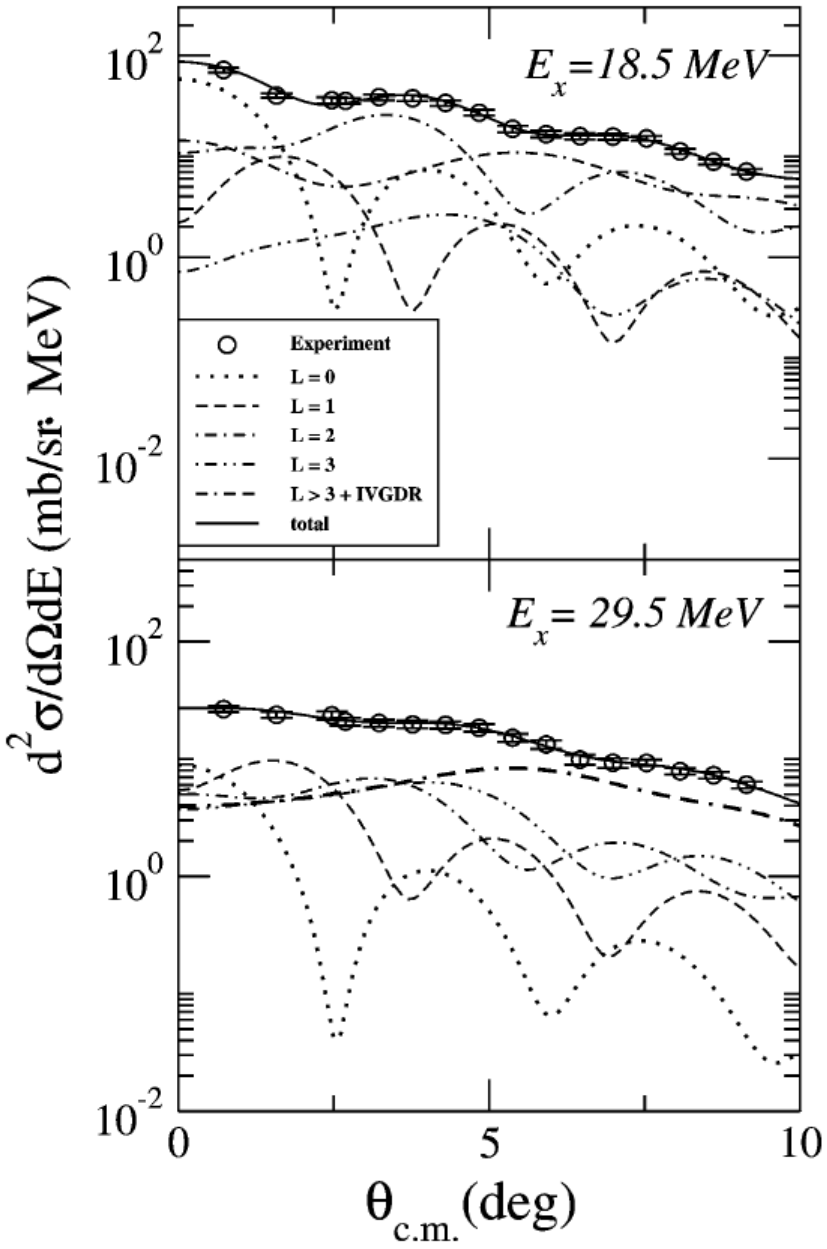

Figure 1.5: Angular distributions of selected 1 MeV bins for the ^{58}Ni(α, α') reaction at 386 MeV. *Upper*: Results for E_x = 18.5 MeV. The open circles are the experimental data and the solid line is the Multipole Decomposition Analysis fit to the data. Also shown are the contributions from $L = 0$ (dotted line), $L = 1$ (dashed line), $L = 2$ (dot-dashed line), $L = 3$ (double-dot-dashed line), and other higher-multipole components, including the IVGDR (double-dash-dotted line), respectively. *Lower*: Same as the upper panel, except for E_x = 29.5 MeV (taken from [13]).

1.3 Present work

This study investigated the ISGMR in ^{58}Ni and ^{90}Zr excited by inelastic scattering with 200 MeV alpha particles at extreme forward scattering angles (at and close to zero degrees) by achieving the following:

- obtain instrumental-background-free spectra with high energy-resolution,
- carry out multipole decomposition DWBA calculations,
- provide an alternative to the difference spectrum technique since only zero-degree data are available,
- extract the width and centroid of the ISGMR,
- establish whether the nuclei of interest carry fine structure in the ISGMR region, and
- extract the characteristic energy scales.

Observation of the ISGMR compression mode of nuclear excitation is of high significance because extraction of the $L = 0\hbar$ strength distributions for the ISGMR and their centroid energies can elucidate the incompressibility of nuclear matter in the aforementioned nuclei. In the present project, since only zero-degree data are available, a method equivalent to the Difference of Spectra technique was developed. The Discrete Wavelet Transform (DWT) background-subtraction technique subsequently allows for a reliable extraction of the centroid and width of the ISGMR. In addition, since multipole decomposition and the Difference of Spectra technique require experimental excitation-energy spectra to be re-binned to about 1 MeV (see extracted multipole strength distributions for ^{90}Zr in Fig. 1.3 [10] and in Fig. 1.4 for ^{58}Ni [13]) , no attention has been paid to possible fine structure in the original data measured. In contrast, the present project reports, importantly, for the first time for the IS-

GMR, extraction of energy scales from high energy-resolution (α, α') scattering leading to a better understanding of damping mechanisms by comparison with latest theoretical calculations.

The layout of this dissertation is as follows:

Chapter 2 provides an overview of the necessary theoretical considerations in the study of giant resonances and, in particular, the ISGMR. The chosen projectile and the causes of fine-structure presence are briefly presented. The theoretical considerations required for the wavelet-analysis procedure are also discussed.

Chapter 3 provides information related to the experimental equipment as well as the step-by-step data-extraction and data-optimisation processes.

Chapter 4 presents the experimental results from the data-extraction process. The results, following a Discrete Wavelet Transform background subtraction and further analysis using the Continuous Wavelet Transform technique, are also presented here, and are subsequently compared to state-of-the-art theoretical calculations for $E0$ strength and the ISGMR.

Chapter 5 presents the conclusions that can be drawn from the present study.

Chapter 2

Theoretical considerations

2.1 Basic theory of giant resonances

The atomic nucleus is a complicated, many-body quantum system that displays a large variety of excitations and a richer spectrum of collective modes than other quantum systems in physics [1, 8]. The nucleons, which are contained within the nucleus, undergo various collective oscillations or vibrations. Giant resonances can be defined as small-amplitude, high-frequency, simple collective modes of excitation [6, 14]. If approached from a hydrodynamic perspective, the degree of the collective motion of the nucleons is such that the modes of excitation can be studied as an oscillating liquid drop [1, 14].

Figure 2.1 illustrates several modes of oscillation of the nucleus that are classified primarily by the angular-momentum quantum number L [1, 8]. Referring to the electric resonances, the monopole mode is a spherically symmetric compression or oscillation of the nucleus $L = 0\hbar$ [14] being the Isoscalar Giant Monopole Resonance (ISGMR) investigated in this project. The well-known and the first to be identified as nuclear resonance, the Isovector Giant Dipole Resonance (IVGDR), for which $L = 1\hbar$, can be described as the motion in which the neutrons and protons oscillate in bulk against one another. Notwith-

standing, the Isoscalar Giant Dipole Resonance (ISGDR) does not appear in Fig. 2.1 since it would constitute an oscillation of the centre-of-mass of the nucleus without a restoring force. However, isoscalar 1^- states in the $1\hbar\,\omega$ energy region have been identified using the $(\alpha, \alpha'\gamma)$ reaction [1] and collectively constitute the ISGDR. While the quadrupole mode, where $L = 2\hbar$, can be described as the oscillation of a spherical nucleus to an oblate and then prolate shape [1, 14]. Oscillation modes of $L = 3\hbar$ and $L > 3\hbar$ exist and would be included in a multipole decomposition [14]. The other quantum numbers used to classify the giant-resonance mode are the spin excitation ΔS and the isospin excitation ΔT. The isoscalar giant resonance modes are characterised by $\Delta T = 0$ and are modes in which the neutrons and protons oscillate in phase, thus implying that they are modes without isospin excitation [8, 14]. Conversely, the isovector giant resonance modes are characterised by $\Delta T = 1$ and are associated with the isospin excitation since they involve the out-of-phase oscillation of the neutrons and protons [14].

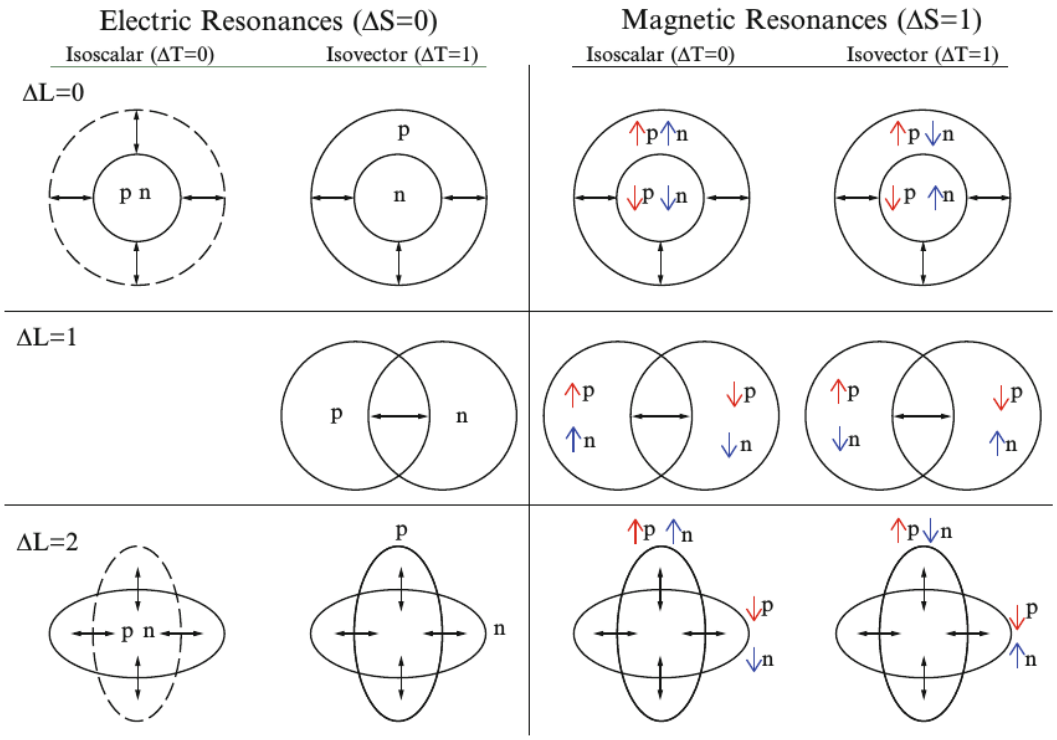

Figure 2.1: A schematic illustration of the different oscillation modes of a nucleus (taken from [7]).

The nucleus also comprises both "spin-up" and "spin-down" components, which implies that for each existing multipolarity, there are four possible combinations of the above-mentioned properties as shown in Fig. 2.1 [7, 14]. The oscillations of the spin-up and spin-down nucleons in phase are classified as $\Delta S = 0$ modes, while the modes referred to as spin-flip modes can be classified as $\Delta S = 1$ modes and are produced when spin-up and spin-down nucleons oscillate out of phase with one another [15]. The $\Delta S = 0$ and $\Delta S = 1$ modes are also referred to as the electric and magnetic giant-resonance modes, respectively [14, 15].

It is possible to infer the collectivity of a specific mode by studying the transition rates for their electromagnetic excitation or de-excitation. The collectivity can also be deduced from measurements of the cross sections of the excitation via direct reactions such as inelastic scattering [1, 14].

The single-particle transition rates provide an estimate for a single nucleon promoted from one level of the shell model to another [1]. Sum rules provide information on the total expected transition strength of a mode with specified L, T, and S values. Both the single-particle transition rate and sum rules are useful criteria to determine whether the transition is collective or not [1, 16]. A transition must satisfy certain criteria in order to be considered collective. These criteria state that the transition rate must be greater than or equal to 10 times the transition rate of the single-particle value, and that an appreciable portion of the sum rule must be exhausted [2, 3]. Giant resonances exhaust approximately 20% - 90% of their respective sum rules [14].

Figure 2.2 provides a schematic representation of the electric multipole transitions that may occur between states of the shell model of a hypothetical nucleus [14]. Collective transitions will only result from the superpositions of single-particle transitions; however, these superpositions must be constructive in order for the collective transitions to occur. In Fig. 2.2, the major shells of the nucleus are denoted N, $N+1$, $N+2$, etc. The major shells are separated

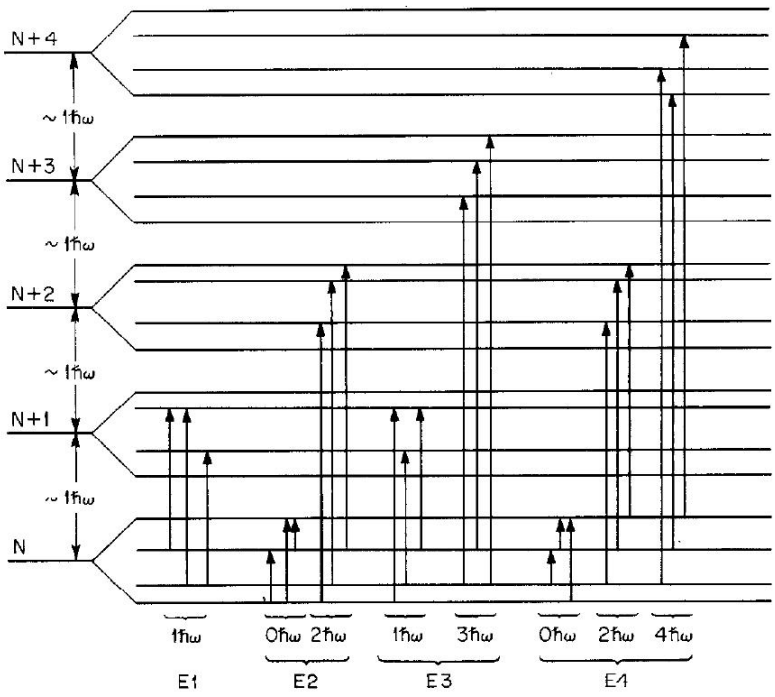

Figure 2.2: A schematic illustration of the electric multipole transitions between states of the shell model of a hypothetical nucleus (taken from [14]).

by approximately $1\hbar\omega$ or by approximately $41A^{-1/3}$ MeV [14].

2.2 Damping of giant resonances

2.2.1 Width Γ of the resonance

There are three parameters, apart from the angular-momentum quantum number, the spin excitation and the isospin excitation, that describe a resonance [1]. These three parameters are the energy E_{C}, the strength S_{R}, and the width Γ, where the width is the most important since a theoretical understanding of the width requires the most complicated description [1]. The width of a giant resonance is described as follows:

$$\Gamma = \Delta\Gamma + \Gamma^{\uparrow} + \Gamma^{\downarrow}, \tag{2.1}$$

where $\Delta\Gamma$ is the inherent width of the giant resonance which arises from a phenomenon in which the excitation energy spreads in the initial 1p-1h strength function [3]. A spreading such as this can and will only occur if there are many non-collective 1p-1h configurations that have the same set of quantum numbers as the collective state and an energy close to that of the collective state [1]. The spin-orbit interaction in nuclei will remove the degeneracy of spin-orbit partners, which will allow for a strong variation in the excitation energy of the 1p-1h configurations that have the same spin and parity [1]. This, in turn, causes the state to become fragmented and is known as Landau damping [3]. Giant resonances are located in a high excitation-energy region where there is a high density of 2p-2h configurations, again with the same spin and parity as the 1p-1h giant-resonance configuration [17].

The escape width, $\Gamma^{\uparrow}$, is an acquired width [1]. In general, the collective 1p-1h state is above the particle-decay threshold. This width is then acquired by the emission of a particle [1]. When the decay is through particle emission, the escape width can be used to express the direct decay of the collective 1p-1h state in a nucleus with mass number A. Experimentally, this process populates the hole states in the nucleus.

The spreading width, denoted by $\Gamma^{\downarrow}$, occurs when the 2p-2h configurations couple. The spreading width causes the 1p-1h states to mix with the 2p-2h states, which then progressively dissolve into the more-complex 3p-3h states [17]. This process continues until the energy has been spread over all degrees of freedom and a compound nucleus is formed. The decay of this nucleus can then be described by means of a statistical model [1].

2.3 Isoscalar Giant Monopole Resonance

The ISGMR is characterised by $L = 0\hbar$, $\Delta S = 0$, and $\Delta T = 0$ (refer to Fig. 2.1), and has long been regarded as the optimal observable from which to determine the compression modulus of the nucleus, i.e. the nuclear compressibility [18]. This mode is also known as the compressional mode or breathing mode (whose identity is firmly established from the angular distribution of α-particle inelastic scattering at extreme forward scattering angles down to 0° [19]) and, macroscopically, can be thought of as a radial oscillation of the nucleus as a whole. The ISGMR is of particular importance because knowledge of its excitation energy relates directly to the nuclear incompressibility K_{A} and then, by extrapolation, the nuclear-matter incompressibility K_{nm} can be deduced [1]. In the description of nuclear matter, a fundamental quantity is the nuclear-matter incompressibility and it is also a fundamental parameter needed to describe neutron stars and supernova explosions [1]. Accurate assessment of the incompressibility coefficient is directly related to the curvature of the Equation Of State (EOS) [20]. The nuclear EOS is needed to describe supernova evolution, cooling of neutron stars, heavy-ion collisions and novel many-body systems [21].

The first direct observation of the ISGMR was made using an inelastic-scattering reaction of 120 MeV alpha particles from a ^{208}Pb target [4]. Figure 2.3 shows the spectra obtained at scattering angles of 12° and 14°. In the 14° spectrum, the presence of what appears to be two wide peaks, indicated by the dashed lines, can be seen. These two broad peaks are in the giant-resonance region of the spectrum. The larger peak is located at approximately 11 MeV [4, 14], which is now synonymous with the giant quadrupole resonance region [14, 18]. The smaller of the two peaks is located at approximately 13.9 MeV (or $80A^{-1/3}$), which is very close to the energy of the giant dipole resonance in ^{208}Pb. The Isovector Giant Dipole Resonance (IVGDR), however, is not excited strongly enough by this particular scattering reaction to account for the presence of

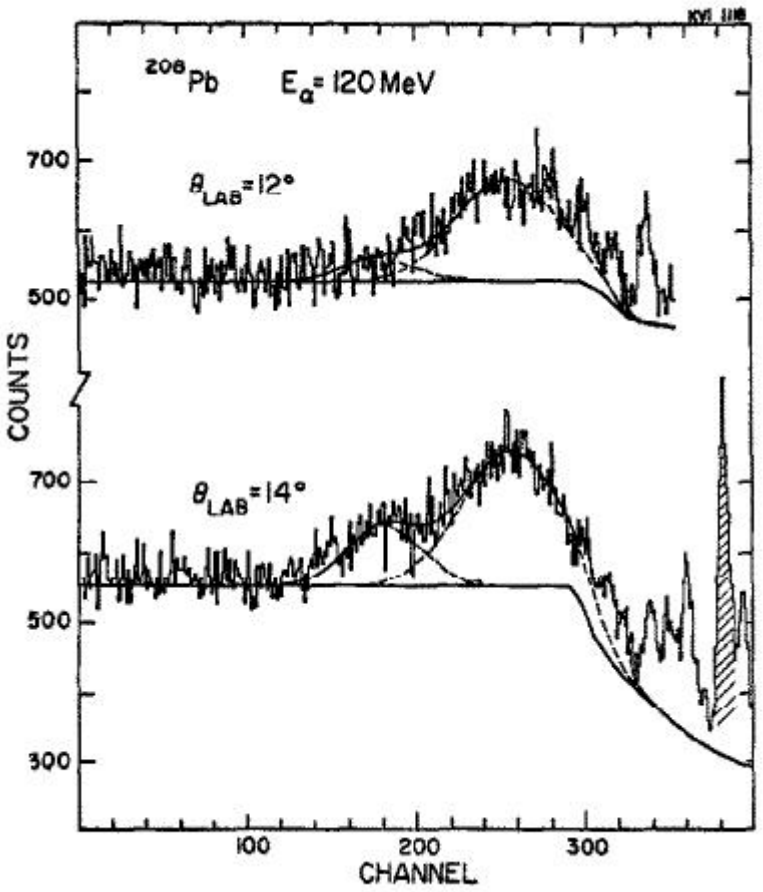

Figure 2.3: Giant-resonance spectra for the inelastic-scattering reaction of 120 MeV α particles at scattering angles of 12° and 14° for ^{208}Pb (taken from [4]).

this peak. A similar peak was also found in ^{197}Au, ^{209}Bi and ^{206}Pb [4, 22]. The peak in the 14° spectrum is a relatively stronger excitation than the one shown in the 12° spectrum of Fig. 2.3, which indicates a multipolarity that is different from $L = 2\hbar$. Two possibilities are then available for consideration, these being a $\Delta L = 0\hbar$ transfer and a $\Delta L = 4\hbar$ transfer. In 1977, Youngblood et al. [6] measured the angular distributions of the inelastically scattered α particles at very small scattering angles, and it was found that a $\Delta L = 0\hbar$ transfer is the definite assignment as it shows a very characteristic pattern.

Thus far, the following properties of the ISGMR have been well established. In nuclei with $A \geq 90$, the ISGMR has a highly concentrated strength distribution, which can be described very well by a Gaussian distribution. The

centroid energy of the Gaussian distribution has been found to be approximately $80A^{-1/3}$ MeV and is important for the calculation of the nuclear incompressibility [23, 24]. In nuclei with $A \geq 90$, 100% of the sum-rule strength has been located. The width of the ISGMR increases from approximately 2.5 MeV in the lead region to 4 MeV in the $A = 90$ region [1]. In a deformed nucleus, the strength distribution of the ISGMR is much broader than it appears in spherical nuclei that have the same A. Giant resonances in spherical nuclei are, however, better described by Lorentzian distributions [25]. Such a distribution is given by:

$$\sigma(E) = \frac{\sigma_{\mathrm{c}}\Gamma^2 E^2}{\left(E^2 - E_{\mathrm{c}}^2\right)^2 + \Gamma^2 E^2}, \tag{2.2}$$

which is dependent on the resonance energy, E_{c}, the width of the resonance, Γ, and the cross section of the peak, σ_{c} [25, 26].

2.3.1 ISGMR in different mass regions

The systematic excitation energy of the ISGMR is well determined at $80/A^{1/3}$ MeV in the heavier-nuclei range. The excitation energy arises from particle-hole excitations into the oscillator shell above [19]. One of the characteristic features of the ISGMR is the apparent disappearance it exhibits in lighter nuclei. This disappearance is not an actual disappearance of the ISGMR but rather a severe spreading and breaking up of the resonance [19]. Further-more, in light nuclei, the ISGMR and ISGQR are strongly entangled with each other [27]. These two resonances widely overlap each other in the experimental region and their respective contributions are, therefore, extremely difficult extract independently [27].

The isoscalar giant monopole and dipole modes are known as the compression-mode giant resonances and are perfect examples of collective nuclear motion [28]. A key parameter of the nuclear EOS is the incompressibility of uniform

nuclear matter. Interest in these giant resonances originates from the hope that the incompressibility of nuclear matter can be extrapolated from their properties [28]. In several medium-heavy nuclei, the ISGMR is a well-defined compression mode; however, it gets fragmented in lighter and/or deformed systems [28]. Equating the ISGMR with a macroscopic compressional "single mode" then becomes highly problematic. Previously, the ISGMR in ^{208}Pb has been used to extract the value of the nuclear incompressibility [29]. This understanding is now being checked against other types of nuclei, which may allow for a broader view or perspective change in terms of understanding and calculating the nuclear incompressibility [28].

2.3.1.1 ISGMR in light nuclei

In this study, the lightest nucleus under consideration is ^{24}Mg. The experimental conditions for the ISGMR in lighter nuclei are very different from those of the heavier nuclei in that identification of the $E0$ (the electric monopole single-particle transition operator) EWSR strength has proven to be extremely difficult and almost impossible in some cases [30]. This happens as a result of fragmentation of the strength distributions of the giant resonances. In some cases, there exists a nearly complete overlap in the excitation energies of the ISGMR and the ISGQR. It is then necessary to use a slicing technique and a Multipole Decomposition Analysis (MDA) procedure to differentiate between these two resonances. This was done for ^{24}Mg in Ref. [30]. The ISGMR for light nuclei is important in order to determine the nuclear incompressibility, which can only be done if the observed ISGMR strength exhausts $\sim$100% of the sum rule.

Figure 2.4 shows spectra taken at different extreme forward scattering angles using 120 MeV α-particles intended to excite the ISGMR in ^{24}Mg [30]. This figure shows that the multipole strength is highly fragmented in this particular nucleus, and that if the underlying continuum is present at all, it is very small.

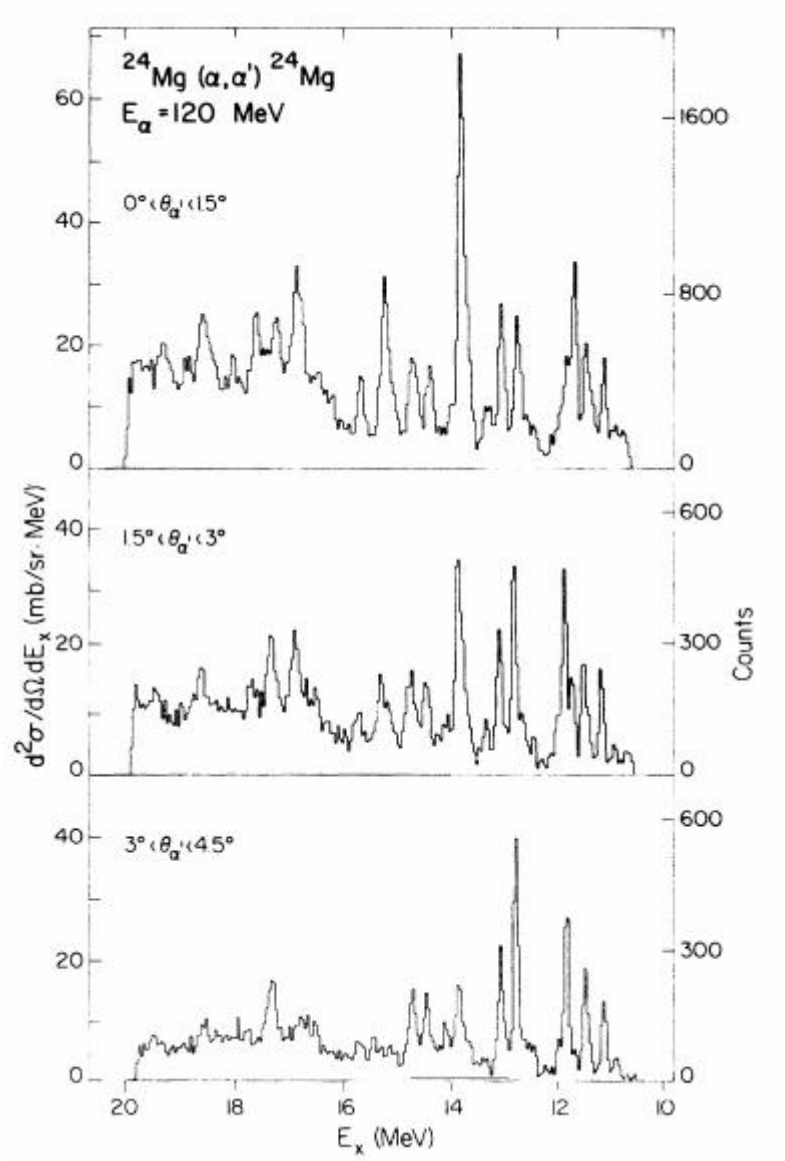

Figure 2.4: Alpha inelastic-scattering spectra for ^{24}Mg with $E_\alpha = 120$ MeV at small scattering angles (taken from [30]).

It can be seen in Fig. 2.4 that several peaks display a typical $\Delta L = 0\hbar$ pattern, a great example of which is the peak near 13.9 MeV [30].

2.3.1.2 ISGMR in medium mass nuclei

The main problem for nuclei with $A \leq 90$ is that there exists an intermingling of the various multipolarities. Experimentally, this is problematic since their various strengths must be disentangled. As was discussed previously,

this intermingling of multipolarities is illustrated in the ^{24}Mg nucleus. The fragmentation of the strengths is such that for multiple peaks that exist in the giant-resonance energy region, the multipolarity can be separately determined and the strength distributions broken down by taking the energy spectrum and dividing it into small energy bins. Each bin will then need the angular distributions as a sum of several multipolarities to be analysed [1]. In the case where the strength distribution is more continuous, a problem will occur when $E0$ intermingles with a significant part of $E1$ (the electric dipole transition operator). The isoscalar $E1$ strength has an angular distribution with a relative minimum at 0° and a relative maximum at approximately the first minimum of the $E0$ angular distribution. The net effect will, therefore, most likely resemble an approximately flat angular distribution, which will cause the $E0$ strength to be completely missed [1].

In nuclei where the mass number is between 40 and 90, 30% of the $E0$ EWSR has been found to be exhausted by the α-particle inelastic-scattering reaction with $E_\alpha = 130$ MeV. This is indicative of the presence of a monopole resonance [31]. Youngblood et al. [31], reported that the Giant Dipole Resonance (GDR) and Giant Monopole Resonance (GMR) could not be separated in that work; however, it was also not possible to definitely identify the GMR from its angular distribution.

2.4 Choice of projectile

2.4.1 General α-particle considerations

It is generally known that there is no well-defined/well-documented boundary that distinguishes between the light and heavy ions [32]. The use of α particles as projectiles has shown that they exhibit certain features that are not only characteristic of heavier projectiles but are more complex than the features of

lighter projectiles. The α particle is, therefore, sometimes referred to as the "lightest-heavy ion" [32]. High-quality, high-intensity α-particle beams have become widely available and are now a conventional tool in nuclear-physics experiments [30, 31, 32, 33].

2.4.2 Alpha-particle scattering

Elastic and inelastic scattering reactions using intermediate-energy α-particles results in differential cross sections exhibiting strong diffraction patterns. However, these scattering reactions must occur at energies above the Coulomb barrier (see Section 2.5) [34]. The method of α-particle inelastic scattering at intermediate energies is one of the most-functional probes used to measure the ISGMR strengths, provided that the measurements are performed at extreme forward scattering angles [35]. These types of reactions have an immediate selectivity for those transitions that have a natural parity. As a result, there exists a good linear relationship between the (reaction-specific) cross sections and the relevant nuclear transition matrix elements [35].

The choice of α-particles as a scattering probe is important because they select natural-parity transitions (such as the 0° strength of the ISGMR) and because isoscalar transitions are strongly favoured.

2.5 Rutherford approach

The semi-classical approach to the Coloumb-excitation process considers the projectile as a point-like charged particle. The point-like charged particle moves along a hyperbolic trajectory within the repulsive Coloumb field of the target nucleus (see Fig. 2.5) [26]. A Rutherford path is assumed to be taken by the projectile at low incident energies; conversely, at high incident energies, it is assumed that the particle follows a straight-line path [26]. The Coulomb

barrier is the barrier of energy that exists owing to the electrostatic interaction that two nuclei must overcome so that they can get close enough to undergo a reaction. In a typical scattering experiment, the projectile will approach the target nucleus along a straight line. If a repulsive force is not present, the projectile will pass a distance b from the nucleus. This distance b is known as the impact parameter. In Rutherford scattering, the impact parameter is given by:

$$b = \frac{Z_{\mathrm{P}} Z_{\mathrm{T}} e^2}{4\pi\epsilon_0} \frac{1}{p v_0} \frac{1}{\tan(\theta/2)}, \tag{2.3}$$

where

$$K = p v_0, \tag{2.4}$$

and is the initial kinetic energy of the projectile. The relationship between the impact parameter, b, and the scattering angle, θ, can be seen in Eq. (2.3), where Z_{P} and Z_{T} are the atomic numbers of the projectile and target, respectively. If an assumed head-on collision takes place, with the use of the conservation of energy, it is possible to calculate the distance of closest approach, d_0 [26]:

$$K = \frac{Z_{\mathrm{P}} Z_{\mathrm{T}} e^2}{4\pi\epsilon_0} \frac{1}{d_0}, \tag{2.5}$$

$$d_0 = \frac{Z_{\mathrm{P}} Z_{\mathrm{T}} e^2}{4\pi\epsilon_0} \frac{1}{K}, \tag{2.6}$$

leading to a simplification of the relationship between the impact parameter and the scattering angle [26]:

$$b = \frac{d_0}{2} \frac{1}{\tan(\theta/2)}. \tag{2.7}$$

By combining the previous equations, it is possible to obtain the Rutherford differential cross section using assumptions: the projectile follows a hyperbolic trajectory in the Coulomb field of the target, and the scattering angle must be calculated. The Rutherford differential cross section is, therefore, given by:

$$\frac{d\sigma}{d\Omega} = \left(\frac{d_0}{4}\right)^2 \frac{1}{\sin^4(\theta/2)}, \tag{2.8}$$

and when simplified:

$$\frac{d\sigma}{d\Omega} = \left(\frac{Z_{\mathrm{P}} Z_{\mathrm{T}} e^2}{4\pi\epsilon_0}\frac{1}{4K}\right)^2 \frac{1}{\sin^4(\theta/2)}. \tag{2.9}$$

The relative motion of the interaction is considered to be approximated to a good degree by the Rutherford trajectory.

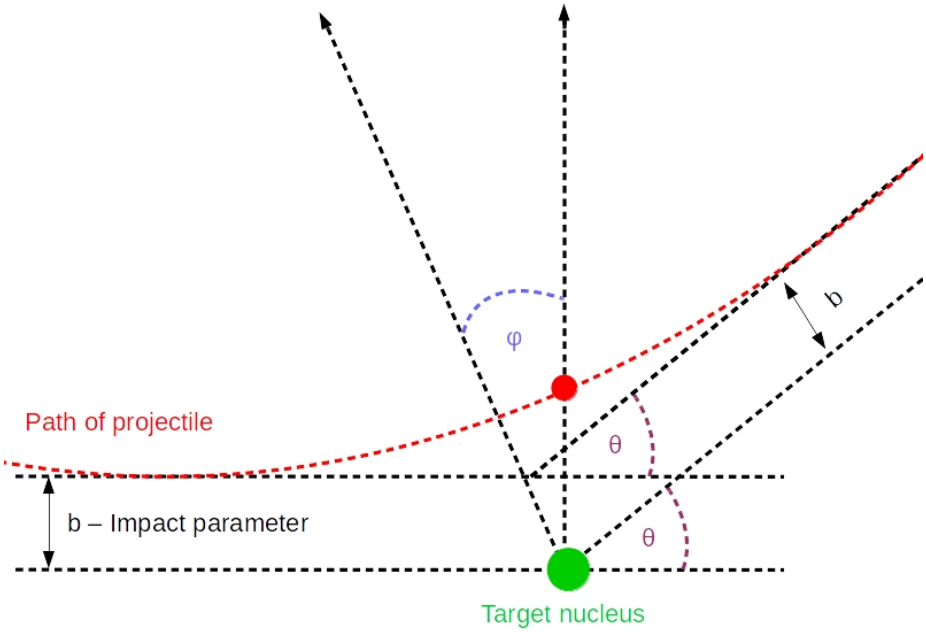

Figure 2.5: A schematic representation of the Coulomb-excitation process.

2.6 Theoretical model predictions

As mentioned in Chapter 1, a well-documented and established property of giant resonances is the exhaustion of a rather large fraction of the EWSR. Sum rules allow for a relation between the experimentally observed ground-state properties and the strength distribution of the excited states integrated over all of the energies.

2.6.1 Random Phase Approximation (RPA)

The Random Phase Approximation (RPA), a simple many-body theory, provides a theoretical description wherein the sum rules are satisfied by the model states in the same way as the exact states. RPA is, therefore, the basic microscopic theory for describing of giant resonances. The RPA framework describes giant resonances as a coherent superposition of 1p-1h excitations that are built on a corresponding ground state. A great difficulty exists within this model. The complexity of giant-resonance calculations (which span beyond the standard RPA) increases exponentially with the size of the configuration space, while the space in which it must work is quite limited [36]. This complexity was overcome by appropriate introduction of Quasiparticle-RPA based on effective nucleon-nucleon interaction, which accommodates large space configurations. Damping mechanisms are one such case where the complexity of the calculations span beyond the standard RPA, and so, an extension is needed. An appropriate extension to the RPA is the Quasiparticle Random Phase Approximation.

2.6.2 Quasiparticle Random Phase Approximation (QRPA)

QRPA calculations make it possible to relate the ground-state properties to the excited states by the same energy-density functional [37]. This type of approach describes the properties of the low-lying states less accurately than the phenomenological approaches do, but the results are in reasonable agreement with experimental data [37, 38, 39]. A detailed explanation is presented in [39] and so, only a brief explanation is presented here.

The starting point of this method is the Hartree-Fock plus Bardeen-Cooper-Schrieffer, (HF)-BCS, calculation [40] of the ground state. This is when the

quasiparticle wave functions have spherical symmetry imposed on them. The continuous part of the single-particle spectrum is discretised. This is achieved by diagonalising the Skyrme HF Hamiltonian on a harmonic-oscillator basis [37]. Skyrme interactions are used as the effective interactions in the particle-hole channel. The pairing correlations are then generated by a zero-range density-dependent force [37]:

$$V_{\text{pair}}(\vec{r_1}, \vec{r_2}) = V_0 \left[1 - \eta \left(\frac{\rho(\vec{r_1})}{\rho_0} \right)^{\alpha} \right] \delta(\vec{r_1} - \vec{r_2}), \tag{2.10}$$

where $\rho(\vec{r_1})$ is the particle density in coordinate space, ρ is the nuclear-saturation density and V_0 is a parameter that remains fixed in order to reproduce the odd-even mass difference of nuclei in the region of interest [39].

The residual interaction $V_{\text{res}}^{\text{ph}}$ in the p-h channel is obtained by taking the second derivatives of the energy-density functional with respect to the particle density ρ and the pair density $\tilde{\rho}$. The residual interaction is then simplified by approximating it by the corresponding Landau-Migdal form [39]. The Landau parameters for Skyrme interactions are functions of the coordinate $\vec{r}$. A full explanation of the Skyrme force parameters is given in Ref. [41]. The residual interaction is given by:

$$V_{\text{res}}^{a}(\vec{r_1}, \vec{r_2}) = N_0^{-1} [F_0^a(\vec{r_1}) + F_0' a(\vec{r_1}) \tau_1 \cdot \tau_2] \delta(\vec{r_1} - \vec{r_2}), \tag{2.11}$$

where a is the channel index and τ_i is the isospin operator.

$$N_0 = \frac{2 k_{\text{F}} m^*}{\pi^2 \hbar^2}, \tag{2.12}$$

where k_{F} is the Fermi momentum and m^* is the nucleon effective mass.

2.6.3 Phonon-phonon coupling

In the Quasiparticle Phonon Model (QPM) approach, 1p-1h excitations are projected onto a space of one-phonon states. The properties of these excitations, the excitation energy and the internal fermionic structure, are obtained by solving the QRPA equations [42]. After construction of the phonon basis, the wave function of the excited states is written as a combination of the interaction between one- and multi-phonon configurations [26].

Phonon-phonon coupling takes the basic concepts of the QPM model into account [42]. The Hamiltonian is diagonalised in a space that is spanned by states composed of one- and two-QRPA phonons:

$$\Psi_\nu(\lambda\mu) = \left(\sum_i R_i(\lambda\nu) Q^+_{\lambda\mu i} + \sum_{\lambda_1 i_1 \lambda_2 i_2} P^{\lambda_1 i_1}_{\lambda_2 i_2}(\lambda\nu) \left[Q^+_{\lambda_1\mu_1 i_1} Q^+_{\lambda_2\mu_2 i_2} \right]_{|\lambda\mu} \right) |0\rangle, \tag{2.13}$$

with the normalisation condition represented as:

$$\sum_i R_i^2(\lambda\nu) + 2 \sum_{\lambda_1 i_1 \lambda_2 i_2} \left[P^{\lambda_1 i_1}_{\lambda_2 i_2}(\lambda\nu) \right]^2 = 1. \tag{2.14}$$

The Hamiltonian can be rewritten in terms of the quasiparticle and phonon operators [37, 42, 43]. If the two-phonon components of the wave functions are to obey the Pauli principle, the exact commutation relations between the phonon operators must be taken into consideration [42]. The variational principle determines the amplitudes of $R_i(\lambda\nu)$ and $P^{\lambda_1 i_1}_{\lambda_2 i_2}(\lambda\nu)$:

$$\delta \left(\langle \Psi_\nu(\lambda\mu) | H | \Psi_\nu(\lambda\mu) \rangle - E_\nu \left(\langle \Psi_\nu(\lambda\mu) | \Psi_\nu(\lambda\mu) \rangle - 1 \right) \right) = 0, \tag{2.15}$$

leading to a set of linear equations [37, 43]:

$$\left(\omega_{\lambda i} - E_\nu \right) R_i(\lambda\nu) + \sum_{\lambda_1 i_1 \lambda_2 i_2} U^{\lambda_1 i_1}_{\lambda_2 i_2}(\lambda i) P^{\lambda_1 i_1}_{\lambda_2 i_2}(\lambda\nu) = 0, \tag{2.16}$$

and

$$2\left(\omega_{\lambda_1 i_1}+\omega_{\lambda_2 i_2}-E_\nu\right)P^{\lambda_1 i_1}_{\lambda_2 i_2}(\lambda\nu)+\sum_i U^{\lambda_1 i_1}_{\lambda_2 i_2}(\lambda i)R_i(\lambda\nu)=0. \tag{2.17}$$

The set of linear equations is representative of one- and two-phonon configurations included in the wave function (i.e. Eq. (2.13)), respectively. Equations (2.16) and (2.17) have the same form as QPM equations; however, the single-particle spectrum (and parameters of the residual interaction) is (are) calculated with the chosen Skyrme forces [42].

2.7 Distorted Wave Born Approximation (DWBA) and nuclear potentials

Distorted Wave Born Approximation calculations are needed to determine the angular distribution of various multipoles for the (α,α') reaction. The angular distributions allow for the selection of the most appropriate scattering angle which determines the multipole (which in this study is the ISGMR). The DWUCK4 computer code [44] is used to calculate the scattering and reaction observables for binary nuclear reactions with the use of the Distorted Wave Born Approximation (DWBA). A full description of the code is presented in [44] and [45] and, as such, only a brief description is provided below.

The transition amplitude of the reaction is given by [44]

$$T=J\int d^3\vec{r_b}\int d^3\vec{r_a}\chi^{*(-)}(\vec{k_f},\vec{r_b})^*\langle bB|V|aA\rangle\chi^{(+)}(\vec{k_i},\vec{r_a}), \tag{2.18}$$

where $\chi^{(-)}$ and $\chi^{(+)}$ are the distorted waves that describe the relative motion before and after a collision, respectively [44]. Here, J is representative of the Jacobian for the transformation to the co-ordinates of the systems, which is $\vec{r_a}$ for (a,A) and $\vec{r_b}$ for (b,B), and $\langle bB|V|aA\rangle$ is a matrix element which defines

the form factor for the reaction. The requirement is that a delta function must be contained between the $\vec{r_a}$ and $\vec{r_b}$ co-ordinates.

The interaction potential, V, is dependent on the internal co-ordinates and can be separated into Coulomb and nuclear potentials. Distorted waves are used to asymptotically describe plane waves (momentum $\vec{k}$) and incoming (or outgoing) spherical scattered waves. Where no Coulomb potential is present, the case is described as:

$$\chi^{(\pm)}(\vec{k},\vec{r}) \rightarrow e^{i\vec{k}\cdot\vec{r}} + f(\theta)\frac{e^{\pm ikr}}{r}. \tag{2.19}$$

The relationship between the final distorted wave and the solution of the outgoing waves is given by:

$$\chi^{(-)*}(\vec{k},\vec{r}) = \chi^{(+)}(-\vec{k},\vec{r}). \tag{2.20}$$

Calculation of the cross section depends on whether the reaction is particle transfer or inelastic scattering. For the inelastic-scattering reaction, $b = a'$ (the inelastically scattered projectile) and $B = A^*$ (the excited target nucleus). The complex nuclear potential is given by:

$$U(r) = V(r) + iW(r), \tag{2.21}$$

where $V(r)$ represents the real part of the potential that describes the elastic scattering, while $W(r)$ is representative of the imaginary part of the potential that is responsible for the absorption of flux into the non-elastic channels. The nuclear potential is an attractive short-range potential that is representative of the many-body interaction between colliding nuclei and is, therefore, a complex potential. The Woods-Saxon potential is commonly used as it is a physically realistic phenomenological potential [44, 45]. The Woods-Saxon potential suitably describes the real and imaginary potentials of Eq. (2.21)

leading to:

$$U(r) = -\left[V f_{\mathrm{R}}(r) + iW f_{\mathrm{I}}(r)\right], \tag{2.22}$$

where $f_{\mathrm{R,I}}(r)$ represents the volume Woods-Saxon potential:

$$f_{\mathrm{R,I}}(r) = \left[1 + \exp\left(\frac{r - R_{\mathrm{R,I}}}{a_{\mathrm{R,I}}}\right)\right]^{-1} \tag{2.23}$$

and

$$R_{\mathrm{R,I}} = r_{0\mathrm{R,I}}(A_1^{1/3} + A_2^{1/3}), \tag{2.24}$$

in the heavy-ion convention and

$$R_{\mathrm{R,I}} = r_{0\mathrm{R,I}}(A_2^{1/3}), \tag{2.25}$$

in the light-ion convention. Surface-diffuseness parameters are represented by $a_{\mathrm{R,I}}$ for both the real and imaginary parts, respectively. The mass of the projectile and target is represented by A_1 and A_2, respectively. If adequate agreement to elastic-scattering data must be obtained, the nuclear potential must include the nuclear surface diffuseness. Varying one (or more) of the parameters (V_{R}, R_{R}, a_{R}, V_{I}, R_{I}, a_{I}) can assist in obtaining a fit to elastic-scattering data.

DWBA inelastic scattering, in first order, is treated as a one-step transition process and is inclusive of a collective form-factor [45]. In the collective model, however, it is rational to expect that the nuclear interaction follows the nuclear surface shape. The collective form-factor can be described as the derivative of the interaction potential. This results from either the vibrations about a spherical mean radius (R_0), which deform the spherically symmetric optical potential, or by the rotations of a permanently deformed sphere. The collective form factor is given by [45]:

$$U(r) = U(r - R_0) - \delta R \frac{d}{dr} U(r - R_0), \tag{2.26}$$

where δ is the deformation length. The deformation length for a rotational nucleus is given by:

$$\delta_L = R_{\mathrm{R}}\beta_L^{\mathrm{R}} = R_{\mathrm{W}}\beta_L^{\mathrm{I}}, \tag{2.27}$$

where R_{R} and R_{W} are representative of the real and imaginary nuclear radii. β_L^{R} and β_L^{I} are the respective real and imaginary deformation parameters and are dependent on the multipolarity (L) of the excited state [45].

2.8 Fine structure

The decay of giant resonances in nuclei provides important information on how a well-ordered collective excitation dissolves into a disordered motion of internal degrees of freedom in fermionic quantum many-body systems [46]. This is understood to result from the decay of the collective modes towards compound nuclear states leading to internal mixing [47]. Apart from this internal mixing, the nuclear states may also decay into a continuum of escaping states that give rise to the de-excitation of the system through particle emission [47].

High energy-resolution experiments conducted on nuclei in the region of giant resonances provide a unique method of extracting information about the dominant processes of decay [48]. This information is imprinted into the fragmentation of giant resonances that is visible as fine structure in the excitation-energy spectra [48].

In recent years, fine structure has been established as a global phenomenon in medium- to heavy-mass nuclei for the case of the ISGQR [49]. Fine structure has also been demonstrated for a variety of other modes such as the spin-isospin-flip Gamow-Teller mode [50], the IVGDR [3, 26, 51] and the magnetic quadrupole resonance [52]. Systematic studies of the ISGQR and the IVGDR at the iThemba Laboratory for Accelerator Based Sciences (iThemba

LABS) and the Research Center for Nuclear Physics (RCNP), Japan, have shown a difference in the main mechanism responsible for the fine-structure phenomenon in these resonances, with coupling to low-lying surface vibrations being responsible in the former [49, 53] and Landau damping being responsible in the latter [54]. It is, therefore, of obvious interest to investigate the cause of the fine structure in the case of the ISGMR.

2.9 Extraction of characteristic energy scales

Wavelet analyses were developed independently by physicists, engineers and mathematicians. Owing to collaborations in these fields, the development of new and varied applications has seen vast growth in the last decade [55]. Wavelets are used in data analyses and the interpretations thereof. The fundamental concept behind this dictates that the analysis is performed according to scale. Wavelets are a set of functions, which are known to satisfy a set of mathematical requirements, that are predetermined and used to represent the data or other functions. Fourier analysis uses the same concept [55]. The scales that are used to process data within the wavelet analysis are the distinguishing factor. These scales then go on to play an important role in the interpretation of the analysed data. The window through which a signal is observed dictates the scale of the features observed. If observed through a large window, the gross/macroscopic features will be noticed. If observed through a small window, the microscopic features will be observed. Wavelet analysis allows for both types of features to be seen [55].

Why is wavelet analysis used in the fine-structure analysis of giant resonances and is it well suited? The sine and cosine functions that are used to represent data in the Fourier-analysis case are not only global functions but they also expand infinitely. There is a disadvantage to this approach as it adversely approximates any sharp spikes that may occur in the data. Approximating

functions that are contained in finite domains are the functions that form the basis of wavelet analysis. The fine-structure data of giant resonances are filled with sharp discontinuities and, therefore, wavelet analysis is ideal for the analysis. Applications of wavelet analysis in the study of nuclear giant resonances can be seen in Refs. [3, 48, 49].

The wavelet-analysis procedure is dependent on the selection of a preliminary wavelet, also known as a Mother wavelet [55]. A time-based analysis is then conducted using a high-frequency version of the Mother wavelet that is also contracted. Contrastingly, a frequency analysis is performed using a low-frequency, dilated version of the Mother wavelet. Wavelet transforms offer a main advantage over Fourier transforms owing to their ability to represent functions that have sharp peaks and discontinuities. Wavelet transforms can be classified into two major categories: Continuous Wavelet Transforms (CWTs) and Discrete Wavelet Transforms (DWTs).

The principle of "small waves" localised in both the frequency and time domains is employed by wavelet transforms. These small waves are referred to as wavelets [56]. Predefined mathematical criteria determine the selection of a particular Mother wavelet [57].

A function (either real or complex) represented by $\Psi(x)$ may be used as a Mother wavelet if the following criteria are met:

$$\int_{-\infty}^{\infty} \Psi^*(x)dx = 0 \tag{2.28}$$

and

$$K_\Psi = \int_{-\infty}^{\infty} |\Psi^2(x)|dx < \infty, \tag{2.29}$$

where $\Psi^*(x)$ is the complex conjugate of $\Psi(x)$ and K_Ψ denotes the wavelet norm.

The Mother wavelets that were used in this study are the complex-Morlet

Mother wavelet (where the wavelets are a product of cosine and Gaussian functions) in the CWT and the Biorthogonal (Bior6.8) Mother wavelet used in DWT. Figure 2.6 illustrates these wavelets [45]. The intrinsic scale of a particular wavelet has a certain arbitrary character; therefore, the choice of wavelet is motivated for based on functional simplicity rather than its mathematical or physical characteristics.

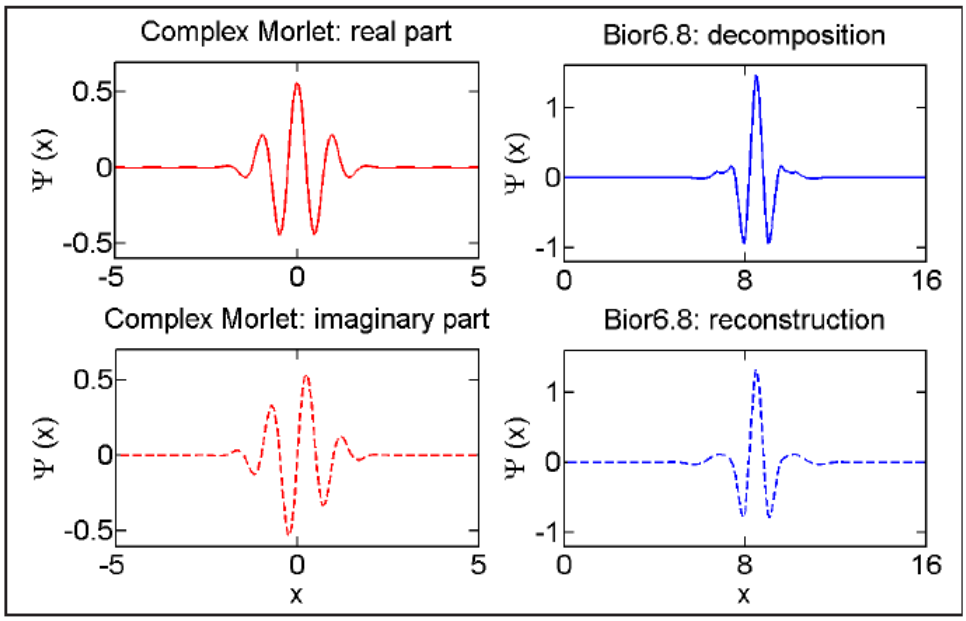

Figure 2.6: Wavelet functions used in this study. *Left*: Complex-Morlet Mother wavelet used for CWT. Both real (*upper*) and imaginary (*lower*) parts are shown. *Right*: Biorthogonal level 6.8 Mother wavelet used for DWT. Both the decomposition (*upper*) and reconstruction (*lower*) functions are shown (taken from [45]).

2.9.1 Continuous Wavelet Transform (CWT)

The Continuous Wavelet Transform of a specific measured spectrum $\sigma(E)$, is defined as its folding with the wavelet function Ψ^*, which is generally a complex-conjugated function, and represented as:

$$C(\delta E, E_x) = \frac{1}{\sqrt{\delta E}} \int \sigma(E) \Psi^* \left(\frac{E_x - E}{\delta E} \right) dE, \tag{2.30}$$

where $C(\delta E, E_x)$ are the wavelet coefficients that scale the function and δE is the bin size, which shifts the wavelet position along the excitation-energy axis. This makes the information on scale localisation accessible. E_{x} denotes the excitation energy [45]. The aforementioned parameters are continuously varied in CWT, which results in a fast and model-independent transform. As a result of such a transform, the wavelet coefficients are obtained as two-dimensional distributions. For positions and scales where the form of the original data spectrum and the scaled and shifted wavelet are very similar, large coefficients are obtained. The converse is also true. The positions and values of the characteristic scales can be extracted from the two-dimensional distributions of the wavelet coefficients [45].

2.9.2 Power spectrum

The Fourier power spectrum (related to a Fourier transform of the form $\hat{f}(k)$ on a function $f(x)$) is given by:

$$P_f(k) = |\hat{f}(k)\hat{f}^*(k)|, \tag{2.31}$$

which is a normalisation of the spectrum [3]. The power, P, can be determined by the absolute value of the complex vector. The power spectrum for a CWT analysis is, therefore, given by the sum of the squares of the complex coefficients. The complex coefficients are determined using the complex-Morlet Mother wavelet. This also results in an equivalent Fourier scale [3].

2.9.3 Discrete Wavelet Transform (DWT)

The Discrete Wavelet Transform adheres to the same principles as the CWT. The difference is that the CWT operates over every possible scale and translation, while the DWT utilises a specific subset of scale and translation values

[45]. DWTs are characterised by their configuration in powers of two, given by:

$$\delta E = 2^k \Delta \tag{2.32}$$

and

$$E_{xk} = k \cdot \delta E_k, k = 1, 2, ..., \tag{2.33}$$

where Δ is the bin size of the data and k is the specification of the number of the significant sinusoidal oscillations within a Gaussian window.

DWTs are used in filtering and compression owing to their ability to represent data more efficiently in comparison to CWTs [58]. The inverse DWT is used to analyse or decompose a signal. The components of the decomposition can be reconstructed into the original signal where there is no loss of information. Some drawbacks of the DWT are that it is not shift invariant and that it gives limited scale resolution [59]. The limited scale resolution is because the bandwidth of the filter can only be increased by a factor of two at each new scale. CWT, in comparison, provides clear results in terms of resolution and/or phase.

DWTs are only possible with specific Mother wavelets where an orthogonal basis of functions can be constructed [59].

2.9.4 DWT background determination

The contribution of the background, $\sigma_{\text{bkg}}(E)$, in the DWT background determination is approximated either by a constant or a polynomial function by the selection of an appropriate level from the decomposition of the signal [45]. This process requires a wavelet function that has a sufficient number of vanishing moments.

The present study made use of the Bior6.8 Mother wavelet owing to the ad-

vantage of providing a good resolution. This Mother wavelet is composed of three vanishing moments. These moments yield results that are insensitive to the background contributions of polynomials up to third order. It is possible to use the Bior6.8 wavelet coefficients to reconstruct the original signal [45]. The application of low-pass and high-pass filters on an original spectrum is illustrated in Fig. 2.7. Low-pass filters are characterised by large scales (δE), while high-pass filters are characterised by small scales. Owing to the spectrum being separated into approximations (A_i) and details (D_i), the original spectrum can be exactly reconstructed at each step of the decomposition [60]. The exact reconstruction is given by:

$$\sigma(E) = A + \sum D_i. \tag{2.34}$$

A detailed explanation of the use of the Bior6.8 wavelet can be found in [48].

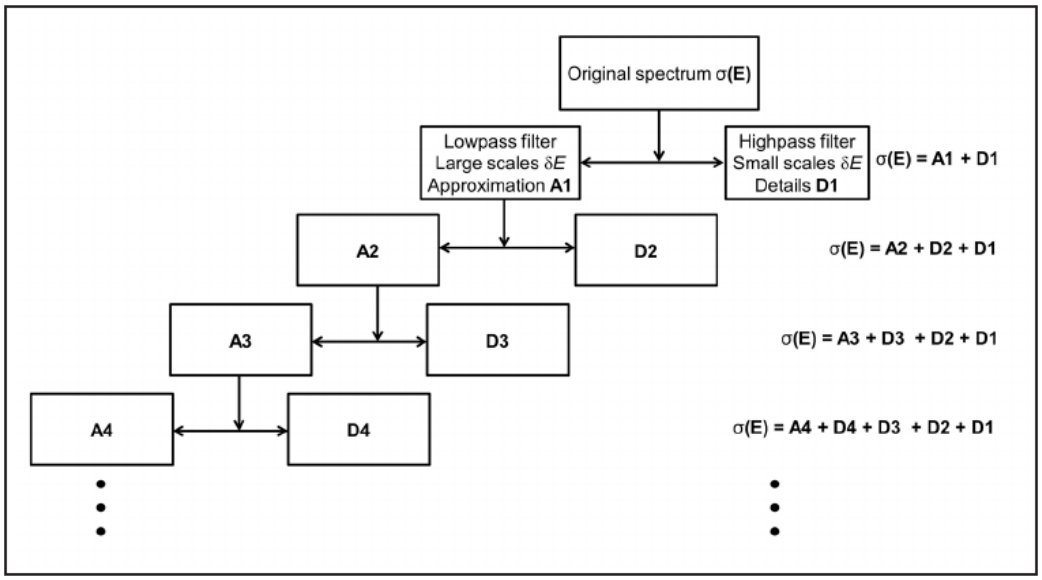

Figure 2.7: A schematic representation of the DWT. Band-pass filters are applied so that the signal is decomposed into components of various frequencies (taken from [45]).

Chapter 3

Experimental details, data extraction and optimisation

This chapter details the experimental techniques, equipment and data-extraction methods used during this experiment. The experimental methods and techniques provides an overview of the necessary equipment, systems and corrections needed while the data extraction and optimisation sections are specific to this experiment.

The experiments for the investigation into the presence of fine structure of the Isoscalar Giant Monopole Resonance in ^{58}Ni and ^{90}Zr were performed at iThemba LABS [61]. The K600 magnetic spectrometer (in zero-degree mode) was used along with a dispersion-matched 200 MeV α-particle beam. The α-particle beam was delivered from the Separated Sector Cyclotron (SSC) of iThemba LABS.

3.1 Accelerator facility

A schematic diagram of iThemba LABS is shown in Fig. 3.1. This figure shows the SSC, which delivers particle beams to the various divisions within iThemba LABS and is, therefore, fundamental in ensuring that iThemba LABS stays up and running.

The beams delivered by the SSC range from proton and neutron beams to beams that are required for light- and heavy-ion production for use in radioisotope production and nuclear-physics research [3]. The existing experimental nuclear-physics facilities at iThemba LABS include the K600 magnetic spectrometer, the A-line nuclear-reaction scattering chamber and the gamma-ray detector array, AFRODITE [3].

Figure 3.1 shows the two injector cyclotrons, which have a K-value of 8 each. Solid Pole injector Cyclotron 1 (SPC1) has an internal ion source called the Penning Ionisation Gauge (PIG) [3]. Solid Pole injector Cyclotron 2 (SPC2) can be used in conjunction with two external ion sources: the polarised-proton ion source and the Electron Cyclotron Resonance (ECR) ion source [3]. In this experiment, SPC2 and the ECR ion source were used.

The process starts at the ECR ion source where the production of the α-particle beams takes place. The beam is injected into SPC2 from the ECR ion source and moves through to the $K = 200$ SSC via the K and J beamlines (seen in Fig. 3.1). At this point, it is accelerated to the required energy of 200 MeV. The accelerated α particles are transferred to the $K = 600$ magnetic spectrometer via a high-resolution double monochromator system, which consists of the X, P1, P2, and S beamlines. In order to optimise the path as well as the delivery of the beam, quadrupole magnets, dipole magnets, and slits are employed [3].

Dispersion matching (detailed in Section 3.5.2) at 0° is achieved via the implementation of the faint-beam technique. Three beam meshes are placed between

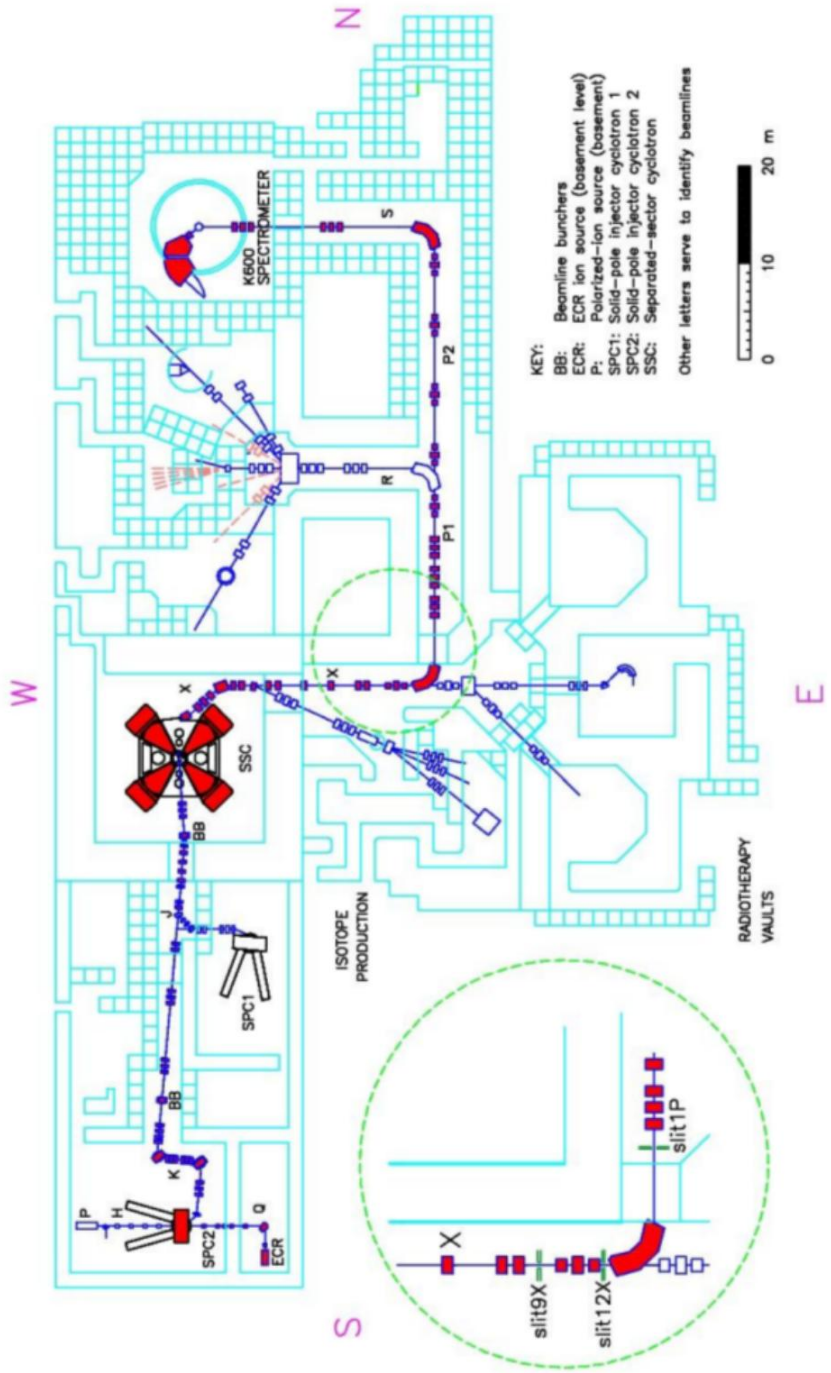

Figure 3.1: Schematic diagram of the layout of iThemba LABS showing the ECR, SPC1, SPC2, the SSC, and the K600 magnetic spectrometer as well as the isotope production and radiotherapy vaults. The enlarged section illustrates the position of the object slit 9X, the emittance slit 12X and the energy-definition slit 1P.

the ECR ion source and SPC2, which results in a significant reduction of the number of alpha particles in the beam. The ion-optical characteristics of the

beam and the beam profile itself, however, remain unchanged [3].

3.2 K600 magnetic spectrometer

The K600 magnetic spectrometer consists of five active elements that can be seen in the schematic diagram presented in Fig. 3.2. The two dipole magnets, referred to as D1 and D2, function mainly to disperse ejectile particles according to their momentum. Furthermore, the momentum dispersion can be varied by varying the ratio of the strengths of the two dipoles. The quadrupole magnet is used to achieve vertical focussing at the focal plane and, finally, the two trim coils, which are located inside the dipoles, are used to achieve final horizontal focussing at the focal plane. These two trim coils are referred to as the K-coil and the H-coil. The K-coil is a pole-face current winding with both a dipole and a quadrupole component that is used to correct for the first-order kinematic variations of momentum with the horizontal scattering angle, i.e. $(x|\theta)$ aberrations [62]. The H-coil is also a pole-face current winding but has a dipole and hexapole component and is used to correct for $(x|\theta^2)$ aberrations [62].

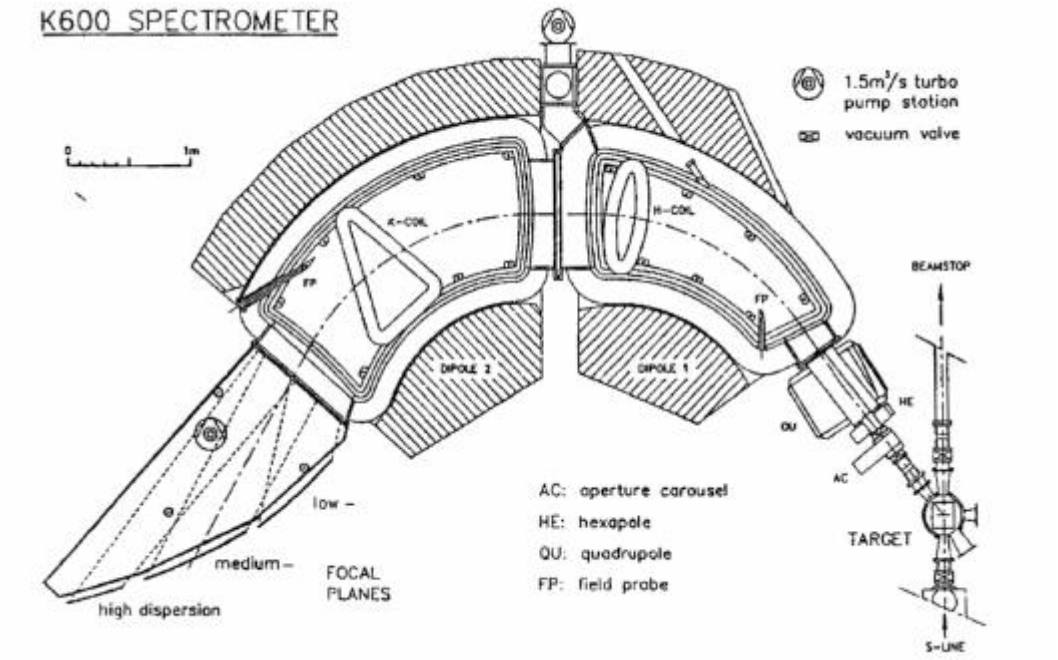

Figure 3.2: Schematic diagram of the K600 magnetic spectrometer at iThemba LABS [62].

A carousel, which houses six collimators, is situated in front of the quadrupole magnet. A scattering chamber with a diameter of 524 mm is situated at the turning axis of the spectrometer. Within the scattering chamber is a target ladder with six target positions as well as a turntable where either an internal beamstop or detectors can be mounted [62].

3.2.1 Zero-degree mode of the K600 magnetic spectrometer

Nuclear reactions are quite complex and often result in experimental spectra that are composed of many different contributions. In order to filter out the unwanted contributions to the experimental spectra, reactions at zero degrees are employed. This is because medium-energy hadronic scattering and reactions at zero degrees are very selective to excitations with low angular-momentum

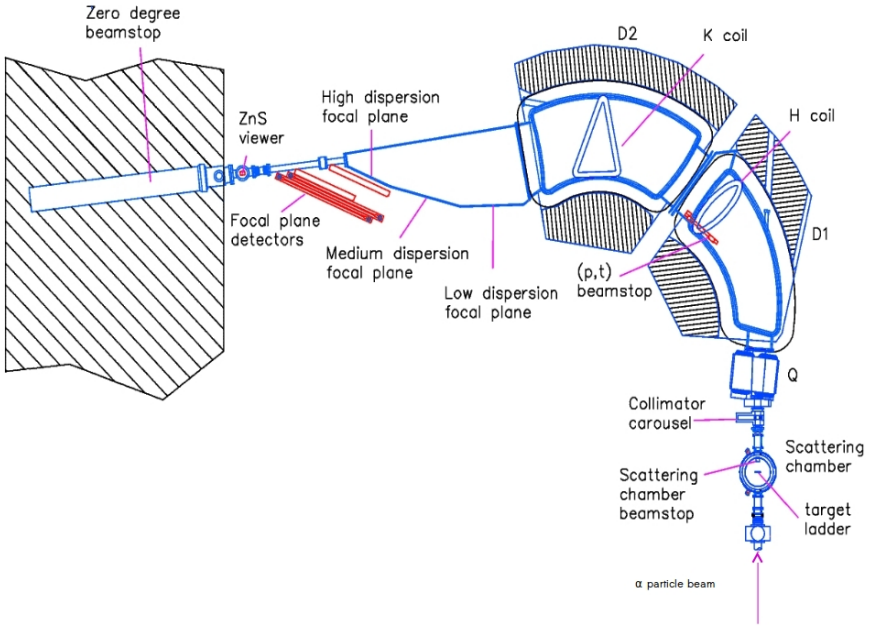

Figure 3.3: Schematic diagram of the zero-degree facility of the K600 magnetic spectrometer (taken from [3]).

transfer. In addition, states with low spin and natural parity are also favoured. This allows for a simplification of the analysis of the multiple contributions to the spectra owing to the complex nature of the nuclear interaction [61]. Only a few facilities exist worldwide where high energy-resolution measurements such as these can be performed. Magnetic spectrometers like the K600 allow for the primary beam to be separated from the inelastically scattered particles or reaction products at zero degrees [63].

The GMR centroid energy is normally combined with contributions from other resonances, predominantly the IVGDR and the ISGQR. Very-selective measurements are, therefore, required [46]. The use of the 0° mode results in measurements that allow for the disentangling of the GMR from the contributions of the other resonances, since the GMR is strongly excited in forward-angle scattering.

The beam passes just 10 cm away from the focal-plane detectors in zero-degree

mode, which is why very low halo conditions are required. The focal-plane detectors are placed in the high-dispersion focal plane to ensure good separation of the beam from the lowest measurable excitation energy such that the required excitation-energy region is measured [64]. After the beam passes through the spectrometer, it moves through the zero-degree beamline towards the zero-degree beamdump, which is a Faraday cup embedded in the concrete wall of the spectrometer vault. The zero-degree beamline includes a scintillating viewer that sits before the entrance to the zero-degree beam dump as shown in Fig. 3.3 [3]. The scintillating viewer is used to assist with the optimisation of the transport through the spectrometer.

3.2.2 Focal-plane detectors

The focal-plane detector package is made up of two plastic scintillation detectors and two Multi-Wire Drift Chambers (MWDCs). After having gone through a flight path of approximately 8 metres from the target, the nuclear-reaction products are detected by the focal-plane detectors [62].

3.2.2.1 Multi-wire drift chambers

Each MWDC contains an X wire plane and a U wire plane. The X wire planes allow for the determination of the horizontal (x) position along the length of the focal plane, while the combination of the X and U wire planes allows for the determination of the vertical (y) position. In the X wire plane, the wires are placed at 90° to the horizontal (that is, perpendicular to the scattering plane) while the wires of the U wire plane are inclined at 50° from the horizontal.

The X wire plane consists of 198 gold-plated tungsten signal wires, spaced 4 mm apart where each signal wire has a diameter of 20 μm, and 199 gold-plated tungsten field-shaping wires that have a diameter of 50 μm each and are placed

at equal distances between the signal wires [45]. The U wire plane has 143 gold-plated tungsten signal wires and 144 gold-plated tungsten field-shaping wires, which have the same diameters and placement as the corresponding wires in the X wire plane [45]. The motivation behind the use of gold-plated tungsten is that gold has a high resistance to corrosion as well as a high work function [65] and tungsten has high tensile strength [66]. Three cathode planes that are made of aluminium foil sandwich the wire planes. Two mylar sheets are used to isolate the interior of the MWDCs from the atmosphere. This particular combination of material was chosen as it prevents fast diffusion of moisture from the experimental area to the inside the of the MWDCs, thus preventing current leakage and sparking inside the detector [45]. The trajectory of the charged particle is detected through the ionisation of gas molecules. Between the two mylar planes is a gas mixture of 90% Ar and 10% CO_2 that is used as the medium for the ionisation [45].

3.2.2.2 Plastic scintillator detectors

The plastic scintillators are used for two purposes. The first is for triggering, where the plastic scintillators provide the trigger for the data acquisition system (discussed in Section 3.3) as well as the common reference time for the drift-time determination in the data [3]. The second is for particle identification using energy-loss information from the ΔE - ΔE particle identification spectra [3].

Two plastic scintillators (also called paddle detectors as a result of their geometry) are located immediately downstream of the MWDCs. The two paddle detectors are $1/2''$ and $1/4''$ thick and are wrapped in aluminised mylar sheets such that no ambient light enters. Photomultiplier tubes are connected vertically to both ends of the plastic scintillators with the use of 90° twisted-pair adiabatic lightguides. This configuration is important as it allows for the plastic scintillators to be placed close to the beampipe [3]. The signals from the

photomultiplier tubes are sent to the Time-to-Digital Converters (TDCs) via 16-channel twisted-pair ribbon cables.

3.3 Data acquisition system and electronics

The K600 Data AcQuisition (DAQ) system is composed of electronics that are in accordance with the Nuclear Instrumentation Module (NIM) standard and that are used to generate the trigger signal [67]. An in-depth explanation of the DAQ can be found in Ref. [62], a brief outline is presented here for completeness. A separate group of electronics that are in accordance with the Versa Module Europa (VME) standard are used to digitise the Time-Of-Flight (TOF), the MWDC drift-time measurements, the measurement of charge that accumulates in the paddles and also to accumulate the scalar signals. Wire-plane signals are pre-amplified and then discriminated by the 16-channel electronic cards that are situated on the PC board of the MWDCs. These signals are then transported to the CAEN V1190A TDCs. The TDCs can achieve 100 ps resolution via the 16-channel twisted-pair ribbon cables.

The photomultiplier tubes send signals that are digitised by a 12-bit current-integrating CAEN V792 Charge-to-Digital Converter (QDC). The coincidence of the two plastic scintillators forms the trigger for the Maximum Integrated Data Acquisition System (MIDAS) [67]. It is assumed that both plastic scintillators are operating at 100% efficiency for the detection of heavy charged particles. MIDAS was developed to create and store event files and is widely used in physics experiments [67]. The acquired files are analysed offline using software called ROOT, which was developed at Counseil Europeen pour le Recherche Nucleaire (CERN). The offline analysis is performed with codes written in the C++ programming language. These codes were developed at iThemba LABS.

3.4 Target preparation

The required targets for this experiment were all manufactured in the iThemba LABS target laboratory. The requested parameters vary according to the experiment but some requirements are common. These include good mechanical strength, stability under the beam, and high chemical purity (also known as isotopic enrichment) [68].

The target preparation method is dependent on many factors such as chemical and physical properties, the type of target needed, and the target thickness required [68]. The magnesium material used during the manufacturing process was supplied by the Oak Ridge National Laboratory in ingot form. An ingot is a piece of a relatively pure metal that is cast into a suitable shape that allows for further processing. The highly ductile property of magnesium allows for the rolling of the material as supplied.

The technique of rolling, although complex by nature, should be considered as one of the primary methods of target preparation for nuclear-structure experiments [68]. This method is known for producing high-quality targets with minimal wastage. Rolling allows for the reshaping of the target material with the use of a rolling mill. The material is placed in a rolling pack, which protects the material from collecting impurities from the rollers but also assists with the reshaping. The rolling pack is usually made out of stainless steel and allows for great precision in terms of target thickness.

The reduction in thickness during the rolling process should not be greater than 10–15% in a single roll during the initial stage of rolling and no more than 5–8% in later stages. These values are only guidelines but are dependent on the malleability as well as the hardness of the material being rolled [68]. If the target thickness is excessively reduced, disruption and damage of the crystal structure may be induced, which will either lead to disintegration or the rolled target will get stuck to the rolling pack. The interior of the rolling

pack should, therefore, at all times, be kept dust free, free from scratches and free from fingerprints so as to exponentially reduce the chances of damaging the rolled target [68]. In the case of reducing the thickness of harder materials, interstep annealing is recommended for stress relaxation [68].

Finally, the effort required to refine the rolling procedure is rewarded by gaining a target that exhibits a more-robust behaviour when bombarded with heavy ions than foils of the same thickness that are produced by vacuum evaporation-condensation [68].

The material for the ^{58}Ni and ^{90}Zr targets was supplied by Isoflex USA in the form of a metal powder. The powder was first compressed into a pellet that was then transferred into a copper boat or crucible. The material was then melted in a vacuum. The resulting bead was mechanically rolled down to the required thickness. A summary of the various thicknesses and isotopic enrichment of the targets can be seen in Table 3.1.

Table 3.1: Details of targets used in this study

Target	Z	N	Areal density (mg/cm^2)	Isotopic enrichment (%)
^{24}Mg (calibration)	12	12	0.23 ± 0.005	99.94
^{58}Ni	28	30	0.7 ± 0.05	99.48
^{90}Zr	40	50	0.9 ± 0.05	96.80

3.5 Experimental techniques and methods

3.5.1 Kinematic correction

Kinematic correction is one of the first processes in obtaining high energy-resolution. This is done by adjusting the magnetic-spectrometer field in such a way that a nuclear state will appear to be upright in the spectrum of x_{fp} *versus* θ_{fp} [3]. Simply explained, this is the convergence of particles from the

same state at the same point in x_{fp}, but with different θ_{fp} values [3]. Changing the K-coil, that is, adjusting $(x|\theta)$ for first-order focusing and then changing the H-coil for the correction of the $(x|\theta^2)$ aberrations allows for the aforementioned convergence. The kinematic-correction procedure alters the ion-optical properties of the spectrometer [69]. This must, therefore, be achieved before the coefficients of focus matching as well as lateral and angular dispersion matching can be adjusted properly.

3.5.2 Dispersion matching

Cohen (1959) [70] showed that if a spectrometer is "matched" to the beamline properly then the spectral resolution will be better than the beam resolution up to the limit of the resolving power of the analysing spectrometer. Therefore, if optimum resolution is to be obtained (which is critical in a fine-structure investigation), proper matching of the incident beam to the K600 spectrometer is extremely important. A "normal" or achromatic beam is set up such that the position and angle of the particles on the target are independent of the momentum of the incident particle. If the beamline is set up in this manner, the inherent momentum/energy distribution of the beam limits the energy resolution of detection in the K600 focal plane. This problem can be overcome by dispersion matching [69]. A dispersion-matched beam can spatially separate the particles according to their momentum. Those particles with a higher momentum will travel a longer distance through the spectrometer in comparison to those with a lower momentum. This will then effectively achieve achromatic focus in the focal plane. What is then obtained is an excitation-energy spectrum with high energy-resolution; however, a high energy-resolution absolute-energy spectrum is not achieved, ensuring that the sensitivity of the nuclear reaction to the varying beam energies is negligible as a result of the energy spread of the beam being small enough.

There are three different beam optical modes [71]: the achromatic mode, the

lateral-dispersion mode and the angular-dispersion mode, which are described briefly below. These modes are schematically depicted in Fig. 3.4.

Achromatic mode: In this mode, the beam is focussed directly at the target. The focal-plane position and the angle of the detected particles in the K600 magnetic spectrometer are then dependent on the initial energy spread of the beam at the target. This will effectively limit the energy resolution [69].

Lateral-dispersion mode: In this mode, a vast improvement in the focal-plane energy resolution can be achieved via the matching of the beam dispersion with the focussing properties of the magnetic spectrometer. This is done via the spatial spreading of the beam spot on the target [45].

Angular-dispersion mode: The angular-dispersion mode allows a significant improvement in the horizontal scattering resolution. In this mode, the incident angles of the incoming beam to the target are matched so that the particle position and the focal-plane angle are independent of the initial beam energy spread. This mode is crucial for zero-degree measurements where the highest-possible energy resolution is the aim [26].

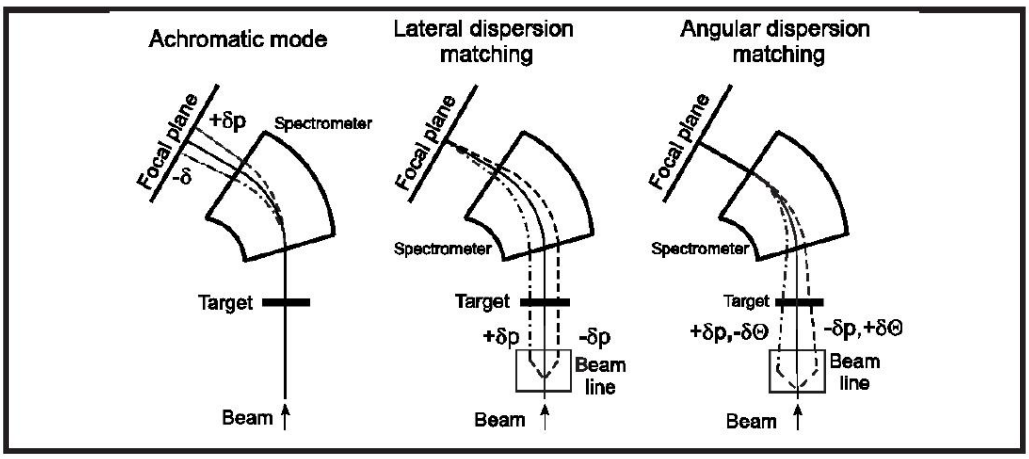

Figure 3.4: Schematic diagram of the three different dispersion-matching modes (taken from [71]).

3.5.3 Faint-beam technique

If a beam goes directly into the magnetic spectrometer at 0°, it would be easy to analyse the matching conditions from the beam properties in the focal-plane detectors. Problematically though, the detector system is not built to handle normal beam intensities (even those as low as 1 nA) and will, therefore, be damaged [3]. The faint-beam technique is implemented in order to optimise conditions for dispersion matching at zero degrees. Beam attenuation copper meshes are used to lower the intensity of the beam without changing the profile of the beam or its ion-optical characteristics [45].

The faint-beam technique was developed especially for zero-degree measurements. Dispersion matching at finite angles is achieved using the ground state of a suitably chosen calibration nucleus. The K600 magnetic spectrometer, connected to the zero-degree beamdump, limits the observed excitation energies (E_{x}) to 7 MeV or higher [26]. Dispersion matching on an excited state becomes an extremely slow process owing to the low count rate. If, however, the faint beam is in use, the beam can directly and safely be observed in the focal-plane detectors of the magnetic spectrometer. Lateral dispersion matching of the beam to the magnetic spectrometer can then effectively be achieved [26].

3.5.4 Background contributions

High energy-resolution experiments require extremely accurate conditions with regards to beam delivery, especially for experiments at and close to 0°. These conditions must be adhered to strictly in order to achieve the required outcome. The beam in question must have very little halo, a small energy spread and a small emittance. These conditions must remain stable for long periods of time to safeguard the practicality of the required measurements.

Measurements such as this experiment are highly susceptible to any beam fluctuations as well as emergent background fluctuations, which are enhanced for extreme forward-angle scattering reactions, i.e. for those at and close to zero degrees. There exists a small rigidity difference between the projectiles and the scattered particles, which results in the enhancement of fluctuations at zero degrees. It is, therefore, extremely important to minimise the background contributions to the observed focal-plane spectrum. The background contribution becomes apparent in the focal-plane position spectrum and has both beam-related and target-related components.

3.5.4.1 Beam-related background

The beam-related background is also referred to as the beam halo and consists of beam particles, in this case α particles, whose coordinates (in phase space) differ from those of the core beam. The transmission efficiency of the SSC is subject to the limitations of the beam emittance at the accelerator complex and, therefore, a medium-to-high fraction of the total beam that is injected into the SSC is extracted from it [3]. The energy spread is defined using slit 12X (shown in Fig. 3.1). The emittance slits are 12X while 1P is the high-energy slit located after the first bending dipole (B1P) after the SSC. The beam halo is caused by the beam scattering off the slits i.e. the amount of potential interaction points is high. By reducing the beam halo, the number of interaction points is also reduced. To ensure that low beam-halo conditions are achieved, a thin slit at the object point in conjunction with four sets of horizontal and vertical clean-up slits as well as two 90° bending magnets are employed [61]. By reducing the beam-related background contribution during a zero-degree experiment, minimisation of the potential interaction points between the beam halo and the beamline material in the final section of the beamline takes place.

The beam is delivered to the K600 experimental area by the cyclotron beam

operators. The beam spot on the target is then verified as being properly positioned and alignment is achieved [3]. A detailed explanation of how this is achieved can be found in Ref. [62]. The background contribution is then characterised through a measurement done on an empty target while the MWDCs are turned off. The cyclotron operators then optimise the slit positions and opening sizes in an attempt to minimise the detected count rate. In general, before commencement of the experiment, all slits can be optimised; thereafter, the 9X and 12X values should remain constant. This is because the object and emittance slits define the dispersion matching and so, if these values change, the dispersion-matching conditions could worsen. As soon as the count rate reaches an acceptable level, background characterisation takes place using a position spectrum generated for an actual target rather than an empty one [3].

3.5.4.2 Target-related background

The target-related background occurs as a result of the particle beam being elastically scattered off the target and then re-scattered off the hardware within the magnetic spectrometer. A problem arises when these particles are detected by the focal-plane detectors with energies and coordinates that are not significantly different from the inelastically scattered particles interest [3, 61].

A substantial reduction in the background contribution to the focal-plane position spectrum came from the use of a 49 mm collimator with an 11 mm thick lip. A collimator reduces the potential internal scattering within the K600 magnetic spectrometer from target-induced scattering of the top and bottom of the scattering vessel [61].

3.6 Data extraction

For each experimental run, the generated data were stored in an event-by-event format in the previously mentioned MIDAS data format. These files were then analysed offline using the CERN ROOT software package and specialised scripts that were written by users at iThemba LABS in C and C++ programming languages. Many offline procedures that are detailed below had to be followed accurately to ensure that the desired information was extracted from the experimentally obtained data files.

3.6.1 Particle identification

The trajectory of a particle through the focal-plane detector system may have various points of interaction causing characteristic information to be left behind. When a charged particle passes through a detector, some of the energy it carries is lost [3]. This energy loss leaves behind a unique and characteristic footprint. In order to justify and group the detected particles, particle identification, which has proved to be successful in the interpretation of this information, must be performed.

In this set of experiments, TOF selection for particle identification is used.

3.6.1.1 Time-Of-Flight selection

TOF selection is essentially the first step of the offline analysis process. For this selection process, it is important to note that the magnetic field setting of the spectrometer provides information regarding the magnetic rigidity, R, only. No information related to the mass, energy, or charge of the detected particle is provided by the magnetic field setting of the spectrometer. The following equation shows the relationship between the radius of curvature, r, which is

the length of the path travelled by the particle through the spectrometer, the momentum, p, and the magnetic field, B:

$$R = rB = \frac{p}{q}. \tag{3.1}$$

The TOF of a particle is simply defined as the time a particle takes to move from its target-interaction point to the point where it is detected in the focal plane by the focal-plane detector package [3]. During the analysis, the TOF peak was stabilised by offsetting the TOF position across all of the data files. These data files were grouped by nuclei, i.e. all the respective data files related to each nucleus (^{24}Mg, ^{58}Ni, and ^{90}Zr) were grouped together respectively. In Fig. 3.5, a double TOF peak can be seen; however, the most-prominent peak was chosen for the analysis. This particular peak was chosen as it exhibits a higher count rate.

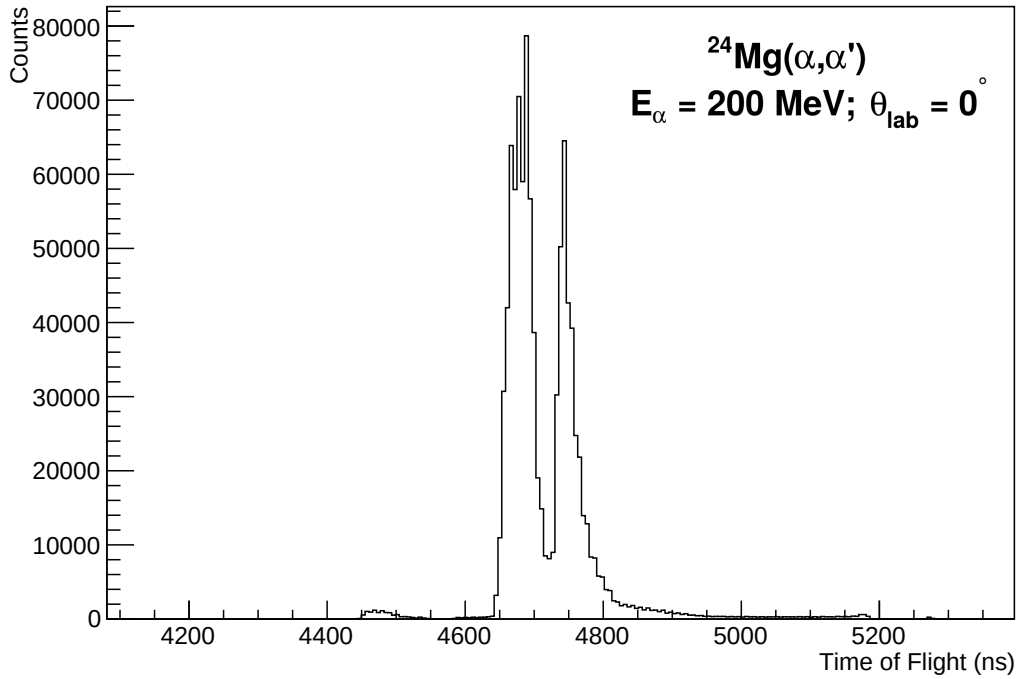

Figure 3.5: Time-Of-Flight before particle identification for particles of interest in ^{24}Mg.

For the purposes of calibration, a ^{24}Mg target was used. Particle IDentification (PID) was performed via the creation of gates shown in Figs. 3.6 and 3.7. TOF selection was done as a function of ΔE in paddle 1 and as a function of the focal-plane position. The application of a PID gate, shown in Fig. 3.7, in addition to that shown in Fig. 3.6 allowed for further and more-precise α-particle identification.

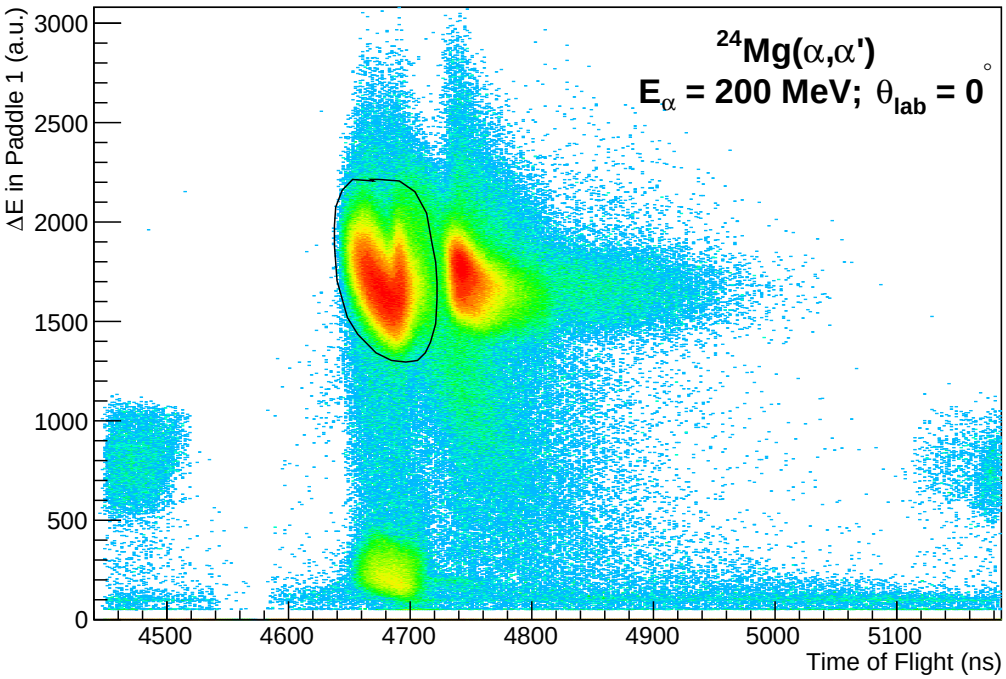

Figure 3.6: The pulse height in paddle 1 plotted as a function of Time-Of-Flight (ns). The black line indicates the selected region of interest for ^{24}Mg(α, α')

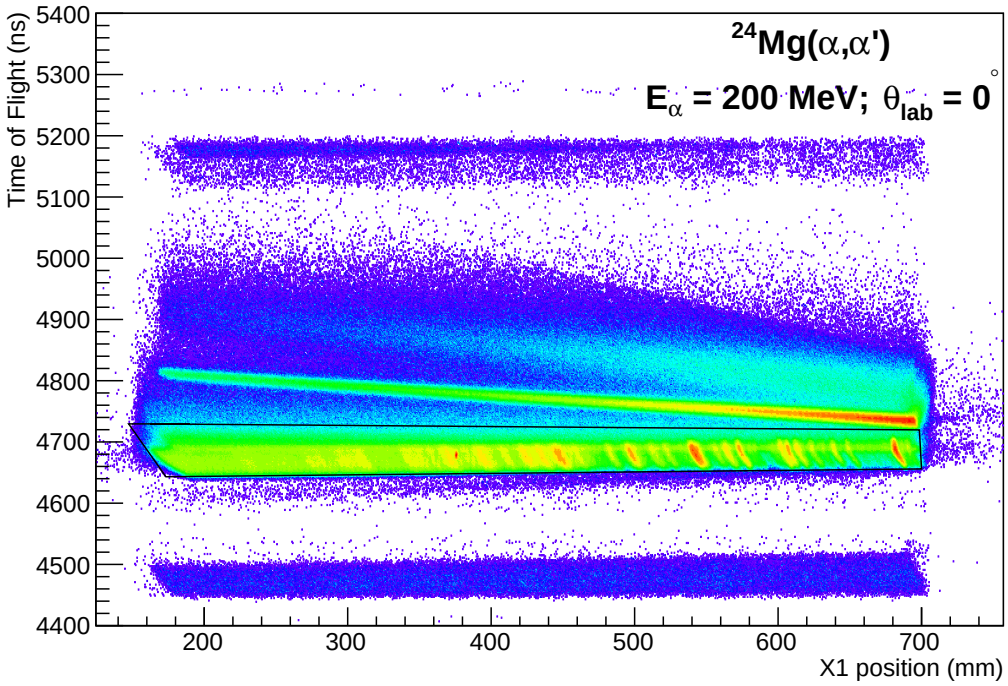

Figure 3.7: Time-Of-Flight (ns) plotted as a function of x_{fp} (mm). The black line indicates the selected region of interest for ^{24}Mg(α, α')

3.6.2 MWDC data extraction

The procedures to obtain accurate focal-plane position information are briefly outlined here, a more in-depth explanation can be seen in Refs. [3] and [62]. The implementation of these procedures is necessary to obtain accurate focal-plane spectra.

3.6.2.1 MWDC operation and focal-plane position determination

A ray-tracing algorithm is used to determine the focal-plane coordinates. The focal-plane coordinates, in turn, are used to measure the drift times in the drift cells of the MWDCs. The measured drift times are translated to drift distances. Variations in ribbon-cable lengths lead to variations in measured

drift times for which corrections must be made. Corrected drift times are more accurate and will eventually contribute to higher accuracy in the excitation-energy spectra. The cable-length-correction procedure is described in detail in [45] and has been automated in a script by J. J. van Zyl written in C++. As a result, any observed variations in the cable lengths now require only minor adjustments.

Drift times are mapped to the associated drift distances by what is known as a Look-Up-Table (LUT). LUTs may require offsets so that the mapping is fully optimised. Figure 3.8 shows the two-dimensional resolution spectra before (upper) and after (lower) the application of a LUT offset to the MWDC U1.

The effect of a LUT offset can be described as the sensitivity of the mapping between drift times and drift distances. For short distances, this sensitivity is the highest. The upper panel of four in Fig. 3.8 provides an example of the Res2D spectra for the case where a U1 LUT is necessary. The need for offsets is determined by the extent to which the central region of the Res2D spectra is misaligned. The inclusion of a LUT offset allows for alignment of the central regions, which can be seen in the lower panel of Fig. 3.8.

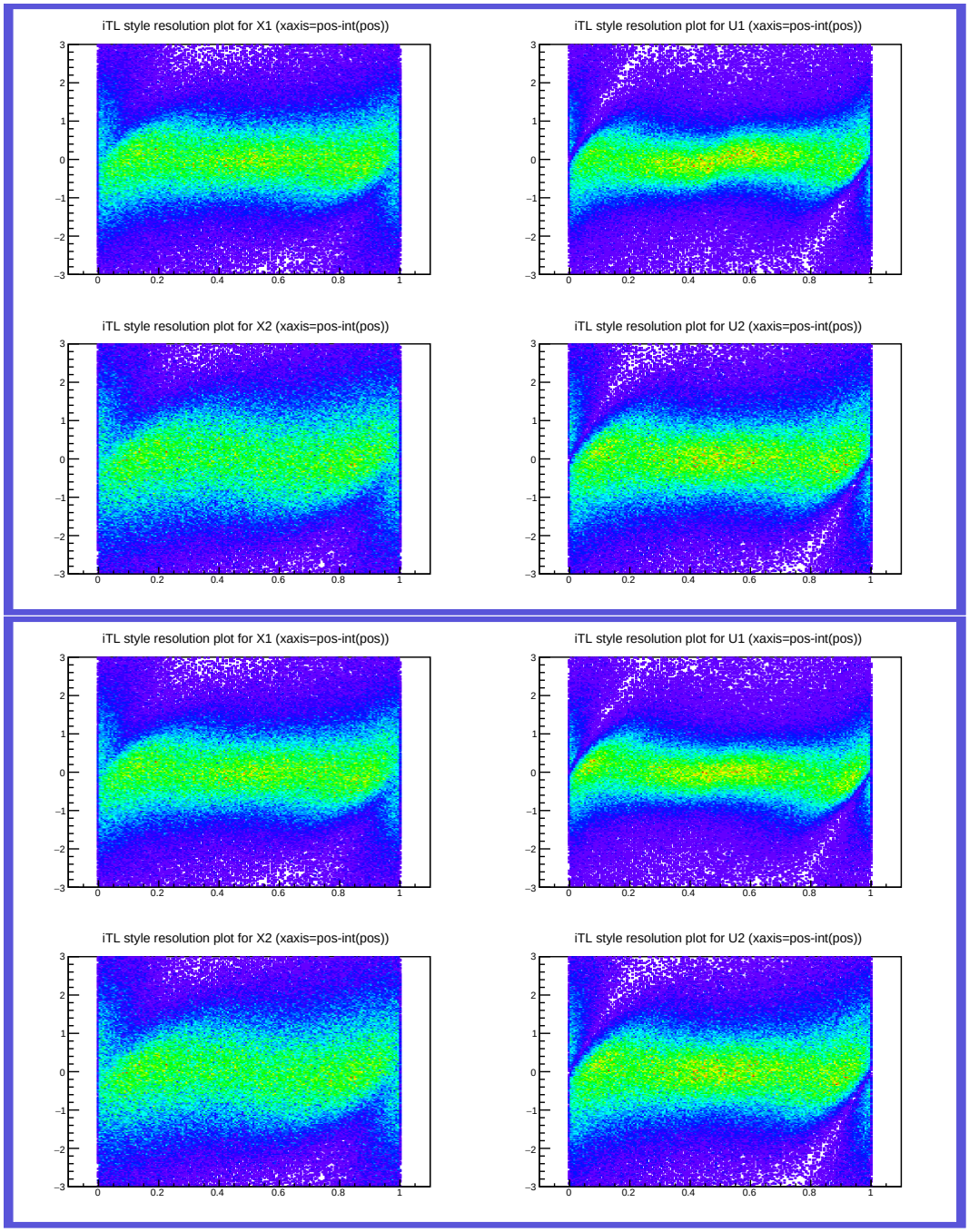

Figure 3.8: Two-dimensional resolution spectra before (*upper*) and after (*lower*) LUT offsets for U1.

3.6.2.2 Position resolution

The track angle on both sides of the wire plane should be approximately constant for any n-wire MWDC event. The difference in slopes is calculated as:

$$D = \frac{d_{t(1)} - d_{t(2)}}{\text{wire separation}} - \frac{d_{t(n-1)} - d_{t(n)}}{\text{wire separation}} \tag{3.2}$$

which should, preferably, equal zero. The variable $d_{t(i)}$ is the drift distance that is calculated from the drift time t of the ith wire. Statistical fluctuations from a number of events lead to a distribution of values around zero.

The accuracy in the position of the drift chamber is given by:

$$\sigma_x = \frac{\sigma_{\mathrm{c}}}{\sqrt{n}} = \frac{\sigma_D}{2\sqrt{n}} \tag{3.3}$$

and was derived in [72]. The variables σ_c and σ_D are the intrinsic cell accuracy and the standard deviation of the difference in the slopes (from Eq. (3.2)), respectively. The number of wires used to determine the position is denoted by n. The intrinsic Full Width at Half Maximum (FWHM) position resolution of the drift chamber can be calculated as:

$$\mathrm{FWHM_{pos}} = 2.35 \times \sigma_x = 2.35 \times \frac{\sigma_{\mathrm{c}}}{\sqrt{n}} = 2.35 \times \frac{\sigma_D}{2\sqrt{n}}. \tag{3.4}$$

3.6.2.3 MWDC efficiency

The MWDC efficiency is an indication of the extent to which a specified MWDC can detect charged particles in the focal plane and is determined as follows:

$$\epsilon = \epsilon_{\mathrm{g}} \cdot \epsilon_{\mathrm{i}}. \tag{3.5}$$

ϵ_g is the geometric efficiency and is assumed to be 100%. This experiment runs in the vertically focused ion-optical mode. In this mode, the α-particles of a

chosen rigidity have been measured to be well focused in the vertical direction of the focal-plane position.

The intrinsic efficiency ϵ_{i} is calculated as follows:

$$\epsilon_i = \frac{N_{\mathrm{accepted}}}{N_{\mathrm{total}}}, \tag{3.6}$$

where N_{total} is the total number of recorded events for a chosen rigidity in the focal plane and N_{accepted} is the number of those recorded events that are valid. The validity of an event is determined by the following:

- gated regions should contain the TOF and scintillator signals,
- the number of hit wires should be between 3 and 6,
- reduced chi-squared should be less than 1 and
- gated regions should also contain the drift times.

3.6.2.4 Angle calibration

Angle calibration is performed: to convert the horizontal focal-plane angle (θ_{fp}) to the horizontal scattering angle (θ_{scat}), and to allow for lineshape corrections (discussed in Section 3.7.1) based on θ_{scat}. Although angular dispersion matching was not performed during this experiment, the horizontal scattering angle resolution provided enough information to carry out a horizontal angle calibration.

The traditional method for this calibration is to take a series of measurements at a finite angle using a multi-hole collimator. This method was not performed during this experiment, and so, the reconstruction of the horizontal scattering angle had to be done manually using a non-traditional method. Angle calibration is composed of a θ_{fp} to θ_{scat} conversion where the parameters of such

an equation need to be determined. The equation in its general form is given by:

$$\theta_{\rm scat} = (a_1 x_{\rm fp} + a_0)\theta_{\rm fp} + (b_1 x_{\rm fp} + b_0). \tag{3.7}$$

The aim of this calibration procedure is to determine parameters a_1, a_0, b_1 and b_0.

Figure 3.9 was used to select a number of points. These points were then used to plot the focal-plane angle as a function of the different focal-plane positions. Shown in Fig. 3.10 is the series of $\theta_{\rm fp}$ to $\theta_{\rm scat}$ conversions for three different focal-plane positions. The values of the slopes of each of these three graphs were then plotted as a function of $x_{\rm fp}$ as shown in Fig. 3.11. The parameters a_1 and a_0 were found from the slope and offset of this graph, respectively. The parameters b_1 and b_0 were determined by plotting the offsets from the three graphs as a function of $x_{\rm fp}$.

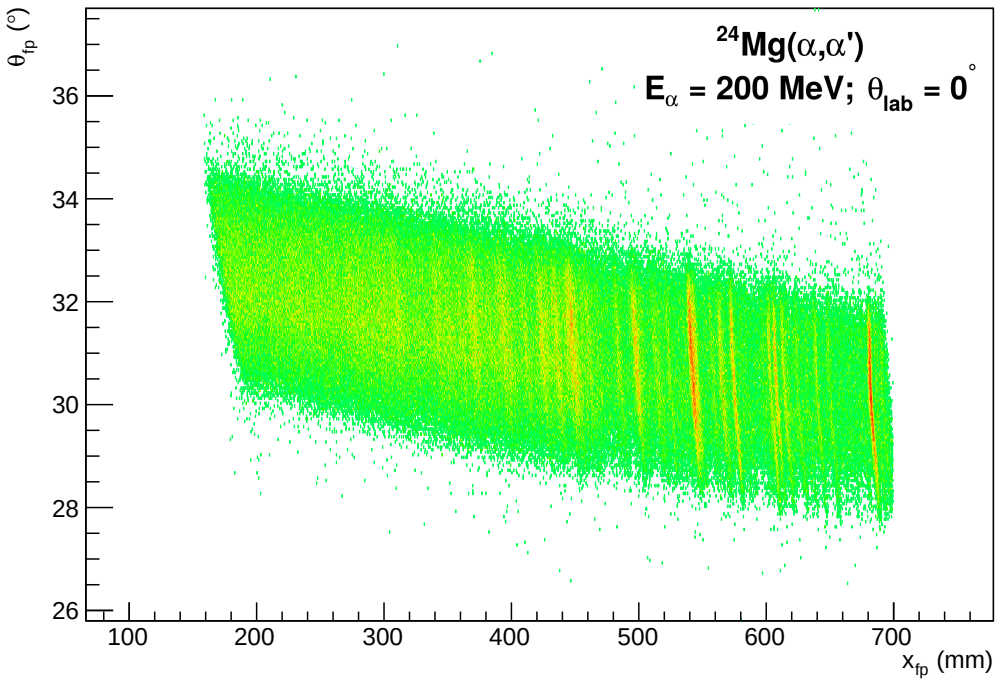

Figure 3.9: $\theta_{\rm fp}$ plotted as a function of $x_{\rm fp}$ (mm) used for the reconstruction of the horizontal scattering angle ($\theta_{\rm scat}$).

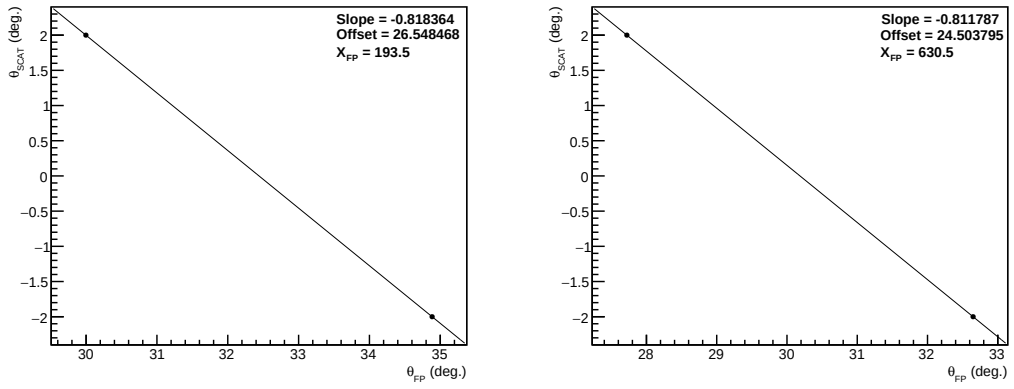

Figure 3.10: The conversion of focal-plane angle (θ_{fp}) to scattering angle (θ_{scat}) for spectra with different focal-plane positions.

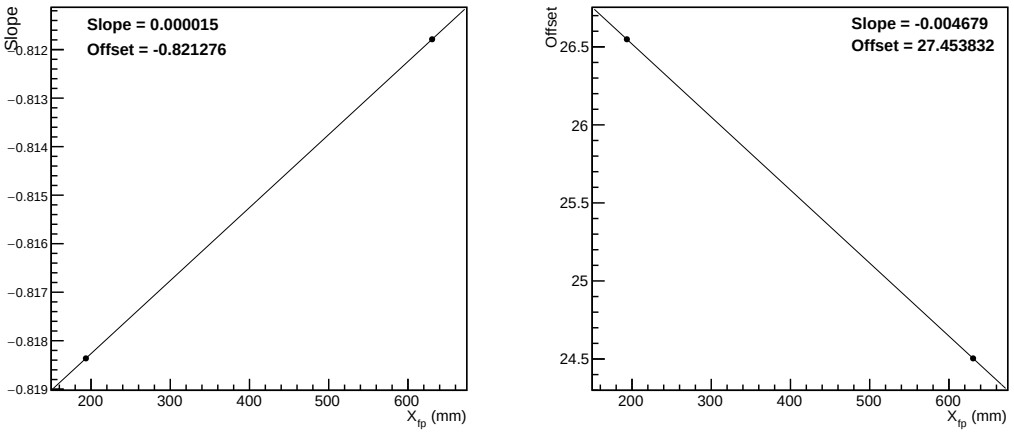

Figure 3.11: *Left*: The slope as a function of the focal-plane position (x_{fp}). *Right*: The offset as a function of the focal-plane position (x_{fp}).

3.7 Data optimisation

3.7.1 Lineshape correction

Lineshape correction is an integral part of the data-optimisation process and is needed to obtain the best-possible energy resolution. The angular depen-

dence of the focal-plane position for any nuclear state that remains following the kinematic correction procedure is corrected for using lineshape correction. A wide excited state is indicative of an uncorrected angular dependence, and, although the use of the K- and H-coils during the experiment provides a reasonable beginning point, further offline adjustments are needed. These offline adjustments serve to ensure that an upright and well-resolved state is obtained.

To get an idea of the amount of correction needed, point markers were placed at regular intervals along a chosen state in the spectrum of $\theta_{\rm scat}$ plotted as a function of $x_{\rm fp}$ for the calibration target. In this case, the most prominent peak situated at approximately 683 mm in Fig. 3.13 was used. A calibration target was used because of the presence of distinct and well-documented excited states obtained from the available literature pertaining to similar experiments. Point markers were used so as to reproduce the overall shape of the line. These points were then plotted on a separate canvas and fitted with a fifth-order polynomial given by:

$$f(\theta) = f_0 + f_1\theta_{\rm scat} + f_2{\theta_{\rm scat}}^2 + f_3{\theta_{\rm scat}}^3 + f_4{\theta_{\rm scat}}^4 + f_5{\theta_{\rm scat}}^5. \qquad (3.8)$$

The fit is shown in Fig. 3.12 with the resulting fit parameters given in the bottom-right corner. The required lineshape-correction equation is, thus, given by:

$$X_{C_i} = x_{\rm fp} - (f_0 + f_1\theta_{\rm scat} + f_2{\theta_{\rm scat}}^2 + f_3{\theta_{\rm scat}}^3 + f_4{\theta_{\rm scat}}^4 + f_5{\theta_{\rm scat}}^5). \qquad (3.9)$$

Figure 3.13 illustrates the overall effect of the application of the lineshape correction. The upper panel shows the prominent excited states in a $x_{\rm fp}$ *versus* $\theta_{\rm scat}$ scatterplot without the application of the lineshape correction, while the lower panel shows the prominent excited states after the application of the lineshape correction.

As previously mentioned, lineshape correction is required to obtain the best-possible energy resolution and will, therefore, affect the focal-plane spectrum. Figure 3.14 shows the effect of the lineshape correction on the focal-plane spectrum of ^{24}Mg. The lower panel of Fig. 3.14 shows a significant reduction in the FWHM of the most-prominent peak when compared to the upper panel. A reduction in the FWHM is indicative of a better energy resolution. It is important to note here that all spectra displayed after this section will take this correction into account.

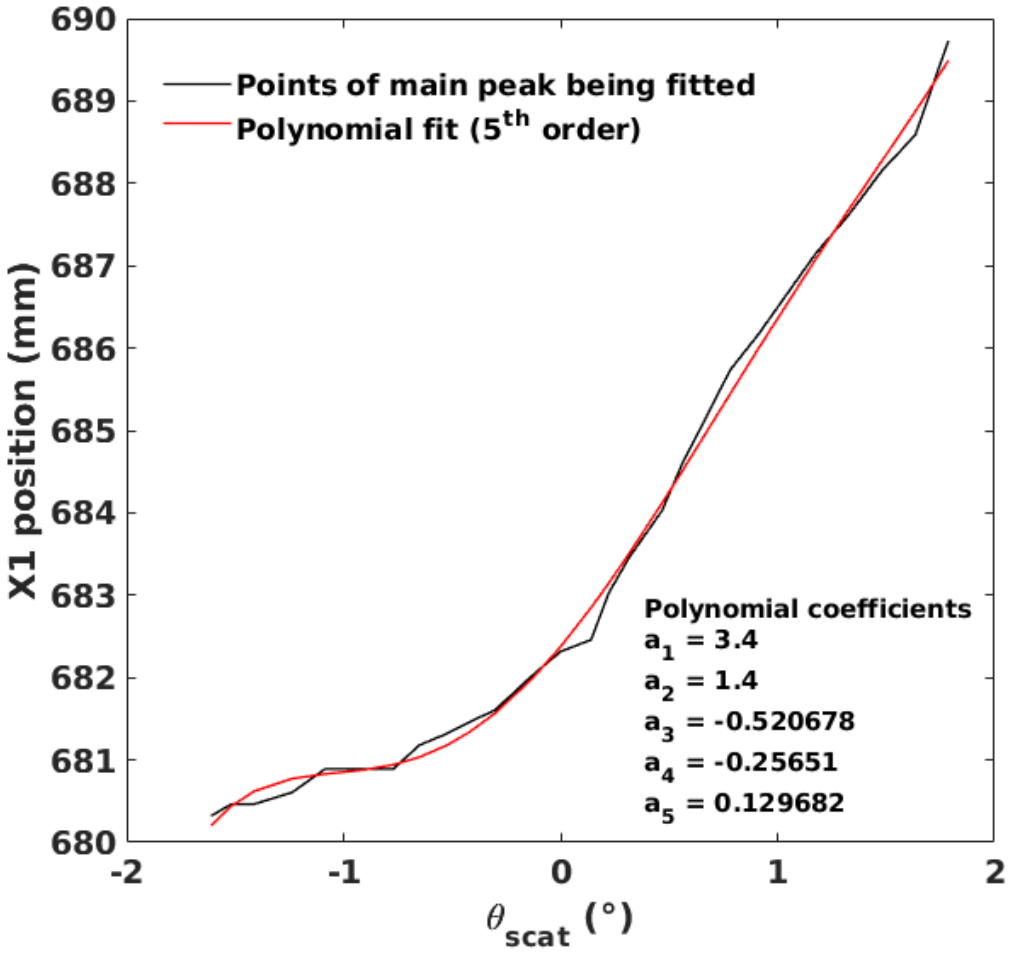

Figure 3.12: The points used to reproduce the lineshape of a chosen state. The fit parameters are given in the bottom-right corner.

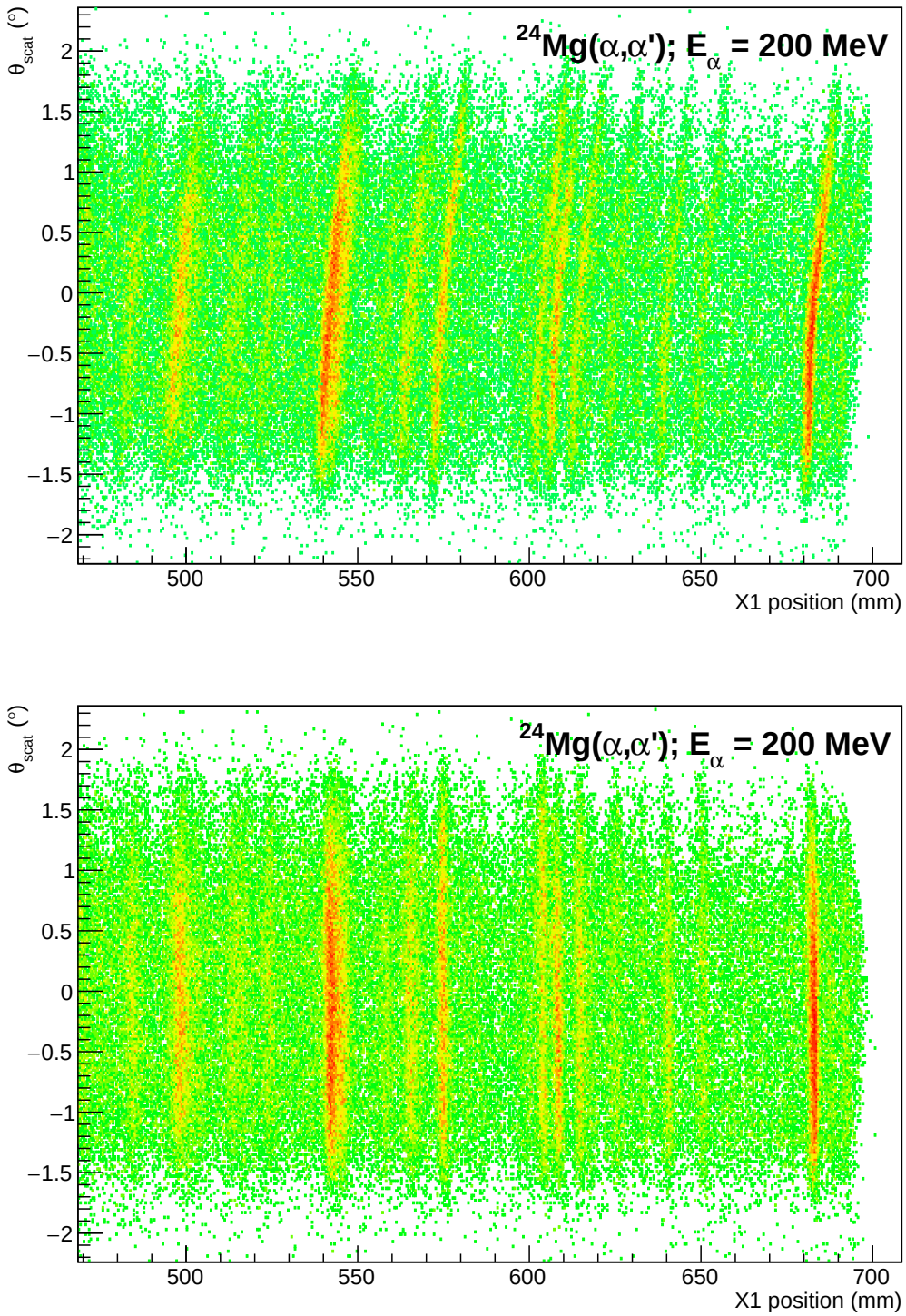

Figure 3.13: The effect of lineshape correction. *Upper*: Prominent excited states in the x_{fp} *versus* θ_{scat} scatterplot with no lineshape correction applied. *Lower*: The scatterplot of the prominent excited states after the application of the lineshape correction.

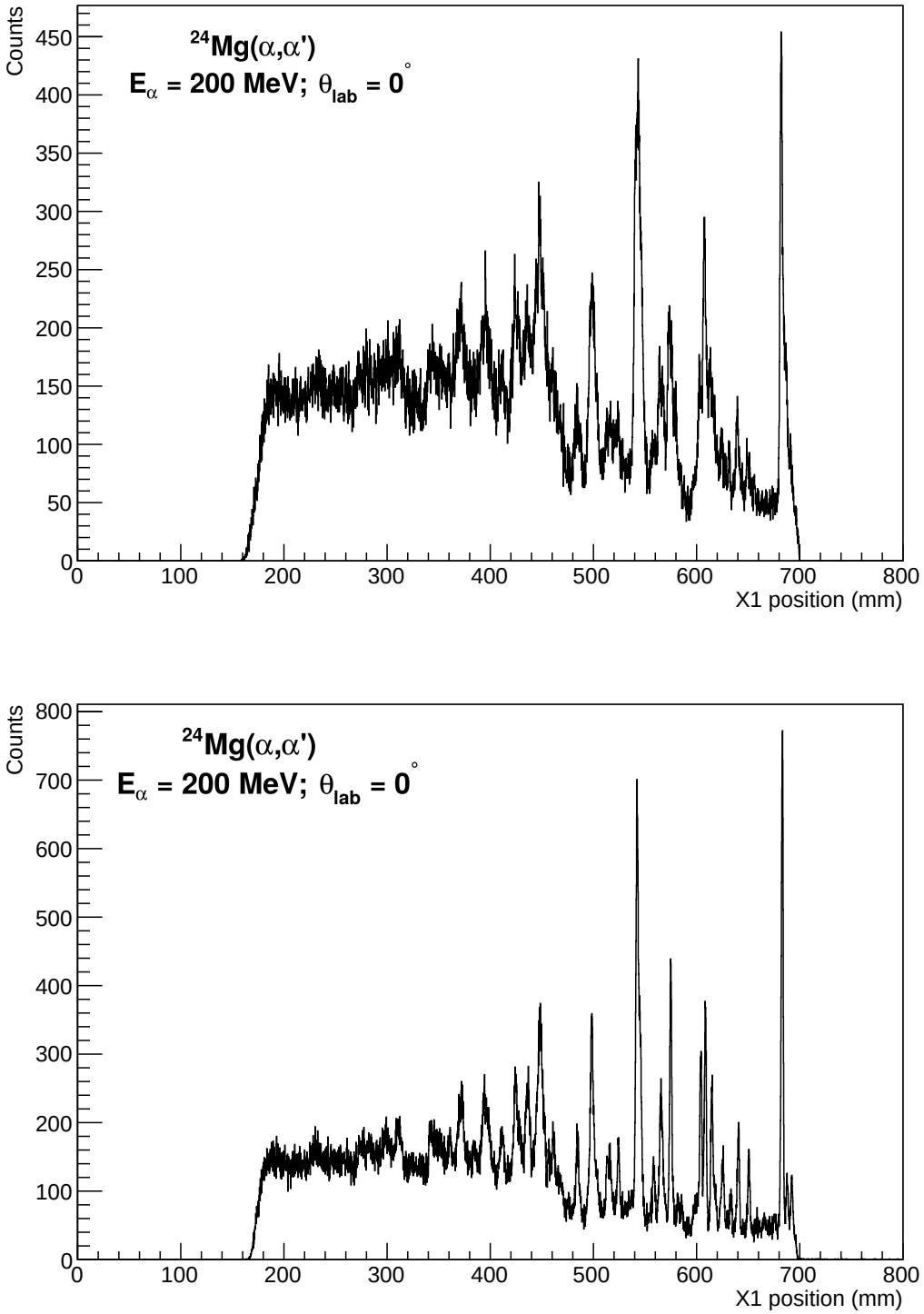

Figure 3.14: *Upper*: Focal-plane position spectrum before lineshape correction for ^{24}Mg. *Lower*: Focal-plane position spectrum after the application of the lineshape correction for ^{24}Mg.

3.7.2 Background subtraction

This experiment involved the spectrometer being operated in vertical focus mode so as to reduce the target-related background. In vertical focus mode, the area of interest is generally centred around $y_{\text{fp}} = 0$. This mode also means that the target- and beam-related background events should be evenly distributed in the vertical plane.

During this experiment, positioning the spectrum around $y_{\text{fp}} = 0$ resulted in an unsatisfactory amount of beam-halo events for certain nuclei. The spectrum was, thus, slightly shifted owing to the change in the vertical beam position on the target. This occurred for the calibration target as well as for ^{58}Ni and resulted in an unequal distribution of the background events above and below the area of interest (shown in Figs. 3.15 and 3.16). For ^{90}Zr, however, the events of interest are evenly distributed around $y_{\text{fp}} = 0$ (illustrated in Fig. 3.17). The background-subtraction method for this type of evenly distributed spectrum is detailed in [26] and is reliant on the x_{fp} *versus* y_{fp} spectrum having two equal background regions on either side of the region of interest as shown in Fig. 3.17.

The background-subtraction method used for ^{90}Zr had to be adjusted for the other nuclei in this experiment. The adjusted background-subtraction method is detailed in [3]. Figures 3.15 and 3.16 show the x_{fp} *versus* y_{fp} as well as the y_{fp} projection. The total area of this projection is made up of both the events of interest and the background events. The number of events contained in the region of interest was identified and a corresponding area from the background sections, which contained the same number of events as the area of interest, was also identified. This background region was subtracted in two equal portions from the raw data. The result of this background-subtraction method ensured that the correct amount of background was subtracted without introducing structure into the region of interest. The resulting focal-plane position spectra obtained from both background-subtraction methods are shown in Fig. 3.18.

The upper panel illustrates the background-subtraction method for events of interest not centered around $y_{\mathrm{fp}} = 0$, while the lower panel illustrates the background-subtraction method for events of interest centered around $y_{\mathrm{fp}} = 0$. For completeness, the background-subtracted focal-plane position spectrum for ^{24}Mg after the application of the lineshape correction is shown in Fig. 3.19.

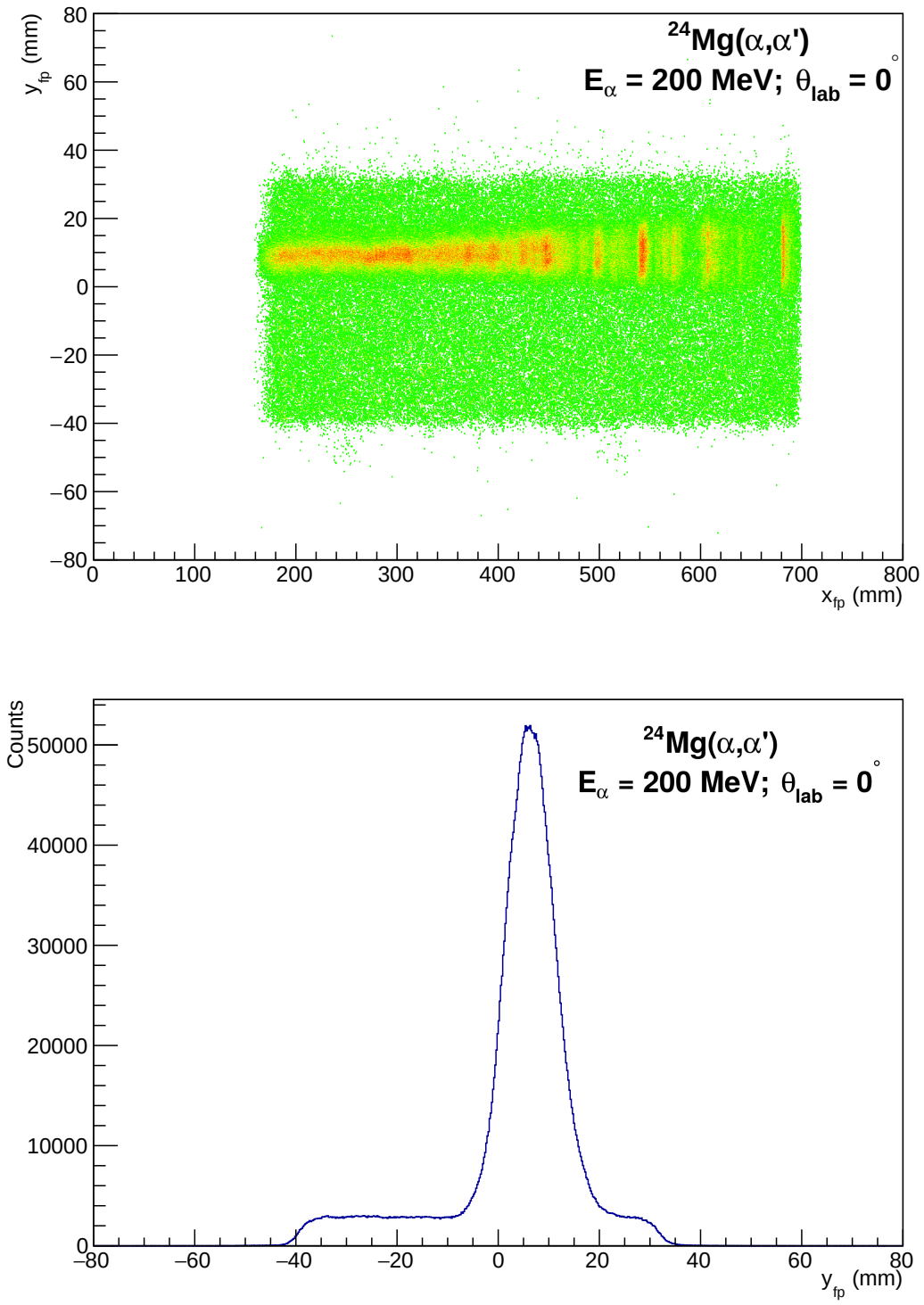

Figure 3.15: *Upper*: The two-dimensional x_{fp} (mm) *versus* y_{fp} (mm) scatter-plot for the calibration target ^{24}Mg. *Lower*: The y_{fp} projection of the focal-plane events show a shift owing to a change in the vertical beam position on the target.

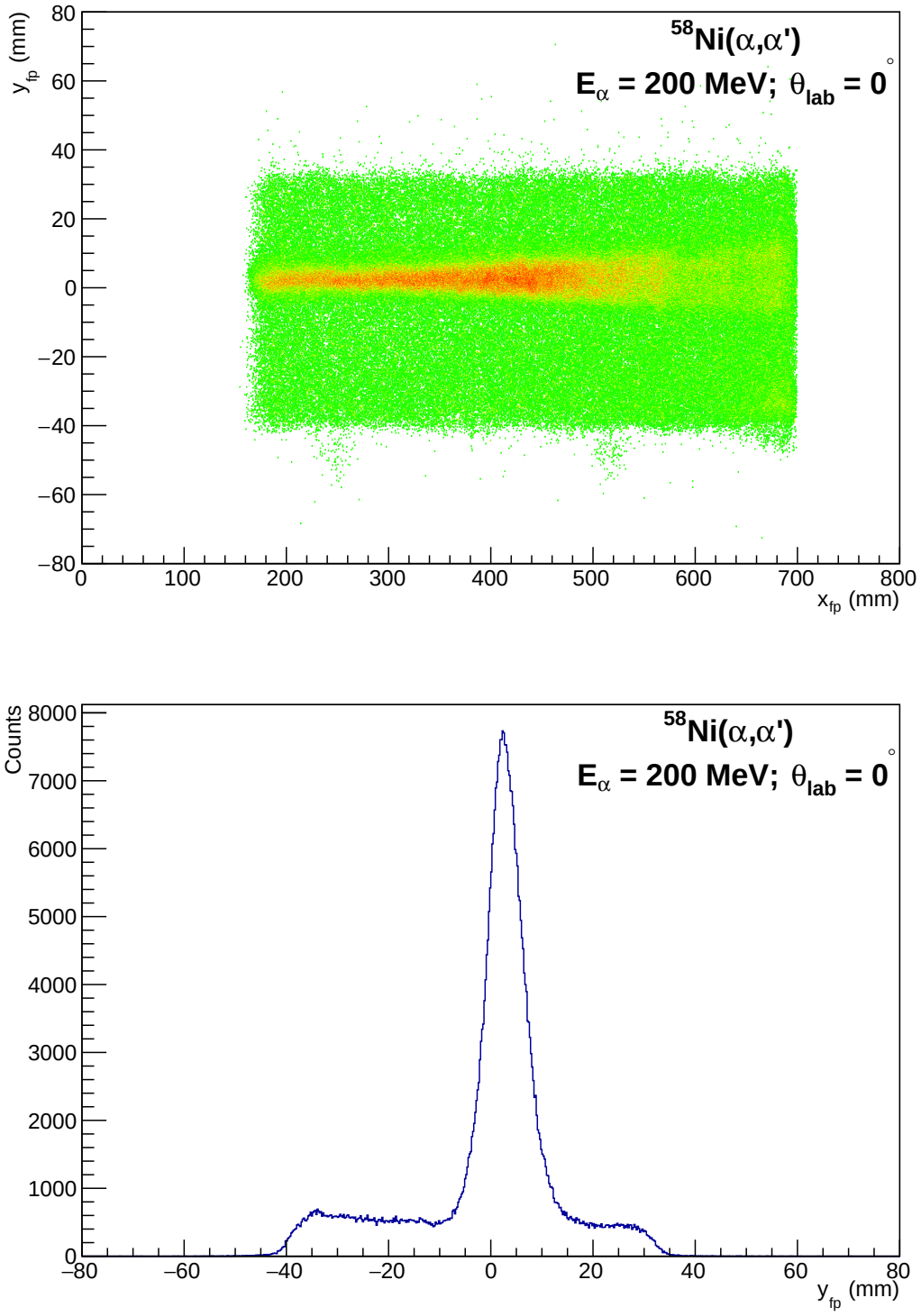

Figure 3.16: *Upper*: The two-dimensional x_{fp} (mm) *versus* y_{fp} (mm) scatterplot for ^{58}Ni. *Lower*: The y_{fp} projection of the focal-plane events show a shift owing to a change in the vertical beam position on the target.

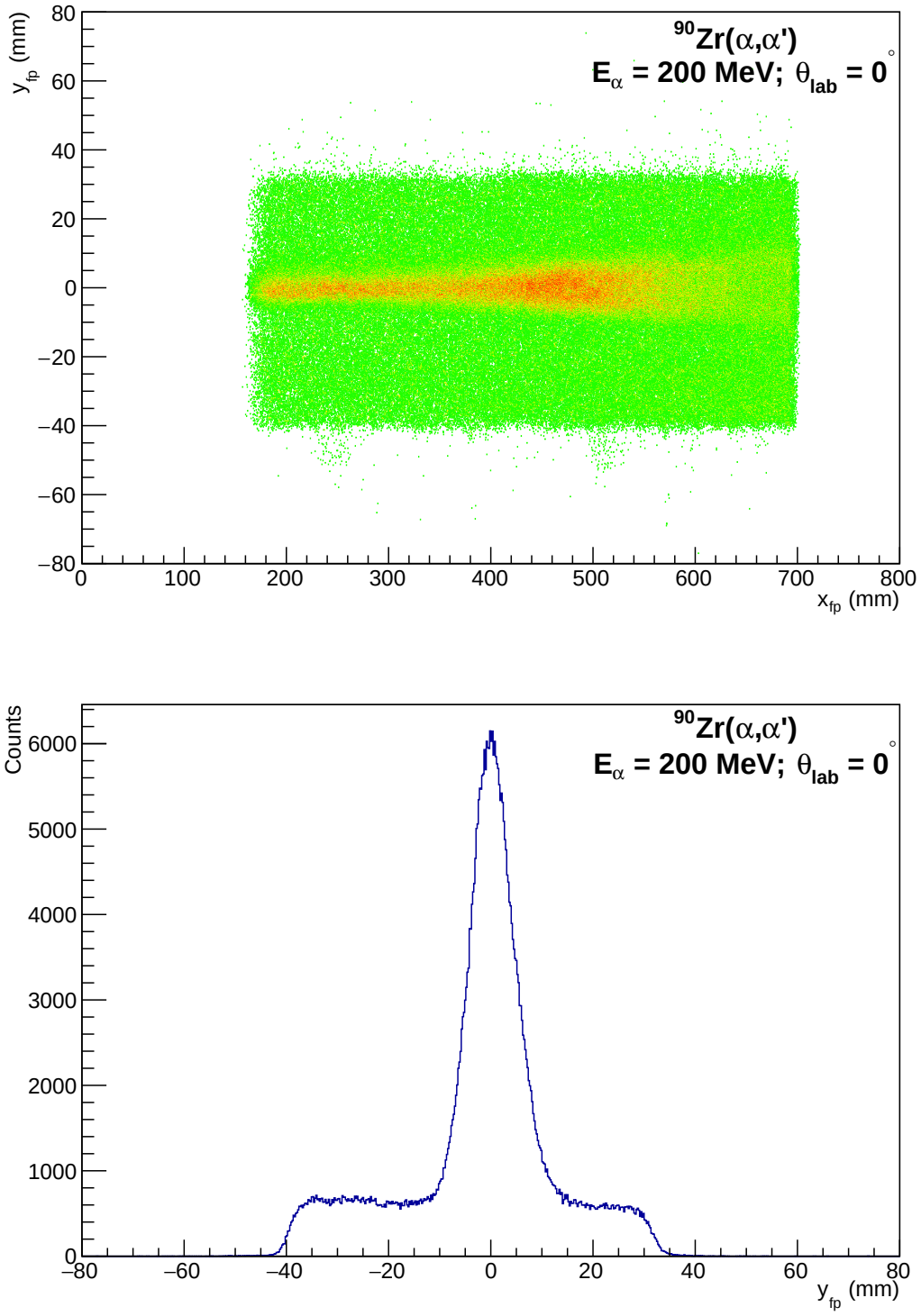

Figure 3.17: *Upper*: The two-dimensional x_{fp} (mm) *versus* y_{fp} (mm) scatterplot for ^{90}Zr. *Lower*: The y_{fp} projection of the focal-plane events show events of interest centered around $y_{\mathrm{fp}} = 0$.

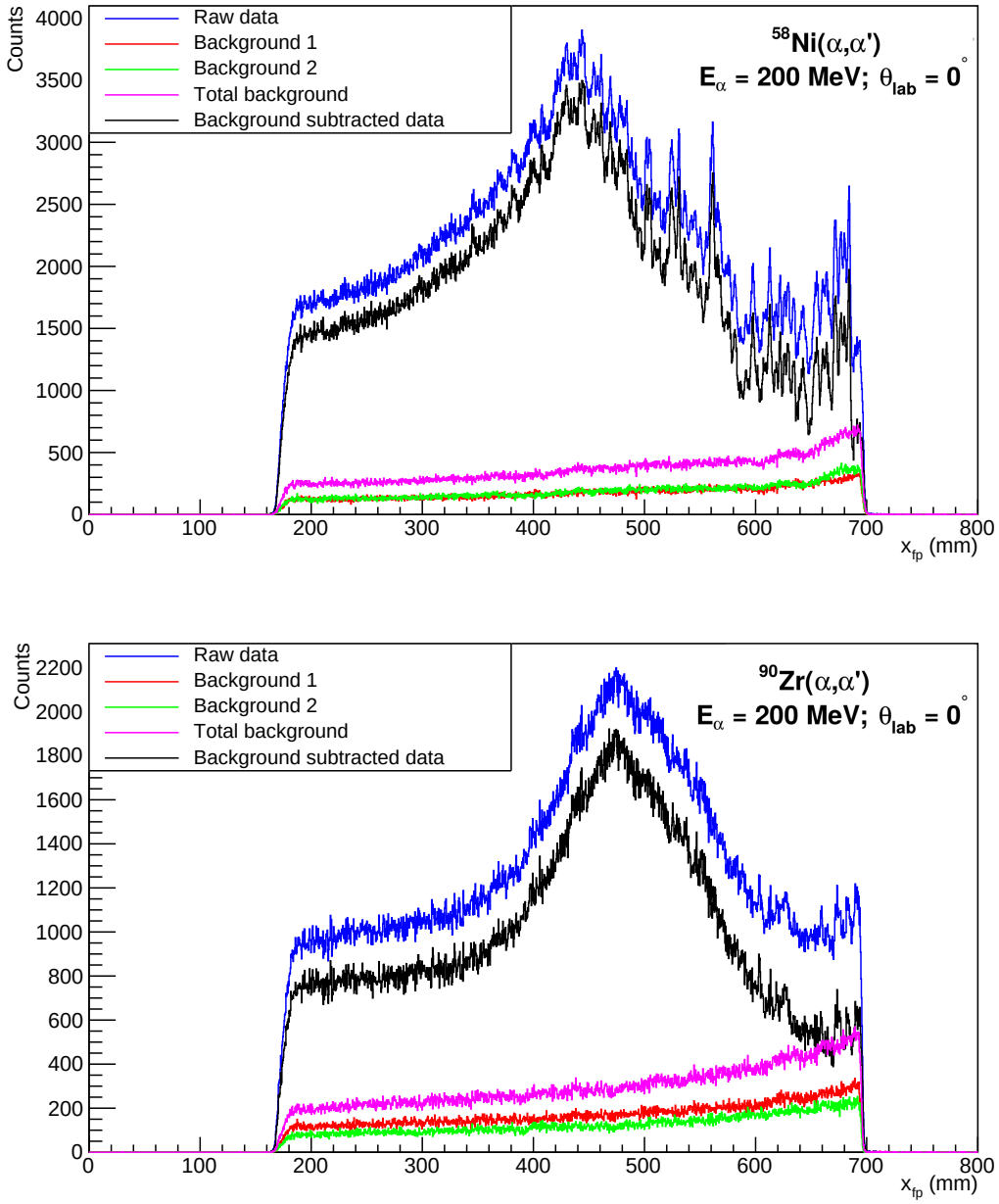

Figure 3.18: The focal-plane position spectra showing the components involved in the background-subtraction procedure. *Upper*: ^{58}Ni. *Lower*: ^{90}Zr

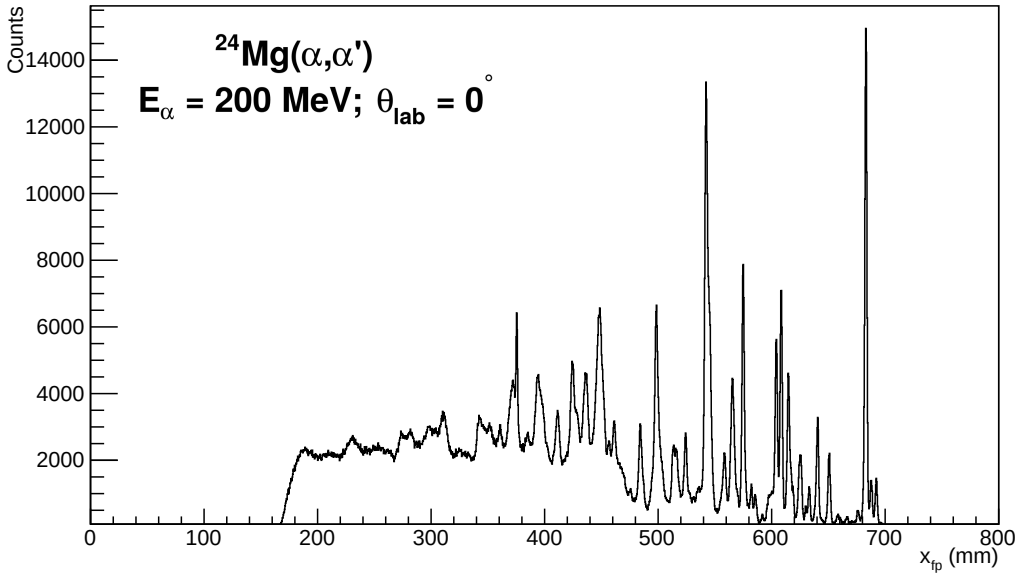

Figure 3.19: The background-subtracted focal-plane position spectrum for ^{24}Mg after the application of the lineshape correction

3.7.3 Data offsets

Shifts in the focal-plane positions and the primary TOF peaks of the detected particles occur owing to field drifts. Field drifts result from a change in temperature and Radio Frequency (RF) field changes owing to the operators performing optimisations during beam time, which may slightly affect the beam energy. During the acceleration process, the particles pass through the SSC many times and are, therefore, affected by any modifications in the beam setup.

All relevant data files for a particular nucleus must be chained together. Shifts in the focal-plane position compromise the energy-resolution, while TOF shifts compromise the location of the PID gates. Before the data files are chained together, the shifts must be taken into account. Each data file was then assigned a focal-plane position offset and a TOF-peak offset relative to a chosen reference point. Figure 3.20 shows the focal-plane position spectrum with no

offsets. Figure 3.21 shows the effect of both offsets on the focal-plane position spectrum. It must be noted that the energy-resolution was approximately 86 keV FWHM which was substantially reduced (see Section 3.7.4). It is important to note that although only the calibration-target spectrum is shown for illustrative purposes, this procedure was performed for all nuclei of interest.

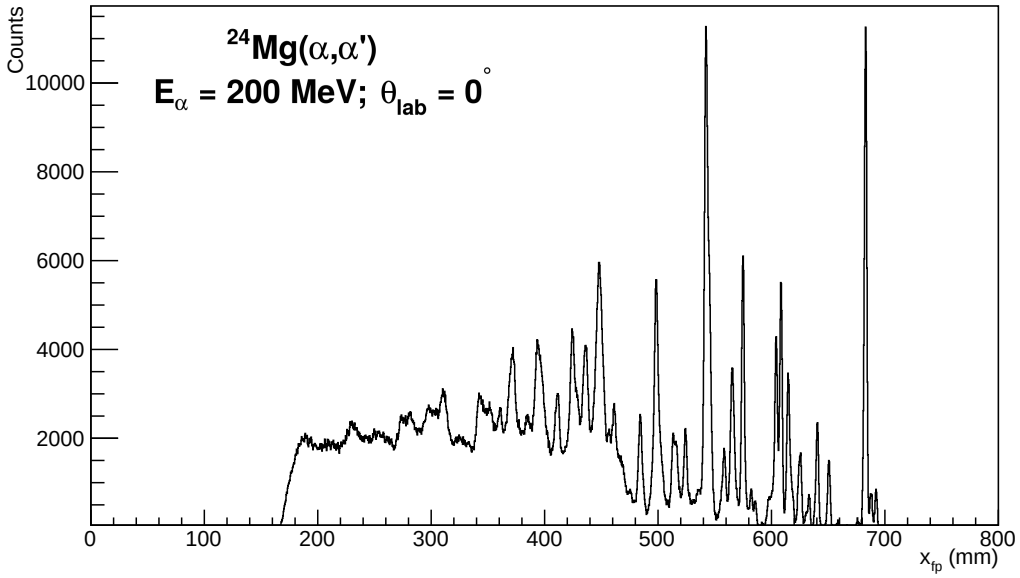

Figure 3.20: The focal-plane position spectrum without position and TOF offsets for ^{24}Mg.

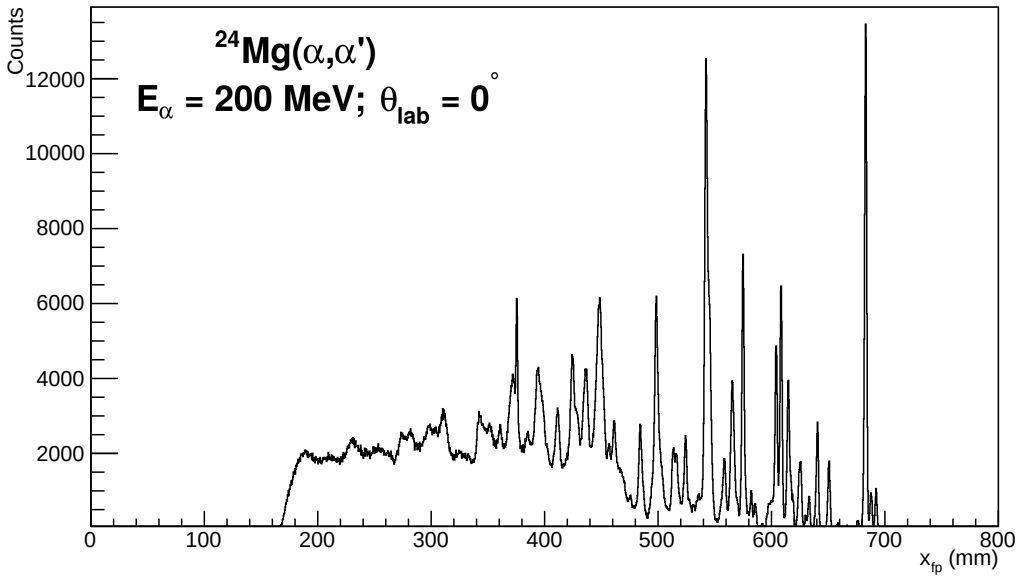

Figure 3.21: The focal-plane position spectrum with both position and TOF offsets for ^{24}Mg.

3.7.4 Energy resolution

Each nucleus was associated with a ^{24}Mg calibration target so as to achieve the most-accurate position-to-energy calibration (discussed in Section 3.7.5). Following the above data-extraction and optimisation procedures, it was possible to calculate the energy resolution from the position resolution of the calibration chain. A Gaussian-plus-polynomial fit was applied to the most-prominent peak in the focal-plane position spectrum of ^{24}Mg, as is shown in Fig. 3.22. A sigma value (mm) was obtained from this fit. Using a factor of 33 keV/mm (calculated during online and offline calibrations), the energy resolution could be calculated and is shown in Table 3.2.

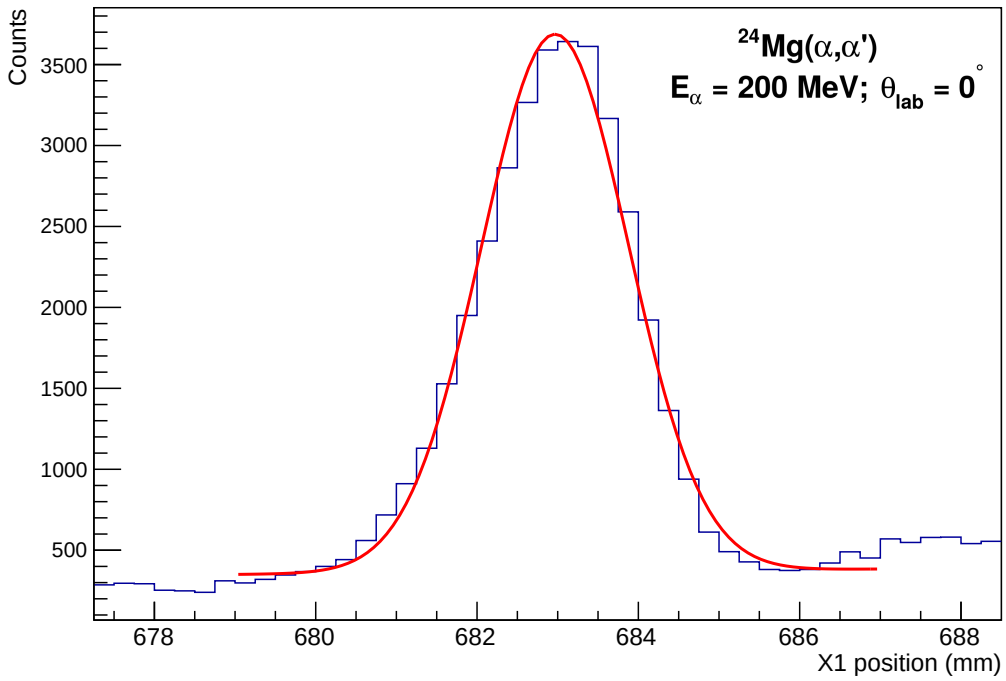

Figure 3.22: An example of a Gaussian-plus-polynomial fit of the most-prominent peak in calibration target ^{24}Mg.

Table 3.2: Position and energy resolutions for the isotopes associated with the ^{24}Mg calibration target

Calibration Target	Association	σ_{pos} (mm)	E_{res} (keV)
^{24}Mg	^{58}Ni	0.903	70
^{24}Mg	^{90}Zr	0.903	70

3.7.5 Energy calibration

The excitation-energy calibration process is two-part and consists of a position-to-rigidity calibration followed by a rigidity-to-energy calibration. Rigidity is determined by the effect of a particular magnetic field on the trajectory of a charged particle. Essentially, it is a measure of the momentum of the particle [73].

3.7.5.1 Position-to-rigidity calibration

Once the lineshape-correction, background-subtraction and data-offset procedures were performed, the focal-plane position spectra were primed for the energy calibration. The first step involved was to identify predicted excited states in the position spectrum. Identified focal-plane positions were then paired with the corresponding known values for the excitation energies of those states. Known energies of the particles of interest of the identified states were used to calculate the rigidity values using a relativistic kinematics code. The calculated rigidity values were plotted against the corresponding focal-plane positions, to which a second-order polynomial fit was applied. The calibration parameters are the coefficients of the equation of best fit and can be seen in Fig. 3.23.

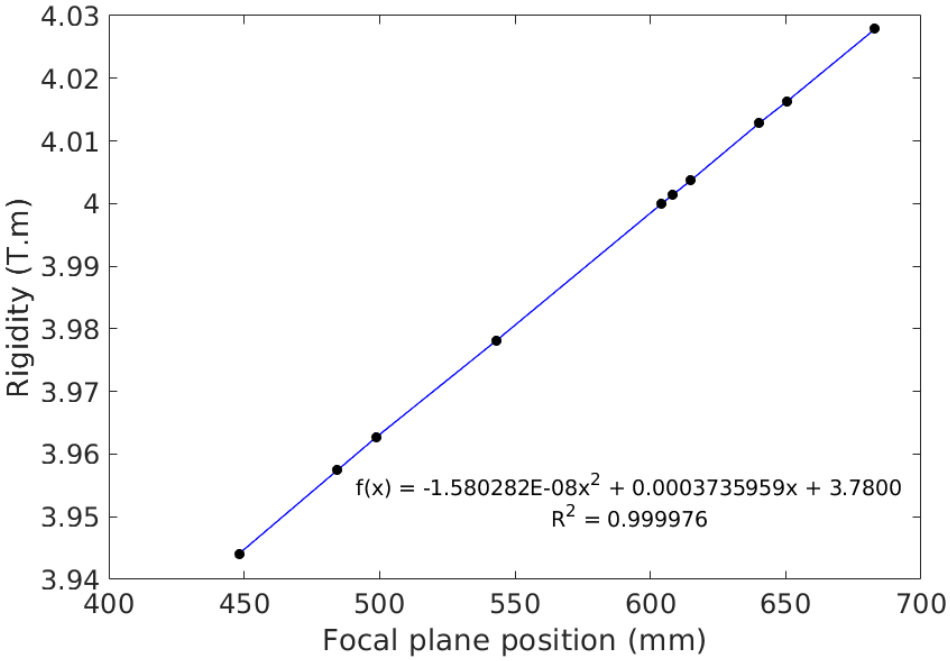

Figure 3.23: The rigidity calibration curve.

3.7.5.2 Rigidity-to-energy calibration

Once the rigidity calibration was done, a simple momentum-to-excitation-energy calibration was then performed. The rigidity values were converted to momentum values within the K600 offline analyser. The excitation energy is derived from two-body kinematics and is given by [3, 74]:

$$E_{\mathrm{x}} = E_0 + m_1 + \sqrt{{p_2}^2 - m_2^2} - ({p_0}^2 + {p_2}^2 - 2p_0p_2cos(\theta) + {m_3}^2)^{\frac{1}{2}}, \qquad (3.10)$$

where the subscripts 0, 1, 2 and 3 represent the projectile, target, ejectile, and recoil nuclei, respectively. Equation (3.10) has components that were calculated for the calibration isotope as well as for ^{58}Ni and ^{90}Zr. The conversion to excitation energy was performed for all nuclei of interest.

3.7.5.3 Excitation-energy spectra

The calibrated excitation-energy spectrum is shown in Fig. 3.24 (upper). An enlarged region between 8 - 18 MeV shows the identified states (lower). Table 3.3 includes a list of the identified values compared with those documented in literature as well as the difference in MeV. Table 3.3 also indicates the reference states that were chosen for calibration purposes. The well-documented states were obtained from the National Nuclear Data Center (NNDC) [75], Kawabata [76] and Kawabata et al. [77].

Table 3.3: A comparison of the energy values obtained in this work and those that are well documented for ^{24}Mg.

J^{π}	Documented states (MeV)	Present work (MeV)	Difference (keV)
0^+, 2^+	9.305	reference state	
2^+	10.360	10.354	5.90
0^+	10.68	10.69	10.18
0^+	11.278	reference state	
2^+	11.5182	11.5122	5.98
1^-	11.864	11.867	3.93
0^+	13.85	13.848	1.96
0^+	15.25	reference state	
	15.72	15.753	33.00
	16.92	16.930	10.95

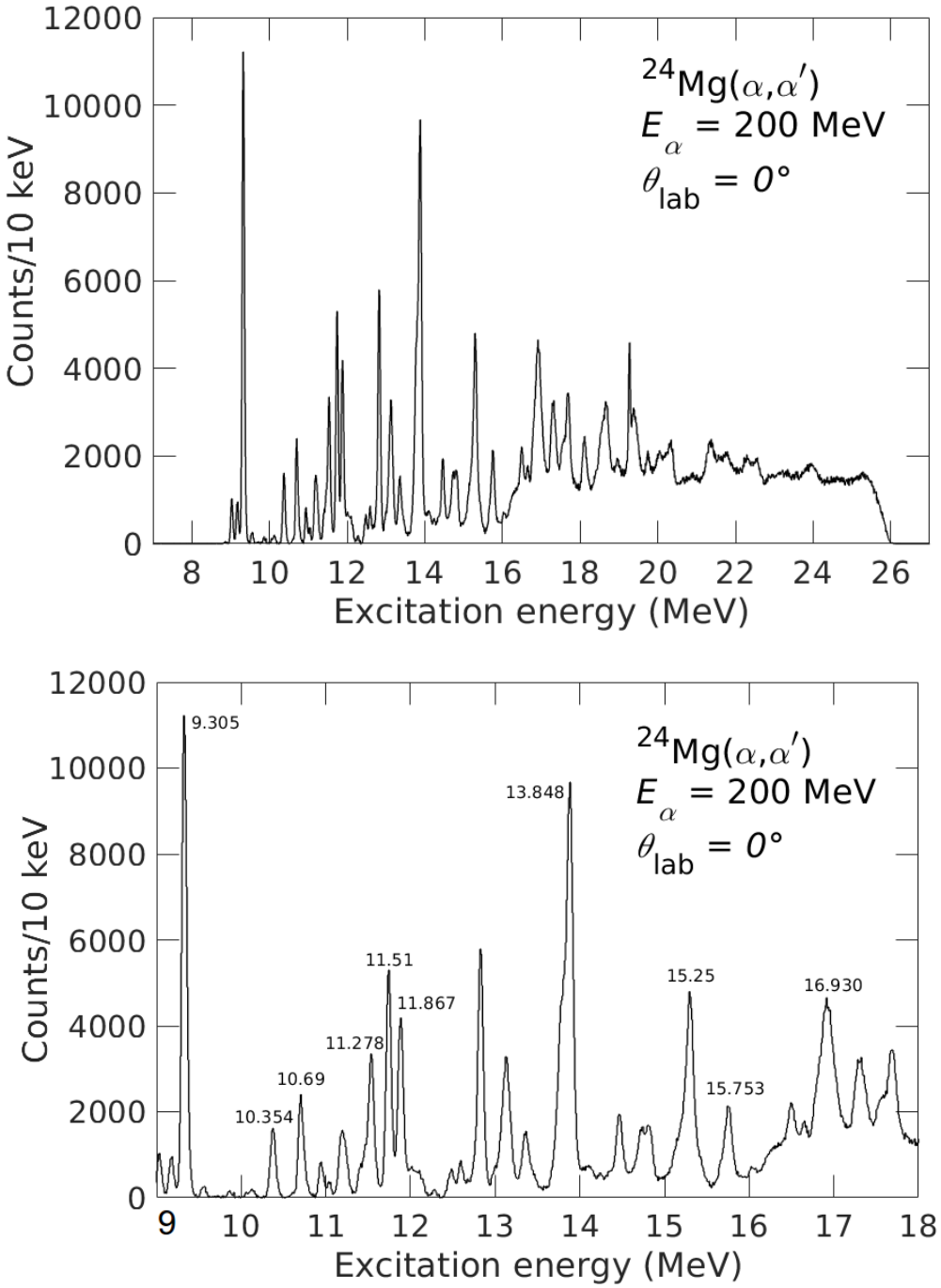

Figure 3.24: The calibrated excitation-energy spectrum for ^{24}Mg (*upper*); A magnification of the identified states (*lower*).

3.7.6 Double-differential cross sections

The experimental double-differential cross section for the α-particle inelastic scattering reaction (units of mb sr^{-1}) is given by:

$$\frac{d^2\sigma}{d\Omega} = \frac{10^{27} \cdot N_{\rm c}}{N_0 \cdot \rho \cdot D \cdot \Delta\Omega \cdot \Delta E \cdot \epsilon_{\rm tot}} \tag{3.11}$$

$N_{\rm c}$ is the corrected number of counts in a bin,

N_0 is the total number of incident α particles on the target,

ρ is the number of target nuclei per unit of area,

D is the electronic dead time correction factor,

$\Delta\Omega$ is the solid angle of the K600 magnetic spectrometer in sr and has a value of 3.41 sr,

ΔE is the energy bin size (MeV) and

$\epsilon_{\rm tot}$ is the total MWDC efficiency of the K600 magnetic spectrometer, and depends on which wire planes were used for the angle calibration.

$$N_0 = \frac{CI \cdot R \cdot 10^{-12}}{e} \tag{3.12}$$

CI is the scalar read-out of the current integrator,

R is the selected range (in nA) of the current integrator and

e is the proton electric charge (in Coulombs).

$$\rho = \frac{\lambda \cdot N_{\rm A}}{A}. \tag{3.13}$$

λ is the target thickness,

N_{A} is Avogadro's number and

A is the mass number of the nucleus in question.

For this experiment, the MWDC efficiency is calculated as follows:

$$\epsilon_{\mathrm{tot}} = \epsilon_{\mathrm{X1}} \times \epsilon_{\mathrm{U1}} \times \epsilon_{\mathrm{U2}}. \tag{3.14}$$

Using the above equations, the double-differential cross sections were extracted for ^{58}Ni and ^{90}Zr.

Chapter 4

Analysis of results and discussion

Excitation-energy spectra, a result of the data-extraction process detailed in Chapter 3, are presented. Results of the DWBA inelastic-scattering calculations are also presented. These calculations were used to determine the most appropriate scattering angle for the ISGMR measurements. DWBA calculations are also used to determine the best-possible angle for a background subtraction of other multipolarity contributions. A Discrete Wavelet Transform (DWT) background-subtraction technique was performed and is presented in comparison to a Difference of Spectra technique to demonstrate its validity as a multipole background subtraction process. Following this, the centroid energy and width of the resonance for the nuclei under investigation were extracted. In addition, the characteristic energy scales, which were extracted with the use of the Continuous Wavelet Transform (CWT) technique, are presented and discussed. For the sake of continuity, figures are placed at the end of each section.

4.1 Experimental data

The experimental data were obtained through bombarding the chosen nuclei with 200 MeV α particles over a series of three weekends. These data underwent intensive offline extraction and optimisation processes, as detailed in Chapter 3. Elastic-scattering peaks were excluded by operating the K600 magnetic spectrometer in a field setting chosen solely for the exclusion of this peak. Given that the elastic-scattering cross sections are extremely high at and close to zero degrees, the data acquisition count rate would be dominated by the elastic-scattering peak for this fieldset. The chosen mode, therefore, excludes not only the elastic-scattering peak but also the low-lying excited states in the nuclei that were investigated. This process enhanced the statistics for the ISGMR region at the highest-possible beam current. The experimental energy resolution for all spectra is approximately 70 keV FWHM.

Figure 4.1 shows the excitation-energy spectra for ^{24}Mg (upper), ^{58}Ni (middle), and ^{90}Zr (lower) *versus* counts/10 keV after the subtraction of the instrumental background. The spectra were then converted into double-differential cross sections through the application of the double-differential cross-section equation (Eq. (3.11)), the result of which is shown in Fig. 4.2.

As mentioned in Section 2.3.1, the ISGMR exhibits an apparent disappearance which is a characteristic feature in lighter nuclei [19]. This is not a disappearance but rather a severe spreading and breaking up of the resonance, which can be identified for ^{24}Mg in the upper panels of Figs. 4.1 and 4.2. This spreading allows for an easy identification of distinct excited states, which can be seen in the lower panel of Fig. 3.24. The ^{24}Mg target was used as a calibration target owing to the presence of distinct excited states, as shown in Chapter 3. Since ^{58}Ni is considered a light nucleus and, as such, the structure towards the left of the centroid shows some fragmentation. The ISGMR for ^{90}Zr can be seen as a wider peak with fine structure on either side owing to the spreading of

the resonance.

Again, in Section 2.3, it was also mentioned that as the mass number increases the width of the ISGMR decreases and the centroid moves towards the lower energy range. This is evident for ^{58}Ni and ^{90}Zr in the middle and lower panels, respectively, of Fig. 4.2.

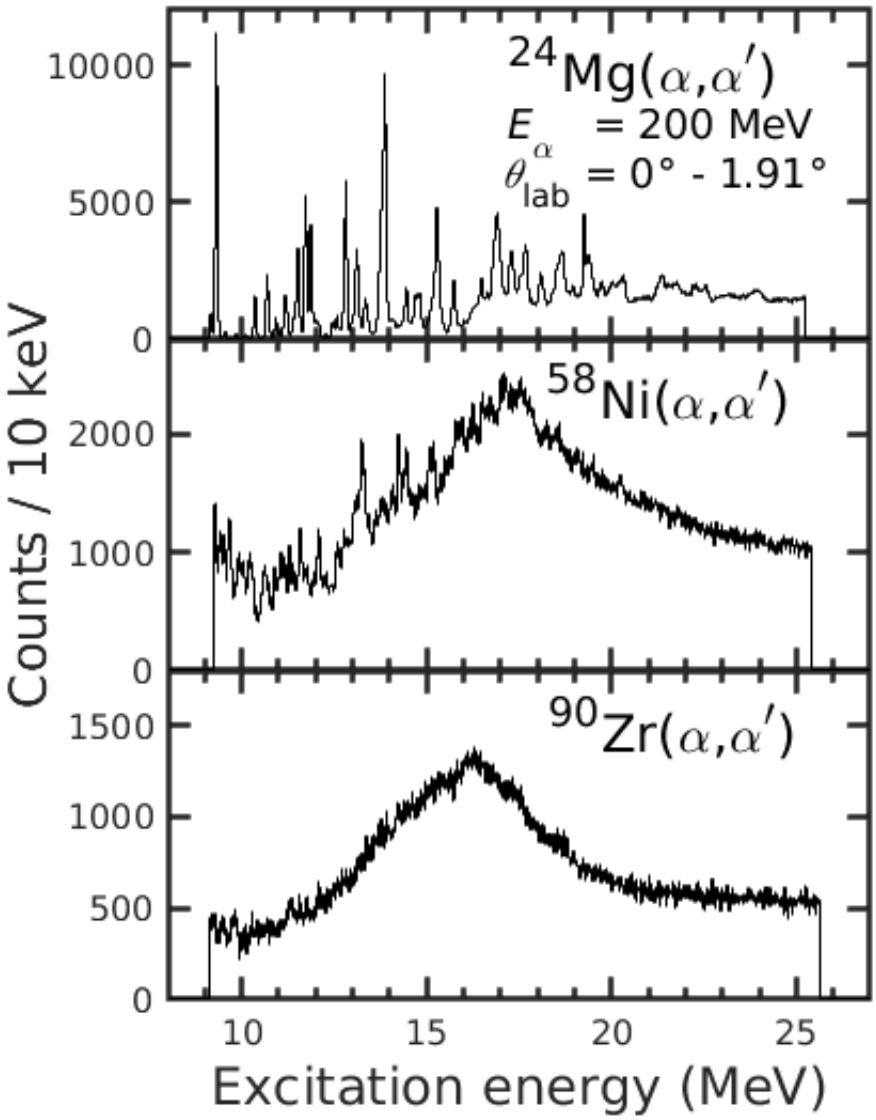

Figure 4.1: Excitation-energy spectra for α-particle inelastic scattering at $E_\alpha = 200$ MeV for ^{24}Mg (*upper*), ^{58}Ni (*middle*), and ^{90}Zr (*lower*). Measurements were taken at $\theta_{\rm lab} = 0°$ where the cross section of the ISGMR is at a maximum.

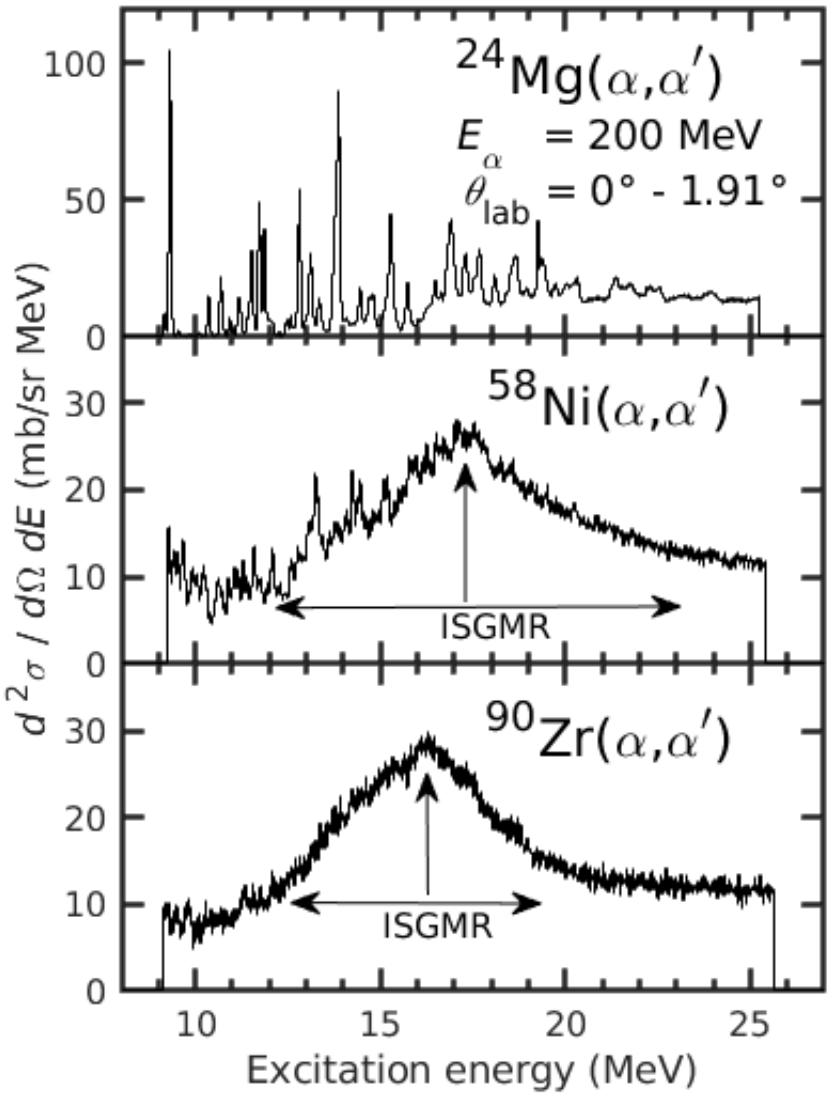

Figure 4.2: Excitation energy (MeV) *versus* double-differential cross section (mb/sr MeV) for α-particle inelastic scattering at $E_\alpha = 200$ MeV for ^{24}Mg (*upper*), ^{58}Ni (*middle*), and ^{90}Zr (*lower*).

4.2 Isoscalar Giant Monopole Resonance in ^{90}Zr

4.2.1 ^{90}Zr ISGMR distribution

The excitation of the ISGMR is strongly scattering-angle dependent especially when it is excited by the inelastic scattering of α particles at intermediate energies. In the early work of 2004 by Uchida et al. [78] at the cyclotron of the Research Center for Nuclear Physics (RCNP), Osaka, angular distributions were obtained for (α, α') at $E_\alpha = 386$ MeV in the range $0^\circ < \theta_{\rm lab} < 13.5^\circ$ and $8 \leq E_{\rm x} \leq 32$ MeV using the Grand Raiden spectrometer for ^{90}Zr, ^{116}Sn, and ^{208}Pb. A Multipole Decomposition Analysis (see Ref. [79]) allowed $L = 0$ (ISGMR) and $L = 1$ (ISGDR) strength distributions to be extracted. In particular for ^{90}Zr, the ISGMR was located at 16.6 ± 0.1 MeV with a width of $\Gamma = 4.9 \pm 0.2$ MeV exhausting 101 ± 3 % of the EWSR. In addition, significant $E0$ strength was found above the ISGMR extending up to 32 MeV, the limit of the experimental measurement.

Later, in 2016, Gupta et al. [10] measured (also at RCNP) the mass 90 nuclei ^{90}Zr, ^{92}Zr, and ^{90}Mo using (α, α') at $E_\alpha = 358$ MeV at extremely forward scattering angles including 0°. This was prompted by the then-recent work of the Texas A & M group (see Refs. [11-13] of Gupta et al. [10]) investigating the ISGMR in the A $\sim$ 90 region claiming that the ISGMR strength distributions vary dramatically, thus indicating that nuclear incompressibility is very strongly influenced by nuclear-structure effects. However, using the Difference of Spectra (DOS) technique (Ref. [22] of Gupta et al. [10]) whereby the measured spectrum at first minimum of the ISGMR angular distribution is taken away from that measured at 0° (the maximum of the ISGMR) yields the pure ISGMR, free from the reasonably flat distributions of the other multipoles excited in that scattering-angle region.

4.2.2 Multipole decomposition and DOS method

The DOS method relies on knowing the angular region to be subtracted for the (α, α') measurement. This is determined by calculating angular distributions within the DWBA for the low-order multipoles excited above $L = 0$. Figure 3 of Gupta et al. [10], reproduced here as Fig. 1.2, shows the results of such calculations and the subsequent fit to the measured ^{90}Zr(α, α') at an excitation energy of 16 MeV in ^{90}Zr, maximum of the ISGMR. Here, it can be seen that the DOS method requires the spectrum measured at $\theta_{\text{c.m.}} = 2^\circ$ to be subtracted from that measured at 0°. The results of which are given in the lower panel of Fig. 2 of Gupta et al. [10], reproduced here as Fig. 1.3.

As a starting point for the calculation of α-particle inelastic scattering, a reliable optical model potential is required. Gupta et al. [10] used the density-dependent single-folding model with a Gaussian α-nucleon potential for the real part and a Woods-Saxon imaginary term (details of which can be found in Ref. [10]). This required the simultaneous fitting of elastic scattering and inelastic scattering to low-lying discrete states in the target nucleus via (α, α') scattering.

For the present project, in the absence of extensive elastic- and inelastic-scattering data for α-particle scattering, a global α-nucleus optical model potential was used (determined by Kumar and Kailas [80]). The values calculated using the code OM-Alpha [81, 82] are given in Table 4.1 and are used for the real and imaginary volume potentials described in Section 2.7. Derivative Woods-Saxon collective form-factors were used for multipolarities $L = 0$ to $L = 6$. The results for ^{90}Zr(α, α') at $E_\alpha = 385$ MeV are shown in the upper panel of Fig. 4.3 after adjusting the respective EWSR fractions (see Eq. (1.1)) to fit the measured scattering data of Gupta et al. [10]. Here, it can be seen that there is excellent correspondence with Fig. 3 of Gupta et al. [10] reproduced as Fig. 1.3. The same EWSR fractions were then used to calculate ^{90}Zr(α, α') at $E_\alpha = 200$ MeV, the results of which are shown in the lower panel of Fig.

4.3.

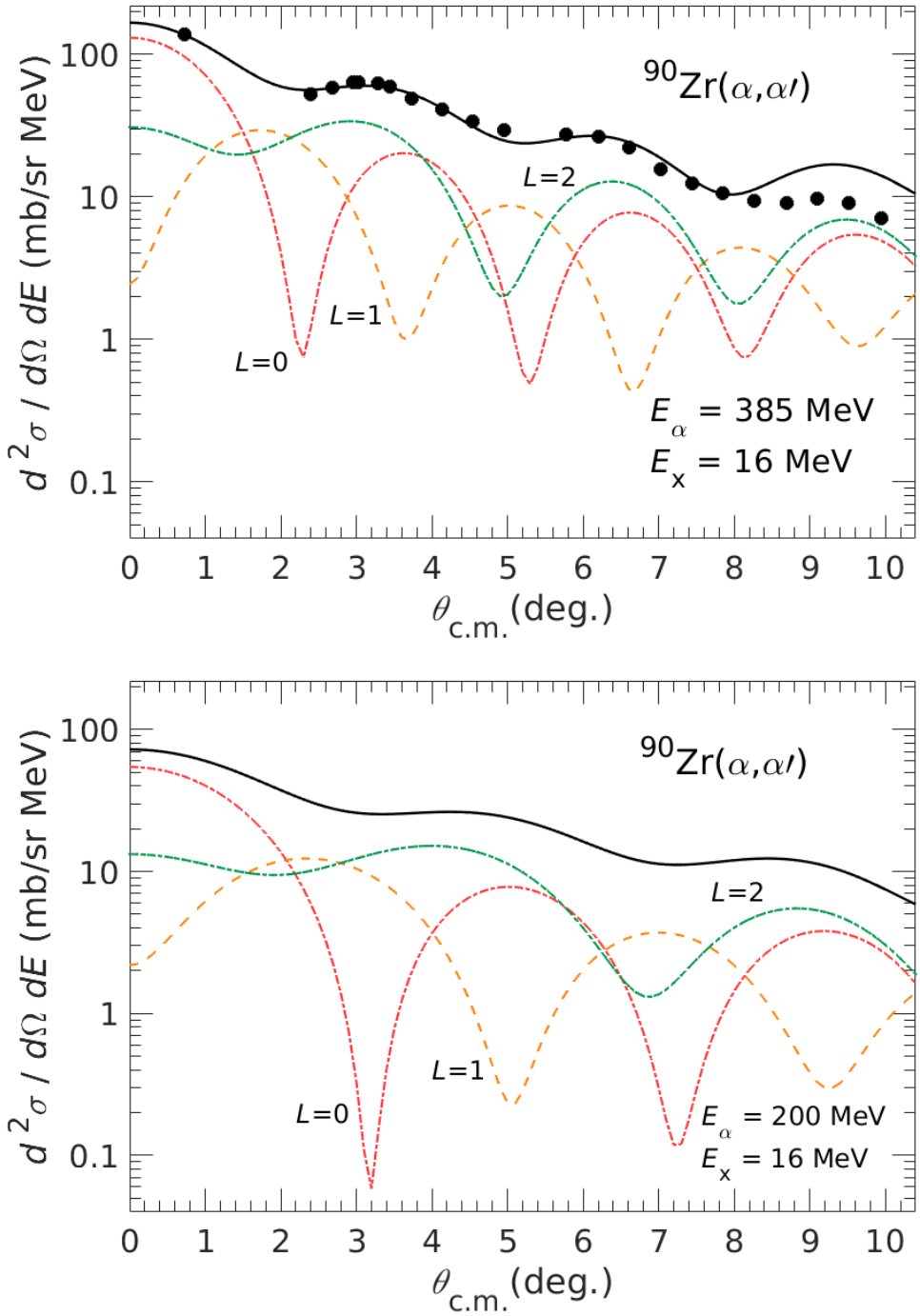

Figure 4.3: Multipole Decomposition Analysis: angular distributions for DWBA α-particle inelastic scattering on ^{90}Zr(α, α'). *Upper*: E_α = 385 MeV. *Lower*: E_α = 200 MeV.

Table 4.1: Optical model potential parameters for ^{90}Zr(α, α') calculated using the method of Kumar and Kailas [80] using the code OM-Alpha [81]. The parameters refer to the real and imaginary Woods-Saxon volume potentials presented in Section 2.7.

$E_{\rm lab}$ (MeV)	$V_{\rm R}$ (MeV)	$r_{0\rm R}$ (fm)	$a_{\rm R}$ (fm)	$V_{\rm I}$ (MeV)	$r_{0\rm I}$ (fm)	$a_{\rm I}$ (fm)
200	112.63	1.235	0.760	20.088	1.555	0.600
385	103.96	1.235	0.760	20.060	1.555	0.600

4.2.3 ISGMR ^{90}Zr background subtraction, DOS and DWT

As can be seen in the upper panel of Fig. 4.3, by subtracting the measured spectrum at 2°, where the $E0$ contribution is a minimum and yield from other multipoles is fairly flat, from the measured spectrum at $\theta_{\rm avg} = 0.7°$, a difference spectrum is almost entirely composed of monopole strength. The difference spectrum is shown in the lower panel of Fig. 2 of Gupta et al. [10], reproduced here as Fig. 1.3. The challenge now is to investigate the similarity of the DWT for background subtraction.

Figure 4.4 illustrates the excitation-energy spectrum of ^{90}Zr(α, α') at $E_\alpha = 385$ MeV obtained from NNDC [83], and published by Ref. [10]. The spectrum was restricted to the 10 - 25 MeV excitation-energy range. This restriction is consistent with the focal-plane excitation-energy range of the K600 magnetic spectrometer that was used in this experiment.

An instrumental background-subtraction procedure, through software corrections, was presented in Chapter 3. It is assumed that for Fig. 4.4, a similar instrumental background subtraction has already been performed. The DWT background-subtraction method accounts for contributions from other

multipolarities by decomposing the spectrum into several approximations and details (see Section 2.9.4). These decompositions can be approximated with low-order polynomials [58]. The approximations and details for Fig. 4.4 (after limiting the spectrum between 10 - 25 MeV as in Fig. 4.5) can be seen in Fig. 4.6. The Biorthogonal 6.8 symmetrical wavelet family was chosen in this investigation owing to the amount of suitable vanishing moments [58]. In order to subtract the non-resonant background component, A_7 was chosen and adjusted downwards to just below the low and high excitation-energies of the ISGMR. This was then subtracted from the excitation-energy spectrum. The components of this procedure are shown in Fig. 4.5.

Excellent correspondence can be seen between the experimental DWT background-subtracted spectrum in Fig. 4.5 and that of the blue spectrum in the lower panel of Fig. 1.3. It is, therefore, possible to employ the use of the DWT background-subtraction technique as a reliable alternative to the DOS technique. The DWT background-subtraction technique was then used on ^{90}Zr at $E_\alpha = 200$ MeV. The components of this subtraction can be seen in Fig. 4.7, while the approximations and details are shown in Fig. 4.8. The Biorthogonal 6.8 symmetrical wavelet family was once again used. For ^{90}Zr at $E_\alpha = 200$ MeV, it was necessary to subtract the non-resonant component at A_{10}. This component was then subtracted from the original excitation-energy spectrum, the components of which can be seen in Fig. 4.7.

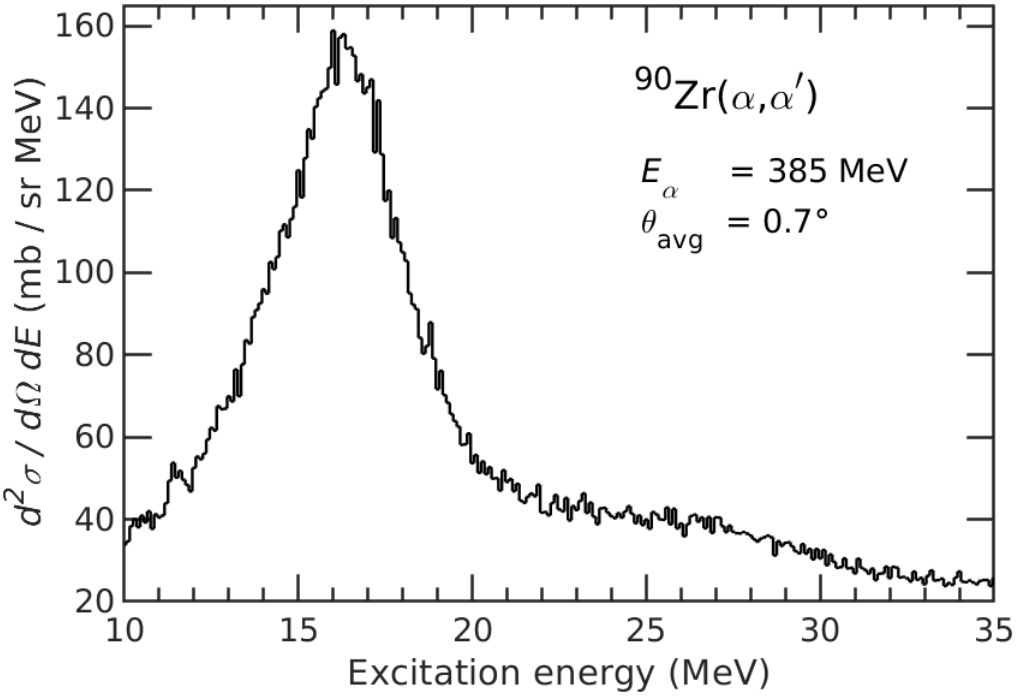

Figure 4.4: Excitation-energy spectrum of ^{90}Zr(α, α') at $E_\alpha = 385$ MeV. See upper panel of Fig. 1.3 (data obtained from the NNDC [83]).

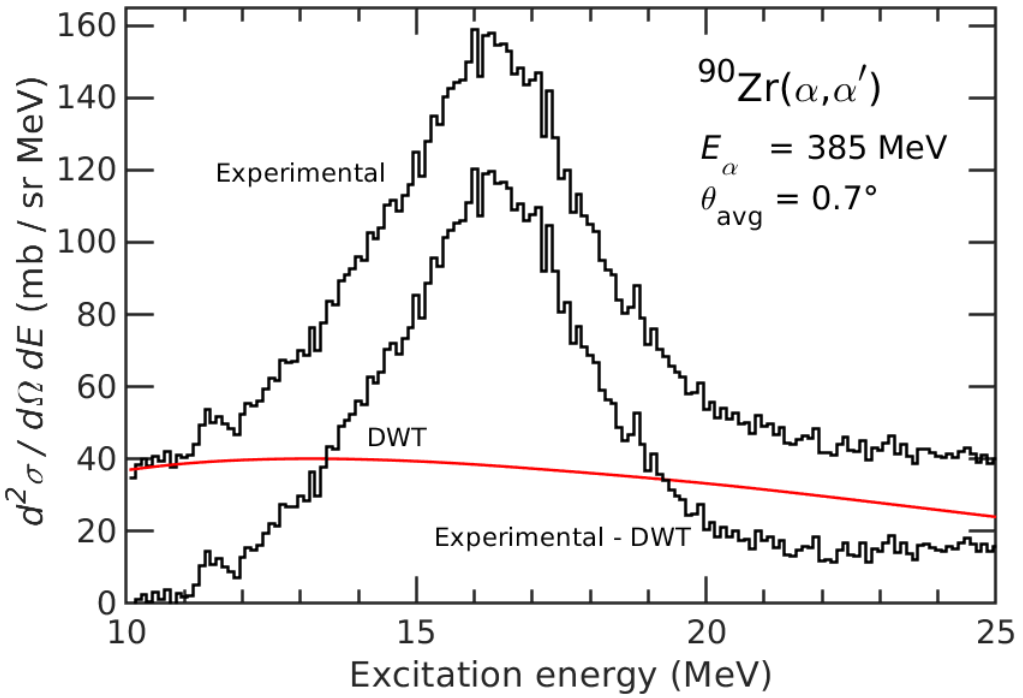

Figure 4.5: DWT background subtraction of the non-resonant component for the $^{90}\mathrm{Zr}(\alpha, \alpha')$ at $E_\alpha = 385$ MeV excitation-energy spectrum. *Upper*: Spectrum containing background components taken from [83] and then limited to the 10-25 MeV excitation-energy range. *Middle*: DWT background contribution. *Lower*: DWT background-subtracted excitation-energy spectrum.

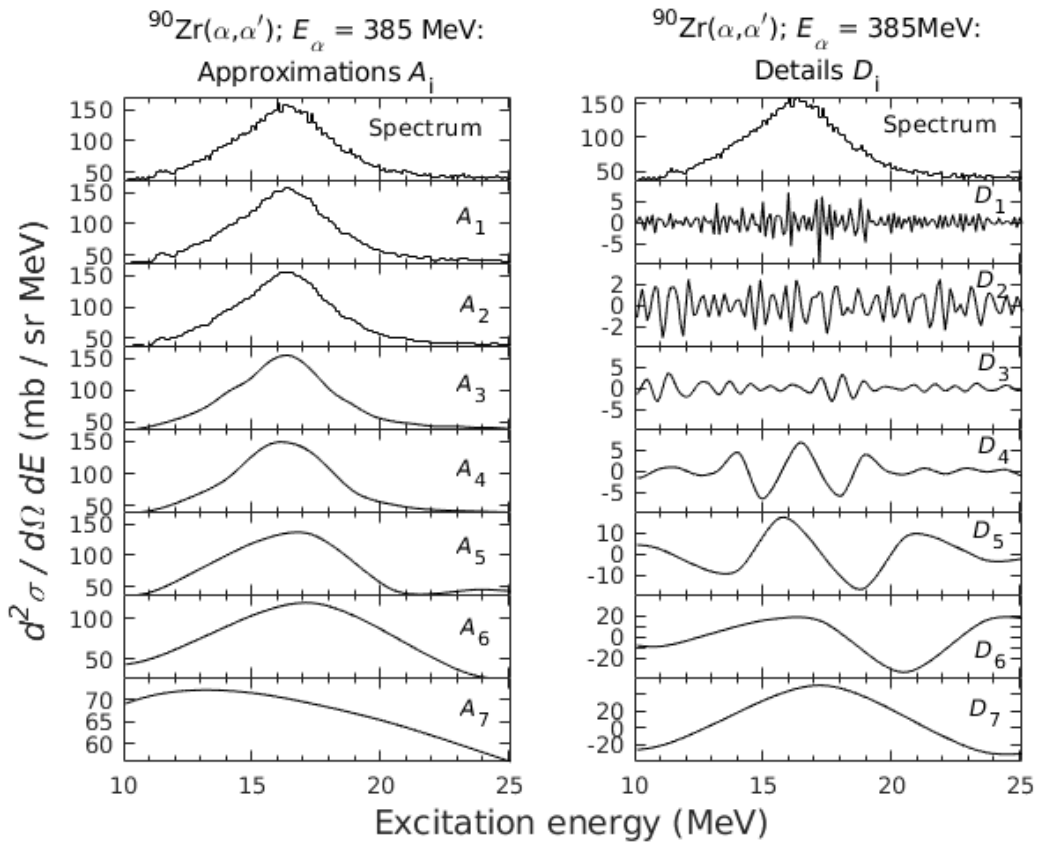

Figure 4.6: Decomposition of the ^{90}Zr(α, α') excitation-energy spectrum at $E_\alpha = 385$ MeV into approximations (A_i) and details (D_i), where i represents the integers from 1 to 7.

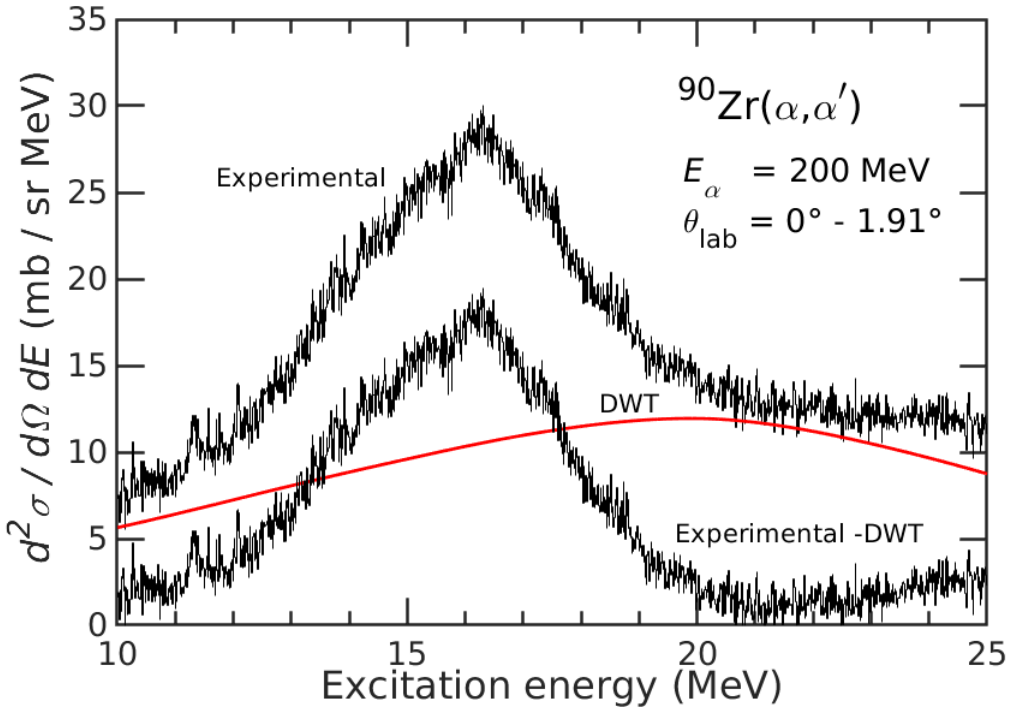

Figure 4.7: DWT background subtraction of the non-resonant component for the ^{90}Zr(α, α') at $E_\alpha = 200$ MeV excitation-energy spectrum. *Upper*: Spectrum containing background components. *Middle*: DWT background contribution. *Lower*: DWT background-subtracted excitation-energy spectrum.

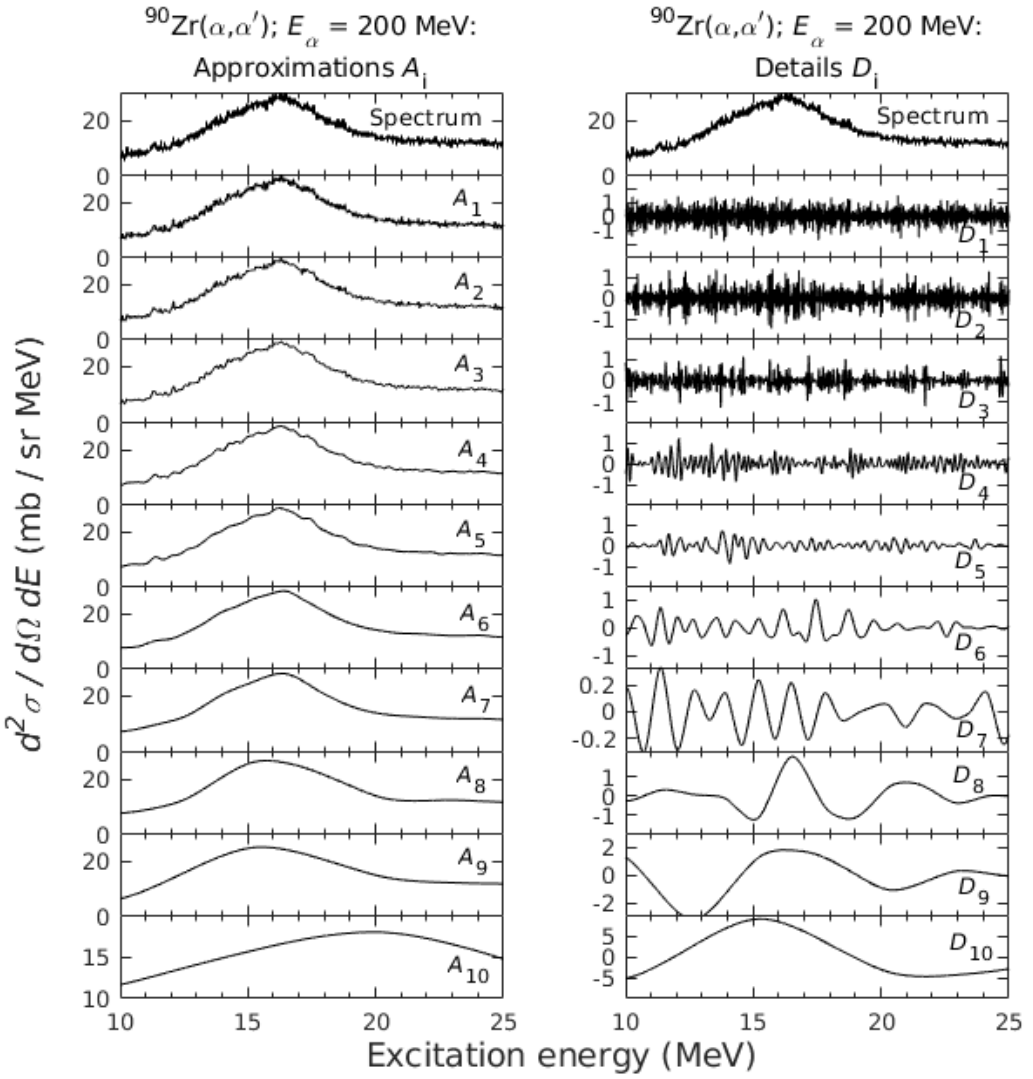

Figure 4.8: Decomposition of the ^{90}Zr(α, α') excitation energy spectrum at E_α = 200 MeV into approximations (A_i) and details (D_i), where i represents the integers from 1 to 10.

4.2.4 ISGMR width and centroid for ^{90}Zr

Following the DWT background-subtraction technique, the centroid energy and width of the ISGMR for the nuclei under investigation were extracted via the use of a Lorentzian fitting function (using Eq. (2.2)) in the software programme SciDAVis [84]. In order to achieve this, a Lorentzian curve-fitting procedure was applied to the ISGMR regions (between 10 and 25 MeV) of the background-subtracted data. This fit is illustrated in Fig. 4.9 for ^{90}Zr.

The application of a Lorentzian fit allowed for the extraction of the centroid energy and width for each target nuclei. The width of the ISGMR is denoted by Γ and is considered a parameter that characterises the decay mechanism of the resonance. Table 4.2 provides the centroids and widths obtained from similar studies conducted on ^{90}Zr as well as the result of the Lorentzian-fitting procedure for the present work.

Table 4.2: Experimentally extracted centroids and widths of the ISGMR for ^{90}Zr.

E_α (MeV)	Centroid (MeV)	Width (MeV)	Reference
200	15.90 ± 0.5	4.3 ±0.8	Present work
385	16.55	4.2	[10]
385	16.76	4.96	[85]
386	16.6	4.9	[78]

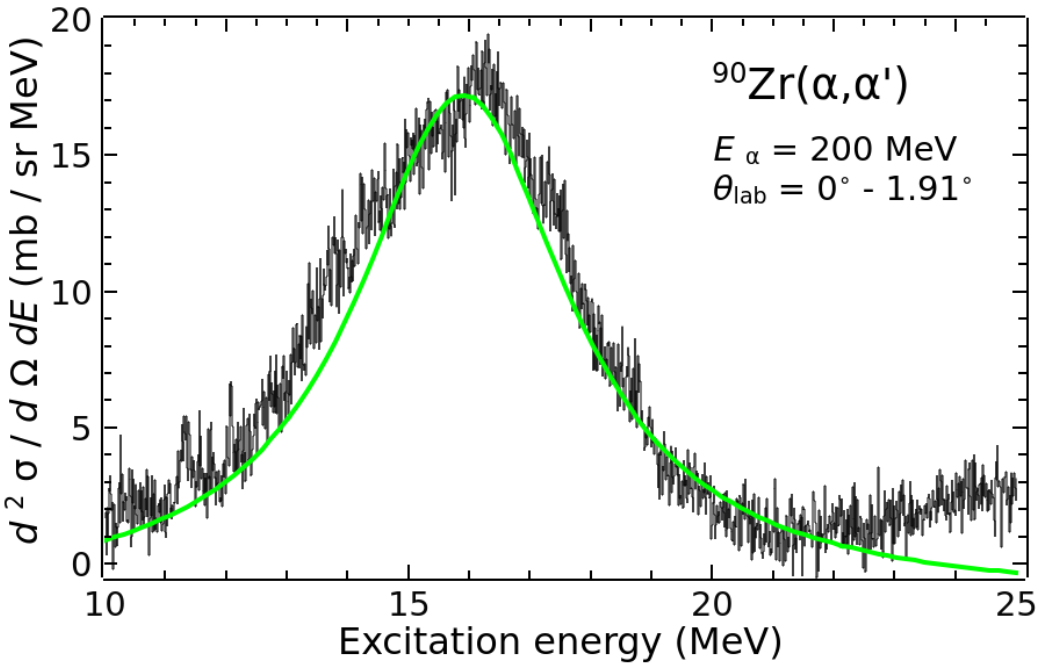

Figure 4.9: DWT background-subtracted excitation-energy spectra for ^{90}Zr showing the application of a Lorentzian curve fit (green).

4.2.5 ^{90}Zr ISGMR fine structure

Application of the CWT (detailed in Sections 2.9.1 and 2.9.2) gives a quantitative measure of observed fine structures. Thus, CWT analysis allows for characteristic energy scales from the excitation-energy region of the ISGMR to be extracted.

The Matlab software programme was used to perform the CWT analysis [86]. The complex-Morlet Mother wavelet was chosen for this project. The complex-Morlet Mother wavelet is preferred in fine-structure studies owing to its ability to provide the smallest time-bandwidth product [26, 87]. In the present project, extracted energy scales are directly comparable to the equivalent Fourier scale if the complex-Morlet Mother wavelet is used.

As a starting point, an overview is presented in Fig. 4.10 of the results obtained from QRPA and Phonon Phonon Coupling (PPC) calculations (described in Sections 2.6.2 and 2.6.3, respectively), the data of Gupta et al. [10] (lower panel of Fig. 4.10), and for comparison, the present ^{90}Zr($\alpha.\alpha'$) scattering data at $E_\alpha = 200$ MeV (upper panel of Fig. 4.10). Fundamental to those calculations within the Skyrme interaction is the choice of a set of Skyrme parameters. One of the Skyrme parameters is an incompressibility modulus K_∞. The calculated energy of the ISGMR is proportional to the nuclear incompressibility. Bearing this in mind, the results of the calculations within the f^- Skyrme force are shown. It should be noted that the SGII Skyrme force and the T45 Skyrme force were also tried but proved to be unsatisfactory regarding the $E0$ strength distributions produced. It can be seen in the lower panel of Fig. 4.10 that the dashed line of the QRPA (one-phonon) results produces $E0$ strength approximately 4 MeV above the position of the ISGMR. As such, in the following scales analysis, only the PPC results (using microscopic coupling matrix elements between the one- and two-phonon configurations) were used. The coupling between 1p-1h and 2p-2h excitations is very important for the description of the $E0$ strength distribution since it leads to a significant

fragmentation of ISGMR strength.

The CWT was applied to two separate regions of interest for ^{90}Zr, the main ISGMR region (12.5 - 19.5 MeV) and the higher-energy region (19.5 - 25 MeV) which exhibits $E0$ strength above the ISGMR. The characteristic scales were then extracted from each region. A summary of extracted scales is provided in Tables 4.3 and 4.4. The stronger scales are shown in bold.

In Section 2.6.3, the theory of PPC was described. The microscopic calculations of PPC are compared to the experimental excitation-energy spectrum for ^{90}Zr in the lower panels of Figs. 4.11 and 4.12. Good correspondence between the theoretical calculations and the experimental data can be seen. The centroid is almost reproduced with a shift to the higher-energy region, where the extracted scales show a good correspondence. Here, it should be noted that the theoretical spectra were folded using a Gaussian of 70 keV energy-resolution (FWHM) which was determined and presented in Chapter 3. It is important to note that individual states are experimentally best fitted with a Gaussian (as shown in Fig. 3.22). The overall shape of the resonance is Lorentzian. The weaker scales are shown with dotted arrows while the stronger scales are shown with continuous arrows in Figs. 4.11 and 4.12.

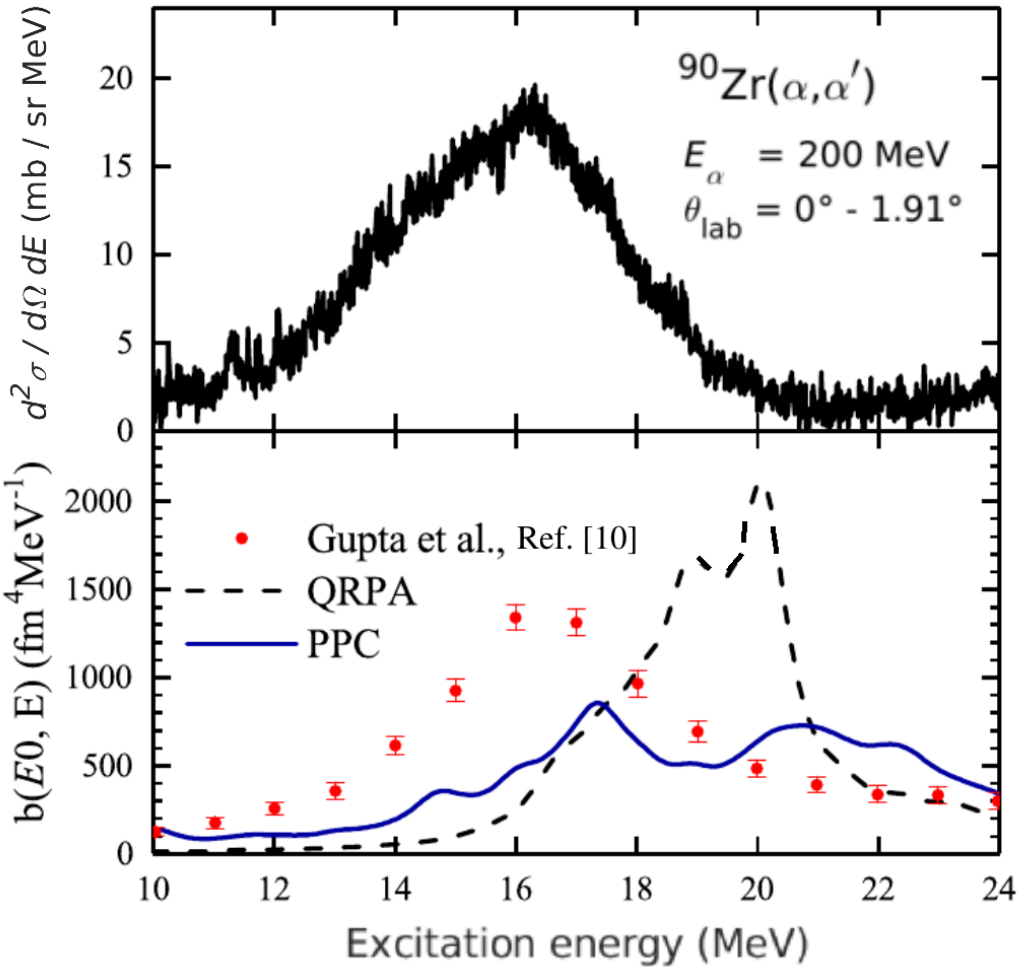

Figure 4.10: *Upper*: Experimental excitation-energy spectra for ^{90}Zr at E_α = 200 MeV. *Lower*: Solid line represents PPC strength distribution, filled circles represent data from Gupta et al. [10], dashed line represents the results of QRPA.

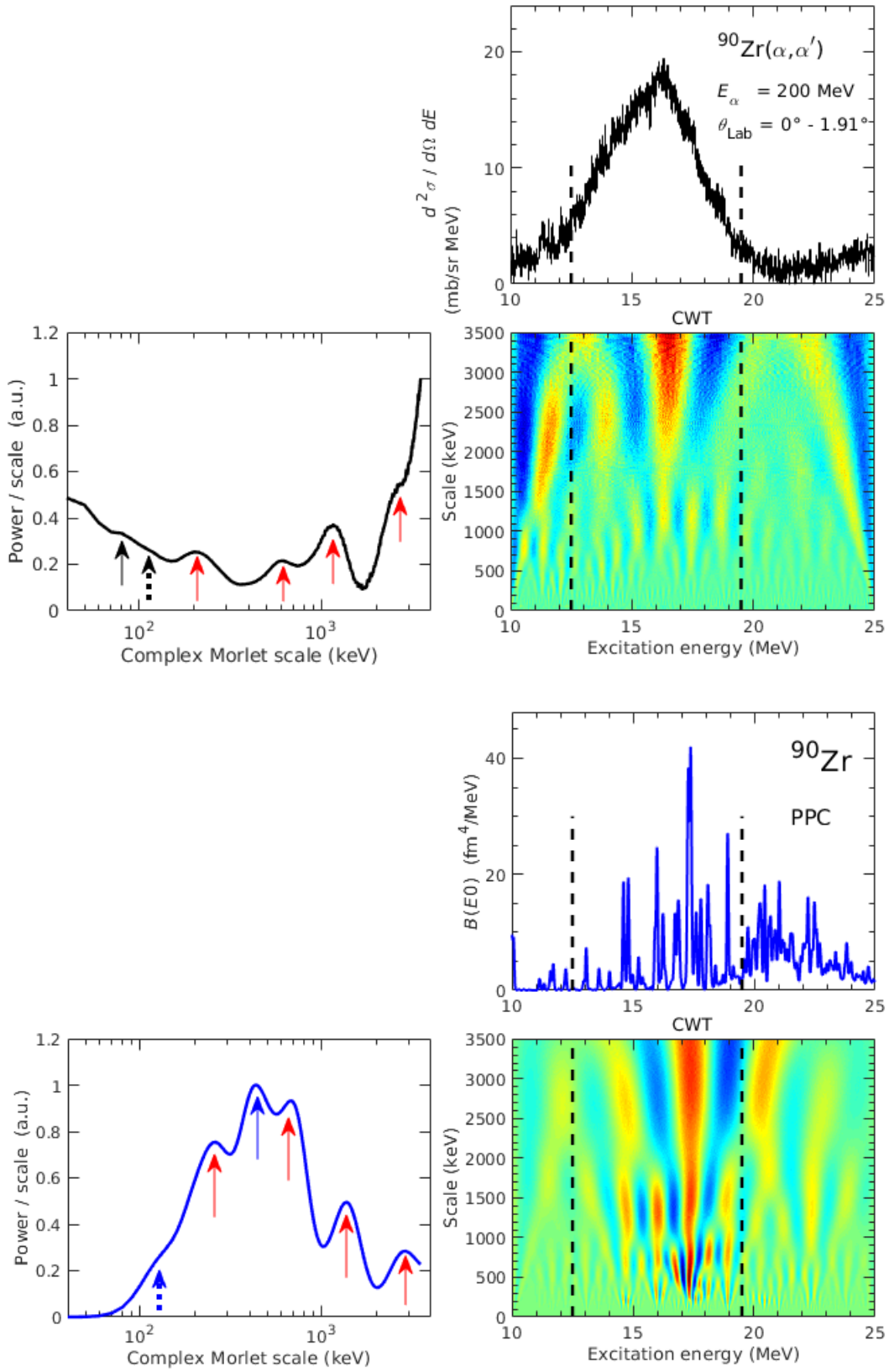

Figure 4.11: Experimental and theoretical CWT analysis for ^{90}Zr between the excitation-energy region of 12.5 - 19.5 MeV. Red arrows indicate the presence of equivalent scales.

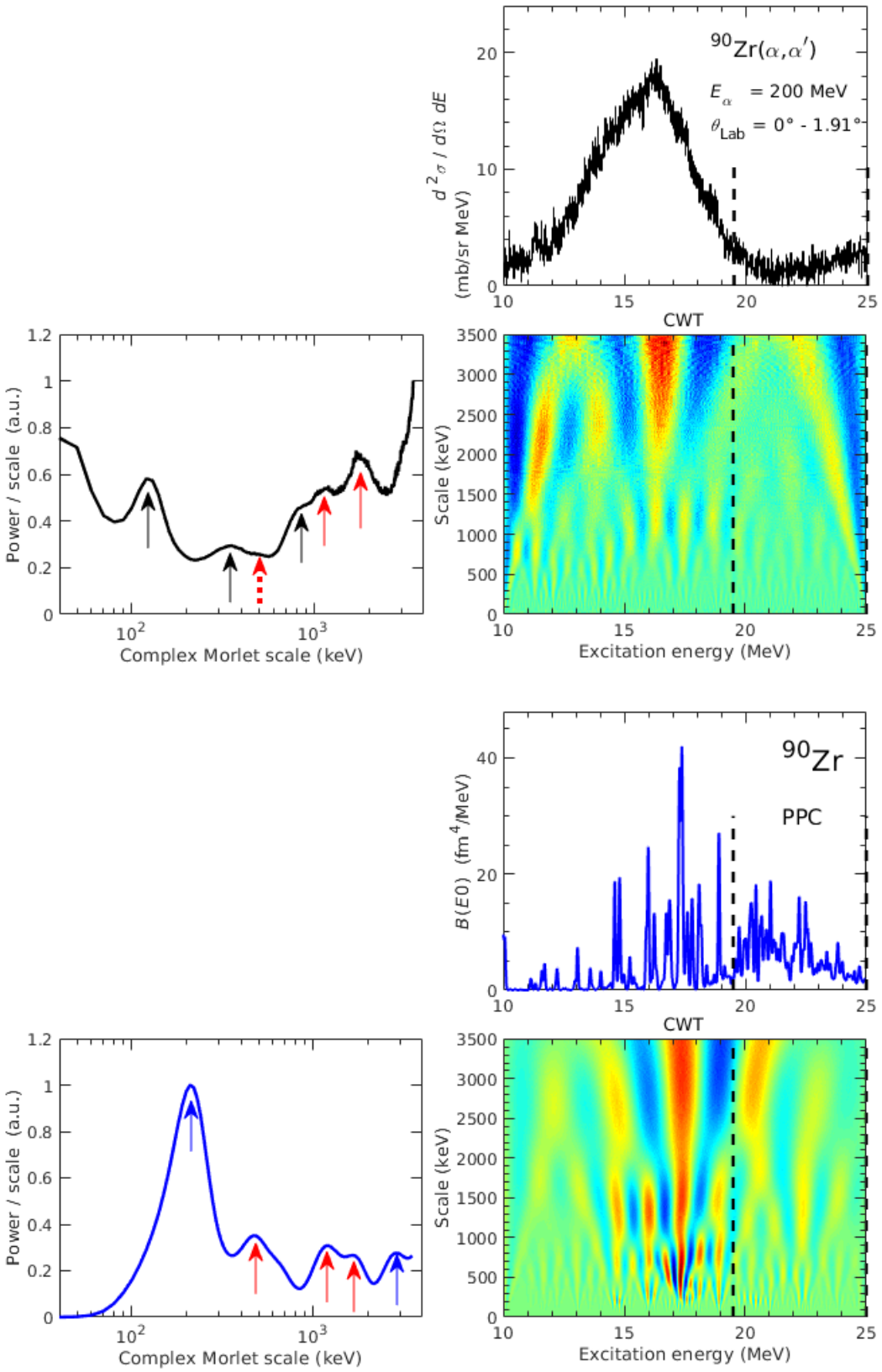

Figure 4.12: Experimental and theoretical CWT analysis for ^{90}Zr between the excitation-energy region of 19.5 - 25 MeV. Red arrows indicate the presence of equivalent scales.

Table 4.3: Characteristic energy scales of the ISGMR for ^{90}Zr: 12.5 - 19.5 MeV. The numbers in red correspond to the red arrows in Fig. 4.11 indicating the corresponding scales.

Scale	Class I		Class II		Class III	
	$\Delta E < 300$ keV		$300 \leq \Delta E \leq 1000$ keV		$\Delta E \geq 1000$ keV	
Experiment	**80**	110 **205**		**600**	**1140**	**2600**
Theory		120 **220**	**440**	**680**	**1370**	**2900**

Table 4.4: Characteristic energy scales for $E0$ strength above the ISGMR for ^{90}Zr: 19.5 - 25 MeV. The numbers in red correspond to the red arrows in Fig. 4.12 indicating the corresponding scales.

Scale	Class I	Class II		Class III		
	$\Delta E < 300$ keV	$300 \leq \Delta E \leq 1000$ keV		$\Delta E \geq 1000$ keV		
Experiment	**120**	**350** 490	**830**	**1140**	**1760**	
Theory	**210**	**480**		**1200**	**1690**	**2860**

4.3 Isoscalar Giant Monopole Resonance in ^{58}Ni

4.3.1 ^{58}Ni ISGMR distribution

In 2006, Nayak et al. [13] obtained the strength distribution of the ISGDR in ^{58}Ni over an excitation-energy range of 10.5 - 49.5 MeV. This was achieved with the (α, α') reaction at $E_\alpha = 386$ MeV at extreme forward scattering angles including 0° in the range $0° < \theta_{\text{lab}} < 8.5°$ using the Grand Raiden spectrometer [13]. As with Gupta et al. [10], a similar Multipole Decomposition Analysis (MDA) was performed by Nayak et al. [13] that allowed for the extraction of the ISGDR and ISGMR strength distributions.

4.3.2 Multipole decomposition and DOS method

An identical MDA to that of ^{90}Zr presented in Chapter 1 was performed for ^{58}Ni at $E_\alpha = 385$ MeV by Nayak et al. [13]. Here, the upper panel of Fig. 1.5 of Ref. [13] displays features very similar to that for ^{90}Zr, which corresponds to the upper panel of Fig. 4.3. Again, there is a deep minimum in the calculated cross section for $L = 0$ at $\theta_{\text{c.m.}} = 2.5°$. This is consistent with diffraction scattering, where the ^{58}Ni nucleus is less than 15% smaller in diameter than ^{90}Zr.

4.3.3 ISGMR ^{58}Ni background subtraction, DOS and DWT

In Section 4.2.3, the DWT background-subtraction technique was shown to be equivalent to the DOS technique for ^{90}Zr. The technique was, therefore, also applied to the present ^{58}Ni data. The results of the DWT background subtraction can be seen in Fig. 4.13, with the approximations and details shown in Fig. 4.14. As was the case for ^{90}Zr, the Biorthogonal 6.8 symmetrical wavelet family was once again used. It was necessary to subtract the non-resonant component at A_{10}.

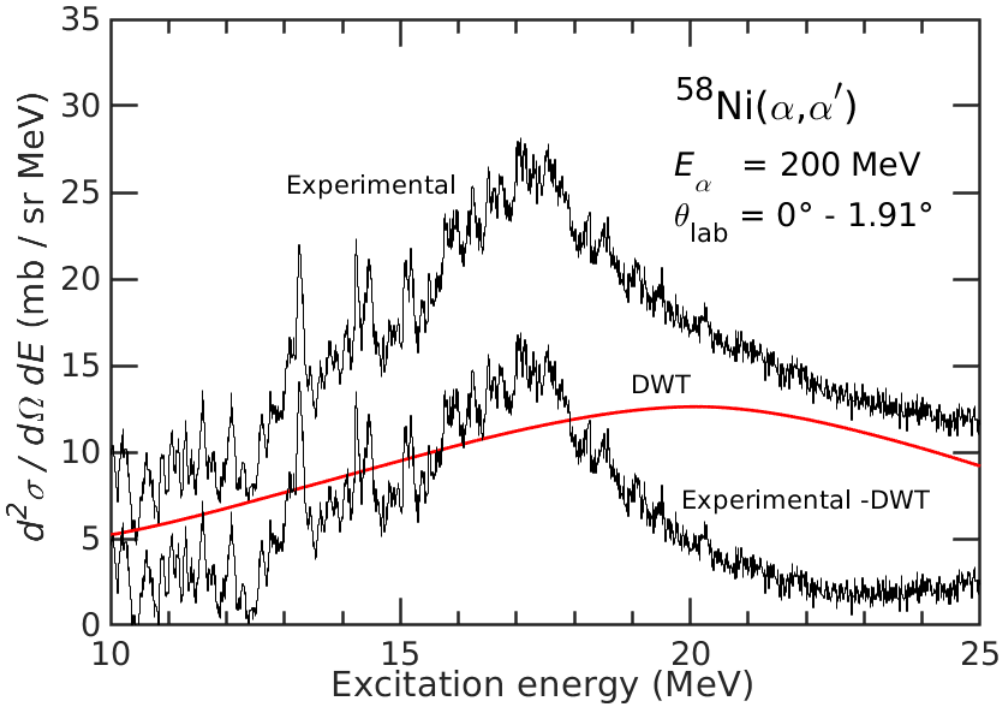

Figure 4.13: DWT background subtraction of the non-resonant component for the ^{58}Ni(α, α') at $E_\alpha = 200$ MeV excitation-energy spectrum. Upper: Spectrum containing background components. Middle: DWT background contribution. Lower: DWT background-subtracted excitation-energy spectrum.

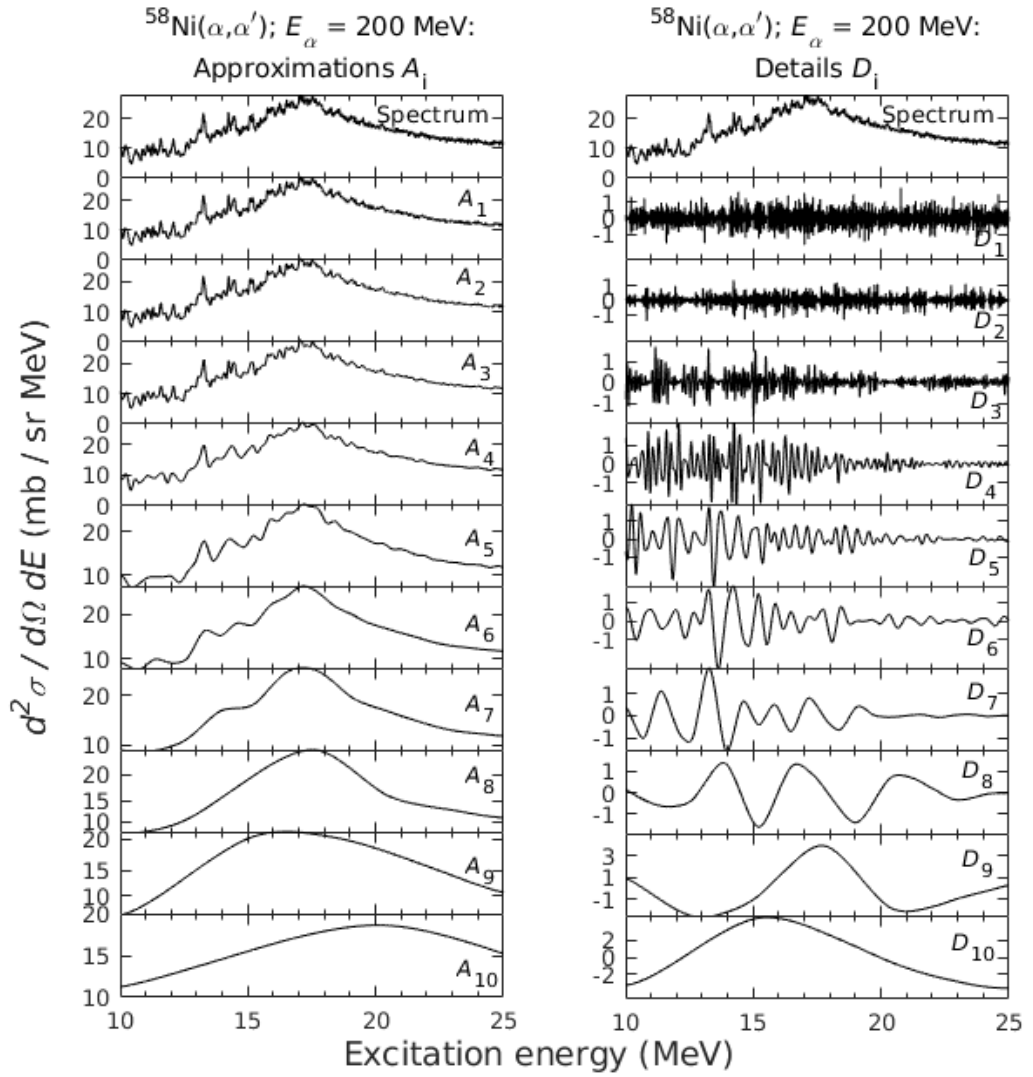

Figure 4.14: Decomposition of the ^{58}Ni(α, α') excitation-energy spectrum at $E_\alpha = 200$ MeV into approximations (A_i) and details (D_i) where i represents the integers from 1 to 10.

4.3.4 ISGMR width and centroid for ^{58}Ni

Following the DWT background-subtraction technique, the centroid energy and width of the ISGMR for ^{58}Ni were extracted using a Lorentzian fitting procedure (see Eq.(2.2)). The result of the fit is illustrated in Fig. 4.15 for ^{58}Ni. Table 4.5 provides the centroids and widths obtained from similar studies conducted for ^{58}Ni as well as the present work.

Table 4.5: Experimentally extracted centroids and widths of the ISGMR for ^{58}Ni.

E_α (MeV)	Centroid (MeV)	Width (MeV)	Reference
200	16.94 ± 0.5	4.0 ± 0.8	Present work
129	17.0	4.0	[11]
240	20.30	4.25	[12]
386	19.9	–	[13]

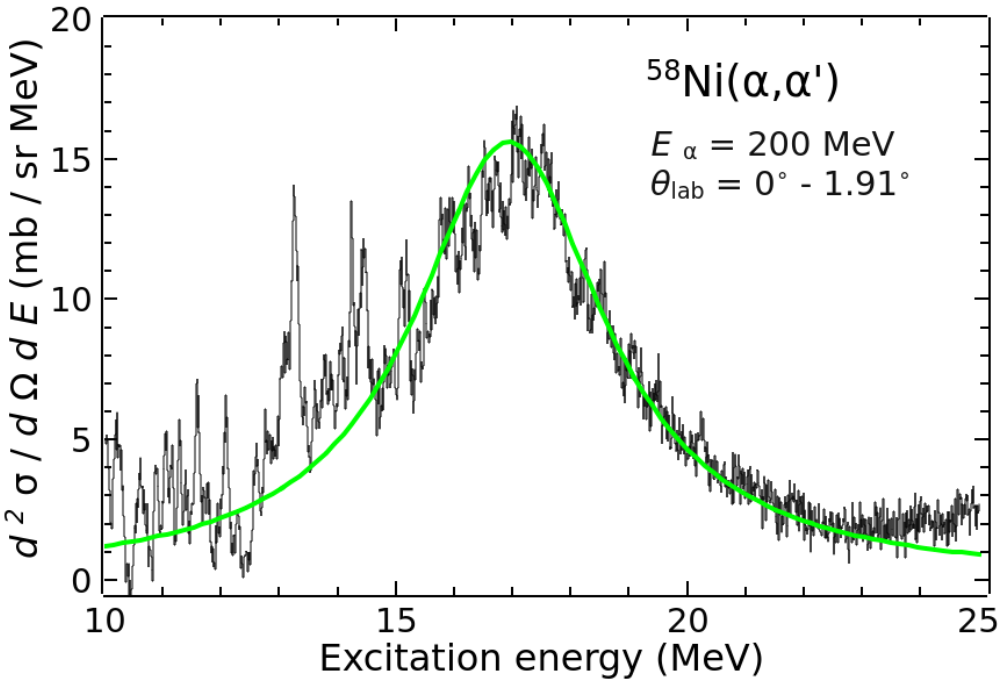

Figure 4.15: DWT background-subtracted excitation-energy spectra for ^{58}Ni showing the application of a Lorentzian curve fit (green).

4.3.5 ^{58}Ni ISGMR fine structure

Again, as a starting point, an overview for ^{58}Ni is presented in Fig. 4.16 of the results obtained from QRPA and PPC calculations (described in Sections 2.6.2 and 2.6.3, respectively), the data of Nayak et al. [13] (lower panel of Fig.

4.16) and, for comparison, the present ^{58}Ni(α, α') scattering data at $E_\alpha = 200$ MeV (upper panel of Fig. 4.16). As for ^{90}Zr, the same f^- Skyrme force is used for the ^{58}Ni calculations. Now the lighter ^{58}Ni exhibits a much broader ISGMR than that of ^{90}Zr noting that it extends over most of the energy bite available at the K600 magnetic spectrometer for the zero-degree setting. As such, a similar CWT analysis was performed for ^{58}Ni, the results of which can be seen in Fig. 4.17. Characteristic energy scales were extracted from the corresponding power spectrum (seen in the left panel of Fig. 4.17). PPC calculations were carried out in the same manner as with ^{90}Zr, the results of which can be seen in the lower panel of Fig. 4.17. The weaker scales are shown with dotted arrows while the stronger scales are shown with continuous arrows in Fig. 4.17.

The characteristic energy scales were extracted. A summary of the extracted scales is presented in Table 4.6. The stronger scales are shown in bold.

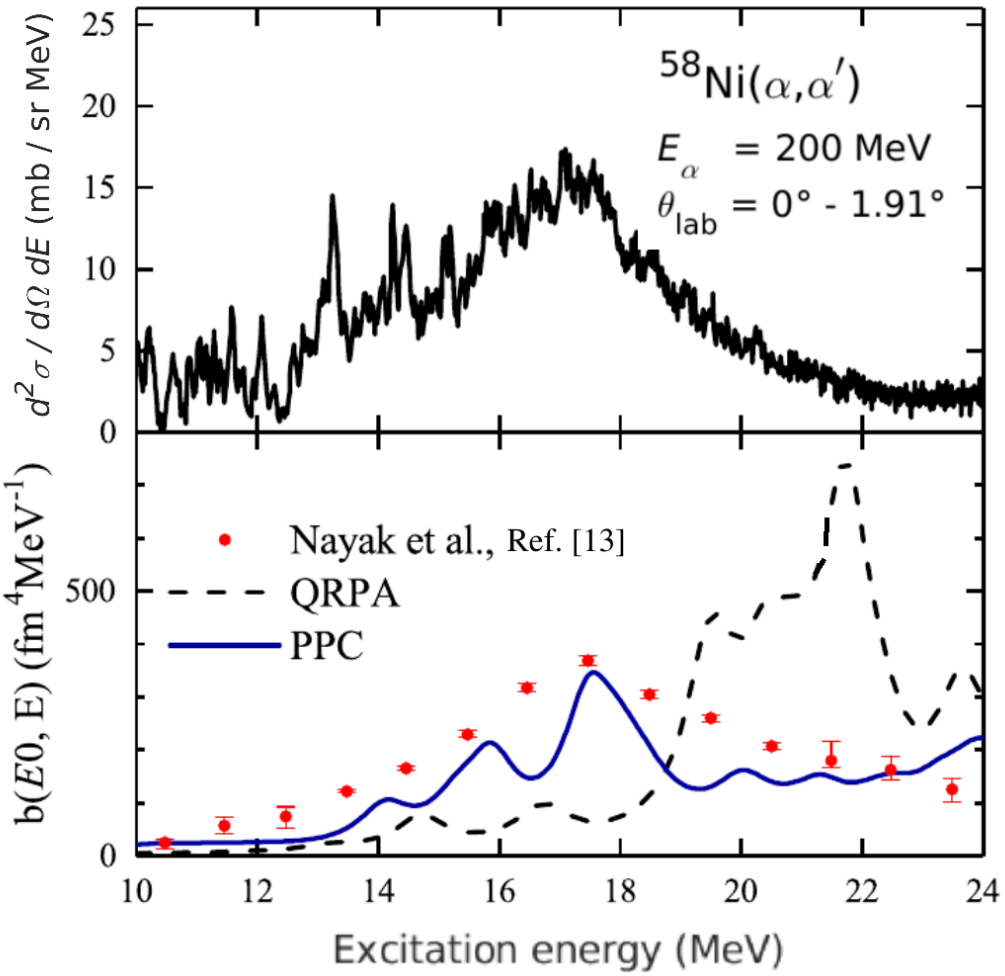

Figure 4.16: *Upper*: Experimental excitation-energy spectra for ^{58}Ni at E_α = 200 MeV. *Lower*: Solid line represents PPC strength distribution, filled circles represent data from Nayak et al. [13], dashed line represents the results of QRPA.

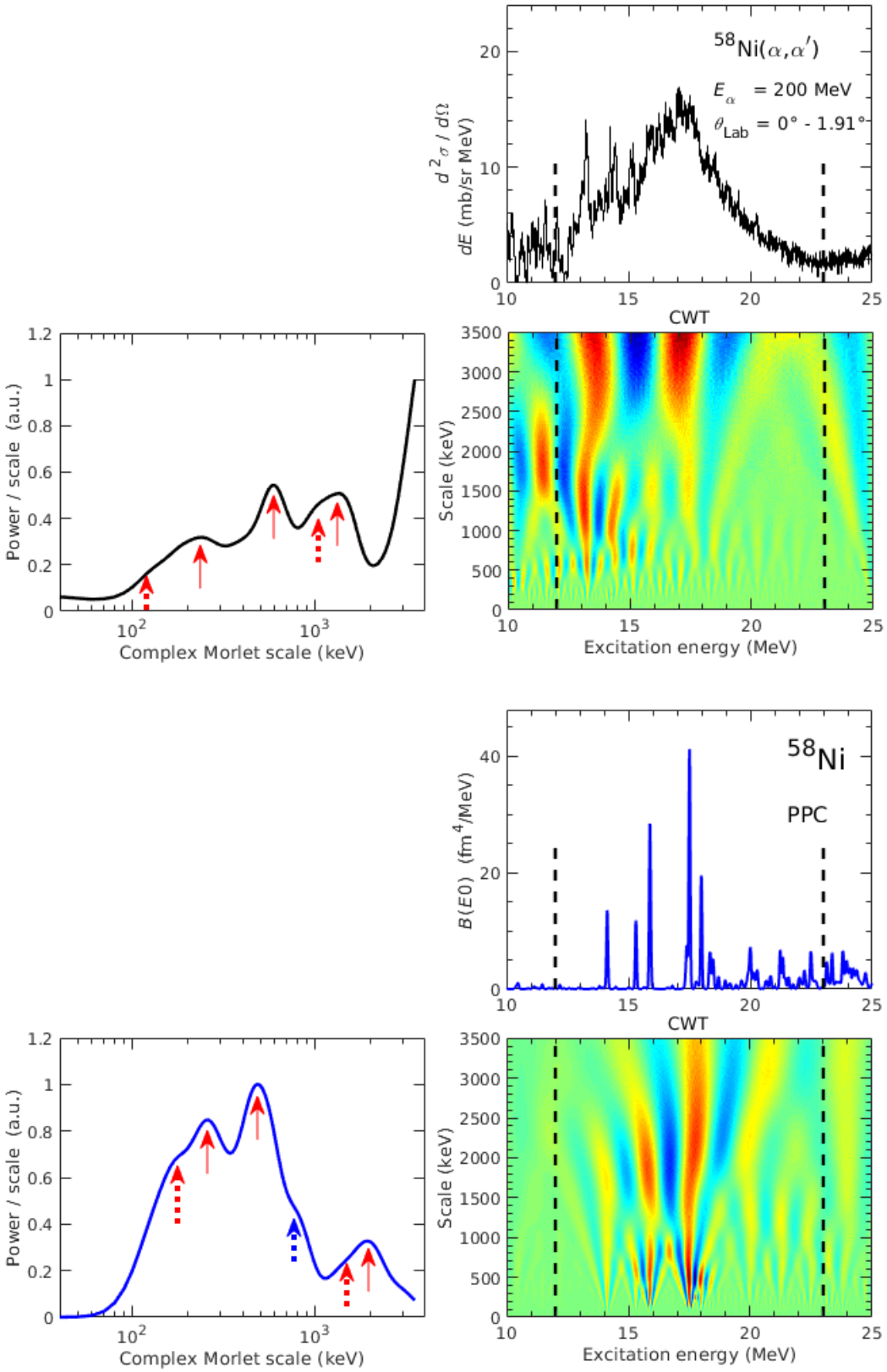

Figure 4.17: Experimental and theoretical CWT analysis for ^{58}Ni between the excitation-energy region of 12 - 23 MeV. Red arrows indicate the presence of equivalent scales.

Table 4.6: Characteristic energy scales of the ISGMR for ^{58}Ni. The numbers in red correspond to the red arrows in Fig. 4.17 indicating the corresponding scales.

Scale	Class I		Class II		Class III	
	$\Delta E < 300$ keV		$300 \leq \Delta E \leq 1000$ keV		$\Delta E \geq 1000$ keV	
Experiment	120	**230**	**590**		1020	**1310**
Theory	180	**260**	**480**	780	1480	**1950**

4.4 Discussion

In order to obtain excitation-energy spectra that are free from instrumental-background contributions, extensive data-extraction and optimisation processes were performed as detailed in Chapter 3. The resulting excitation-energy spectra are presented in Fig. 4.1. These spectra were then converted to double-differential cross sections which are presented in Fig. 4.2. The excitation-energy spectrum for ^{24}Mg shows a severe fragmentation and spreading resulting in clearly defined discrete states. Discrete excited states were used for energy-calibration purposes as detailed in Chapter 3.

The ISGMR distributions for ^{90}Zr and ^{58}Ni, were then studied. Excitation of the ISGMR is strongly scattering-angle dependent. To accurately extract the excitation-energy spectrum for the ISGMR, measurements at different scattering angles are required. DWBA calculations were performed to determine the optimal scattering angle to obtain the highest-possible cross section. As can be seen in the upper panel of Fig. 4.3, DWUCK4 was used to reproduce Fig. 1.2 from Ref. [10]. The DWBA calculations were inserted into Eq. (1.1) and an almost-exact fit up to approximately 8° was determined by varying $a_L(E_x)$, the fractions of the EWSRs. The $a_L(E_x)$ factors obtained from producing the upper panel of Fig. 4.3 were then applied to the same calculation at $E_\alpha = 200$ MeV, the result of which can be seen in the lower panel of Fig. 4.3. Figure 4.3

clearly illustrates that the angle yielding the highest cross section is 0°, which is consistent with the angle at which the measurements were taken. The $L = 0$ multipolarity has a minimum at approximately 3.1°, suggesting that this would be the best angle at which to conduct measurements if a DOS technique were to be used. Owing to lack of measurements at this angle, an alternative to the DOS techniques was validated with the use of published data.

The DWT background-subtraction technique was demonstrated for both nuclei and shown to be consistent with the DOS technique used by Gupta et al. [10]. This type of multipole background subtraction was then performed for both nuclei by first determining the details and approximations needed to decompose the excitation-energy spectra. Spectra for both nuclei were decomposed, and the decompositions were approximated by low-order polynomials in order to identify the non-resonant components of the spectra. As can be seen in Figs. 4.8 and 4.14, A_{10} was chosen and adjusted to the low and high excitation-energies of the ISGMR in both nuclei. Subtraction of A_{10} from the excitation-energy spectra was performed to ensure a pure ISGMR excitation-energy spectrum for both nuclei.

Extraction of the centroid and width of the ISGMR for both nuclei was performed using a Lorentzian curve (see Eq. ((2.2)). The centroid reported for ^{90}Zr is 15.90 MeV, which is consistent with the DWBA calculations performed at $E_{\mathrm{x}} = 16$ MeV and close to that reported by Gupta et al. [10] at 16.55 MeV. Also consistent with Gupta et al. [10], is the width of the ISGMR for ^{90}Zr reported at 4.3 MeV in the present work, while Gupta et al. [10] reported a width of 4.2 MeV. Similarly, extraction of the centroid and width was carried out for ^{58}Ni. Consistencies between the present work and that published by Youngblood et al. [11] exist for the ^{58}Ni nucleus. The present work reports the centroid at 16.94 MeV, while the width is 4.0 MeV. Youngblood et al. [11] reported a centroid of 17.0 MeV and a width of 4.0 MeV. This shows very good correspondence between the present work and published work.

Fine structure, present in both nuclei, was examined by extracting the characteristic energy scales. Comparison of energy scales with PPC theory shows good correspondence for ^{90}Zr as can be seen in Fig. 4.11. Figure 4.12 shows $E0$ strength above the ISGMR region, which is also consistent with PPC theory as can be seen in the lower panel of Fig. 4.12. Similar CWT analysis was performed for ^{58}Ni, which also shows good correspondence between theory and experiment. Extracted energy scales are presented in Tables 4.3, 4.4 and 4.6. Strong scales are seen in bold, while the others are weaker energy scales. The extracted scales in Class I for the experimental spectrum for ^{90}Zr are close to the energy resolution of 70 keV. Since the complex Morlet scale is a length-wise scale and the energy resolution is a width-wise scale, to accurately compare scales, the length scale is divided by two. Experimental energy-resolution for ^{90}Zr is, therefore, 100 keV while for ^{58}Ni it is 115 keV.

Detailed comparisons can be made between the scales obtained from the measured excitation-energy spectra and the corresponding PPC theoretical predictions.

^{90}Zr ISGMR region E_x = 12.5 - 19.5 MeV, referring to Fig. 4.11 and Table 4.3
There is a remarkable correspondence between the energy scales identified in the experimental power spectrum shown by vertical red arrows (upper left panel of Fig. 4.11) and the corresponding scales identified in the PPC calculations (lower left panel of Fig. 4.11). These scale values (also in red) are entered into Table 4.3 as Class I, II, or III scales with corresponding scales in vertical alignment. Only one strong PPC Class II scale at 440 keV has no experimental counterpart.

^{90}Zr region E_x = 19.5 - 25 MeV, referring to Fig. 4.12 and Table 4.4
Immediately noticeable is that a Class III scale appearing in the ISGMR region just over 1000 keV has broken up into two scales between 1000 and 2000 keV, which are quite distinct in the higher excitation-energy region in both experimental and PPC power spectra (left panel of Fig. 4.12). The strong

scale just over 500 keV in the PPC power spectrum has a weak counterpart in the experimental power spectrum. Additionally, there are two very strong Class I scales in both the experimental and PPC power spectra in the region from 100 to 200 keV that might share an association. Again, corresponding Class I, II, and III scales are shown in vertical alignment in Table 4.4.

^{58}Ni region E_x = 12 - 23 MeV, referring to Fig. 4.17 and Table 4.6

There appears to be two close scales in the region from 1000 to 2000 keV that are present in both the experimental and PPC power spectra. All of these scales are identified in vertical alignment in Table 4.6. Only one weak PPC scale at about 780 keV has no obvious experimental counterpart.

In summary there is excellent agreement between experimentally determined scales in the ISGMR region and those from PPC calculations. Also, there is a noticeable difference in scales for the region above the ISGMR in ^{90}Zr and within the ISGMR region.

Chapter 5

Conclusions

Intensive offline data-extraction and optimisation procedures lead to obtaining position-accurate spectra for ^{24}Mg, ^{58}Ni and ^{90}Zr. These data were then converted to double-differential cross sections. A DWT background-subtraction procedure was performed to eliminate other multipole contributions to the excitation-energy spectra. This technique was validated against the well-known DOS technique and was shown to have excellent correspondence for ^{90}Zr(α, α') at $E_\alpha = 385$ MeV. The DWT background-subtraction technique was then applied to the present data of ^{90}Zr and ^{58}Ni.

Centroids and widths of the ISGMR for each nucleus were extracted using a Lorentizian fitting procedure. Good correspondence between the present work and previous values was found.

Continuous Wavelet Transforms were applied to the data to extract the characteristic energy scales. The scales extracted showed good correspondence with the Phonon-Phonon Coupling theoretical model in the excitation energy region of the ISGMR. In addition, extra $E0$ strength above the ^{90}Zr ISGMR predicted by the PPC model also has good correspondence with the measured experimental data. As such, the predominant damping mechanism for the ISGMR in ^{90}Zr and ^{58}Ni can be attributed to the coupling between 1p-1h and

2p-2h excitations. This is quite reasonable since in the excitation-energy region of the ISGMR, there is a high density of 2p-2h configurations, with the same spin and parity as the 1p-1h giant-resonance configuration [17]. This is represented by the term $\Gamma^{\downarrow}$ in Eq. (2.1). Such a finding should be contrasted with the systematics of fine structure associated with the ISGQR where the main mechanism is owing to coupling to low-lying surface vibrations [49] and with the IVGDR where Landau damping ($\Gamma^{\uparrow}$ in Eq. (2.1)) plays the major role [26].

The calculated inelastic-scattering (α, α') cross sections indicate that a DOS technique can be used for the present experimental data should additional (α, α') data become available between $\theta_{\rm lab}$ = 3° - 4° from a future experiment.

References

[1] M. N. Harakeh and A. van der Woude. *Giant resonances: Fundamental High-Frequency Modes of Nuclear Excitation.*, volume 24. Oxford Studies in Nuclear Physics. Oxford: Oxford University Press, 2001.

[2] S. Olorunfunmi. *Investigation of the isoscalar giant monopole resonance as a function of neutron excess in the* $^{42,44,48}Ca$ *isotope chain*, 2016. PhD Research Proposal to University of the Witwatersrand.

[3] L. M. Donaldson. *Effect of deformation on the broad and fine structure of the Isovector Giant Dipole Resonance in* $^{142-150}Nd$ *and* ^{152}Sm. PhD thesis, University of the Witwatersrand, 2016.

[4] M. N. Harakeh, K. van der Borg, T. Ishimatsu, H. P. Morsch, A. van der Woude, and F. E. Bertrand. *Phys. Rev. Lett.*, 38(13):676, 1977.

[5] D. H. Youngblood, C. M. Rozsa, J. M. Moss, D. R. Brown, and J. D. Bronson. *Phys. Rev. Lett.*, 39(19):1188, 1977.

[6] P. Gleissl, M. Brack, J. Meyer, and P. Quentin. *Ann. Phys.*, 197(2):205–264, 1990.

[7] D. C. Patel. *A Study of the Isoscalar Giant Monopole Resonance: The Role of Symmetry Energy in Nuclear Incompressibility in the Open-Shell Nuclei.* Springer Theses, 2015.

[8] J. Speth. *Electric and Magnetic Giant Resonances in Nuclei.*, volume 7. World Scientific Publishing Co. Pte. Ltd., Singapore, 1991.

[9] D. H. Youngblood, Y.-W. Lui, Krishichayan, J. Button, M. R. Anders, M. L. Gorelik, M. H. Urin, and S. Shlomo. *Phys. Rev. C*, 88(2):021301, 2013.

[10] Y. K. Gupta, U. Garg, K. B. Howard, J. T. Matta, M. Şenyiğit, M. Itoh, S. Ando, T. Aoki, A. Uchiyama, S. Adachi, et al. *Phys. Lett. B*, 760:482–485, 2016.

[11] D. H. Youngblood and Y.-W. Lui. *Phys. Rev. C*, 44(5):1878, 1991.

[12] Y. W. Lui, H. L. Clark, and D. H. Youngblood. *Phys. Rev. C*, 61(6):067307, 2000.

[13] B. K. Nayak, U. Garg, M. Hedden, M. Koss, T. Li, Y. Liu, P. V. Madhusudhana Rao, S. Zhu, M. Itoh, H. Sakaguchi, H. Takeda, M. Uchida, Y. Yasuda, M. Yosoi, H. Fujimura, M. Fujiwara, K. Hara, T. Kawabata, H. Akimune, and M. N. Harakeh. *Phys. Lett. B*, 637(1-2):43–47, 2006.

[14] F. E. Bertrand. *Nucl. Phys. A*, 354(1-2):129–156, 1981.

[15] H. Ejiri and H. Toki. *Nucleon-Hadron Many Body Systems: From Hadron-Meson to Quark-Lepton Nuclear Physics.* Number 22. Oxford University Press Inc., New York,, 1999.

[16] E. Lipparini and S. Stringari. *Phys. Rep.*, 175(3-4):103–261, 1989.

[17] S. Drozdz, S. Nishizaki, J. Speth, and J. Wambach. *Phys. Rep.*, 197(1):1–65, 1990.

[18] F. E. Bertrand. *Annu. Rev. Nucl. Sci.*, 26:457, 1976.

[19] A. van der Woude. *Prog. Part. Nucl. Phys.*, 18:217–293, 1987.

[20] G Colò. *Phys. of Part. Nucl.*, 39(2):286–305, 2008.

[21] A. Mukherjee. *Phys. Rev. C*, 79(4):045811, 2009.

[22] M. N. Harakeh, B. van Heyst, K. van der Borg, and A. van der Woude. *Nucl. Phys. A*, 327:373, 1979.

[23] D. H. Youngblood, H. L. Clark, and Y. W. Lui. *Phys. Rev. Lett.*, 82:691, 1999.

[24] D. H. Youngblood, H. L. Clark, and Y. W. Lui. *Nucl. Phys. A*, 649(1-4):49–56, 1999.

[25] U. Kneissl, H. H. Pitz, and A. Zilges. *Prog. Part. Nucl. Phys.*, 37:349–433, 1996.

[26] M. Jingo. *Fine structure of the Isovector Giant Dipole Resonance: A survey with the (p,p′) reaction at zero degrees.* PhD thesis, University of the Witwatersrand, 2014.

[27] G. Duhamel, M. Buenerd, P. De Saintignon, J. Chauvin, D. Lebrun, Ph. Martin, and G. Perrin. *Phys. Rev. C*, 38(6):2509, 1988.

[28] U. Garg and G. Colò. *Prog. Part. Nucl. Phys.*, 2018.

[29] J. Piekarewicz. *Phys. Rev. C*, 66(3):034305, 2002.

[30] H. J. Lu, S. Brandenburg, R. De Leo, M. N. Harakeh, T. D. Poelhekken, and A. van der Woude. *Phys. Rev. C*, 33(3):1116, 1986.

[31] D. H. Youngblood, P. Bogucki, J. D. Bronson, U. Garg, Y. W. Lui, and C. M. Rozsa. *Phys. Rev. C*, 23:1997, 1981.

[32] R. Bass. *IAEA - INIS Repository*, 11, 1980.

[33] D. H. Youngblood, H. L. Clark, and Y. W. Lui. *Phys. Rev. Lett.*, 76:1429, 1996.

[34] V. A. Madsen and W. Tobocman. *Phys. Rev.*, 139:B864, 1965.

[35] T. Kawabata, T. Adachi, M. Fujiwara, K. Hatanaka, Y. Ishiguro, M. Itoh, Y. Maeda, H. Matsubara, H. Miyasako, and Y. Nozawa. *Prog. Theor. Phys. Supp.*, 196:198–202, 2012.

[36] N. Van Giai, C. Stoyanov, and V. V. Voronov. *Phys. Rev. C*, 57(3):1204, 1998.

[37] A. P. Severyukhin, N. N. Arsenyev, and N. Pietralla. *Phys. Rev. C*, 86(2):024311, 2012.

[38] J. Terasaki, J. Engel, M. Bender, J. Dobaczewski, W. Nazarewicz, and M. Stoitsov. *Phys. Rev. C*, 71(3):034310, 2005.

[39] A. P. Severyukhin, V. V. Voronov, and N. Van Giai. *Phys. Rev. C*, 77(2):024322, 2008.

[40] P. Ring and P. Schuck. Springer Science & Business Media, 2004.

[41] N. Van Giai and H. Sagawa. *Phys. Lett. B*, 106(5):379–382, 1981.

[42] V. G. Soloviev. *Theory of Atomic Nuclei, Quasi-particle and Phonons.* CRC Press, 1992.

[43] A. P. Severyukhin, V. V. Voronov, and N. Van Giai. *Eur. Phys. J. A*, 22(3):397–403, 2004.

[44] P. D. Kunz. *Department of Physics, University of Colorado*, 1977.

[45] C. O. Kureba. *Fine structure of the Isoscalar Giant Quadrupole Resonance and 2^+ level densities in spherical to deformed nuclei across the isotope*

chain ^{142,144,146,148,150}*Nd using the (p,p′) reaction.* PhD thesis, University of the Witwatersrand, 2014.

[46] P. F. Bortignon. *IAEA - INIS Repository*, 25, 1993.

[47] D. Lacroix, A. Mai, P. von Neumann-Cosel, A. Richter, and J. Wambach. *Phys. Lett. B*, 479(1-3):15–20, 2000.

[48] I. Usman, Z. Buthelezi, J. Carter, G. R. J. Cooper, R. W. Fearick, S. V. Förtsch, H. Fujita, Y. Fujita, Y. Kalmykov, P. von Neumann-Cosel, R. Neveling, P. Papakonstantinou, A. Richter, R. Roth, A. Shevchenko, E. Sideras-Haddad, and F. D. Smit. *Phys. Lett. B*, 698(3):191–195, 2011.

[49] A. Shevchenko, O. Burda, J. Carter, G. R. J. Cooper, R. W. Fearick, S. V. Förtsch, H. Fujita, Y. Fujita, Y. Kalmykov, D. Lacroix, J. J. Lawrie, P. von Neumann-Cosel, R. Neveling, V. Yu. Ponomarev, A. Richter, E. Sideras-Haddad, F. D. Smit, and J. Wambach. *Phys. Rev. C*, 79(4):044305, 2009.

[50] Y. Kalmykov, T. Adachi, G. P. A. Berg, H. Fujita, K. Fujita, Y. Fujita, K. Hatanaka, J. Kamiya, K. Nakanishi, P. von Neumann-Cosel, V. Yu. Ponomarev, A. Richter, N. Sakamoto, Y. Sakemi, A. Shevchenko, Y. Shimbara, Y. Shimizu, F. D. Smit, T. Wakasa, J. Wambach, and M. Yosoi. *Phys. Rev. Lett.*, 96(1):012502, 2006.

[51] A. Tamii, T. Adachi, J. Carter, M. Dozono, H. Fujita, Y. Fujita, K. Hatanaka, H. Hashimoto, T. Kaneda, M. Itoh, T. Kawabata, H. Matsubara, K. Nakanishi, P. von Neumann-Cosel, H. Okamura, A. Perez, I. Poltoratska, V. Yu. Ponomarev, L. Popescu, A. Richter, B. Rubio, H. Sakaguchi, Y. Sakemi, Y. Sasamoto, Y. Shimbara, Y. Shimizu, F. D. Smit, Y. Tameshige, M. Yosoi, J. Zenihiro, and K. Zimmer. *Nucl. Phys.*, 788:53c, 2007.

[52] P. von Neumann-Cosel, F. Neumeyer, S. Nishizaki, V. Yu. Ponomarev, C. Rangacharyulu, B. Reitz, A. Richter, G. Schrieder, D. I. Sober, T. Waindzoch, and J. Wambach. *Phys. Rev. Lett.*, 82:1105, 1999.

[53] I. T. Usman. *Fine Structure of the Isoscalar Giant Monopole Resonance in ^{208}Pb, ^{90}Zr, ^{58}Ni and ^{40}Ca, using alpha scattering at zero degrees*, 2014. Proposal to iThemba LABS PAC.

[54] I. Poltoratska, R. W. Fearick, A. M. Krumbholz, E. Litvinova, H. Matsubara, P. von Neumann-Cosel, V. Yu. Ponomarev, A. Richter, and A. Tamii. *Phys. Rev. C*, 89(5):054322, 2014.

[55] A. Graps. *IEEE Comput. Sci. Eng.*, 2(2):50–61, 1995.

[56] I. Daubechies. *Ten lectures on wavelets*, volume 61. Siam, 1992.

[57] A. Shevchenko. *IAEA - INIS Repository*, 11, 2005.

[58] I. T. Usman. *Fragmentation of the Isoscalar Giant Quadrupole Resonance in low mass $12 \leq A \leq 40$ nuclei and 2^+ level density in ^{40}Ca from high energy-resolution (p,p′) scattering at 200 MeV*. PhD thesis, University of the Witwatersrand, 2010.

[59] A. Shevchenko, J. Carter, G. R. J. Cooper, R. W. Fearick, Y. Kalmykov, P. von Neumann-Cosel, V. Yu. Ponomarev, A. Richter, I. T. Usman, and J. Wambach. *Phys. Rev. C*, 77(2):024302, 2008.

[60] J. C. van den Berg. *Wavelets in Physics*. Cambridge University Press, 2004.

[61] R. Neveling, H. Fujita, F. D. Smit, T. Adachi, G. P. A. Berg, E. Z. Buthelezi, J. Carter, J. L. Conradie, M. Couder, R. W. Fearick, S. V. Förtsch, D. T. Fourie, Y. Fujita, J. Görres, K. Hatanaka, M. Jingo, A. M. Krumbholz, C. O. Kureba, J. P. Mira, S. H. T. Murray, P. von Neumann-

Cosel, S. O'Brien, P. Papka, I. Poltoratska, A. Richter, E. Sideras-Haddad, J. A. Swartz, A. Tamii, Usman I. T., and J. J. van Zyl. *Nucl. Instr. Methods A*, 654(1):29–39, 2011.

[62] R. Neveling, F. D. Smit, H. Fujita, P. Adsley, K. C. W. Li, J. W. Brummer, D. J. Marn-Lambrri, and R. T. Newman. *Guide to the K600 Magnetic Spectrometer*, 2017.

[63] A. Tamii, Y. Fujita, H. Matsubara, T. Adachi, J. Carter, M. Dozono, H. Fujita, K. Fujita, H. Hashimoto, K. Hatanaka, T. Itahashi, M. Itoh, T. Kawabata, K. Nakanishi, S. Ninomiya, A. B. Perez-Cerdan, L. Popescu, B. Rubio, T. Saito, H. Sakaguchi, Y. Sakemi, Y. Sasamoto, Y. Shimbara, Y. Shimizu, F. D. Smit, Y. Tameshige, M. Yosoi, and J. Zenhiro. *Nucl. Instrum. Methods Phys. Res., Sect. A*, 605(3):326–338, 2009.

[64] G. P. A. Berg. In *Nuclear Reaction Dynamics Of Nucleon-hadron Many Body System: From Nucleon Spins And Mesons In Nuclei To Quark Lepton Nuclear Physics-Proceedings Of The 14th RCNP Osaka International Symposium*, page 141. Indiana University Cyclotron Facility, Bloomington, Indiana 47408, 1996.

[65] J. Song, L. Wang, A. Zibart, and C. Koch. *Metals*, 2(4):450–477, 2012.

[66] D. Roundy, C. R. Krenn, M. L. Cohen, and J. W. Morris Jr. *Philosophical Magazine A*, 81(7):1725–1747, 2001.

[67] S. Ritt, P. Amaudruz, and K. Olchanski. The midas data acquisition system. *Midas online:¡ https://midas. psi*, 1997.

[68] A. Stolarz. *J. Radioanal. Nucl. Chem.*, 299(2):913–931, 2014.

[69] Y. Fujita, H. Fujita, G. P. A. Berg, K. Harada, K. Hatanaka, M. Kawabata, T. Noro, H. Sakaguchi, T. Shinada, and Y. Shimbara. *Journal of the Mass Spectrometry Society of Japan*, 48(5):306–311, 2000.

[70] B. L. Cohen. *Rev. Sci. Instrum.*, 30(6):415–418, 1959.

[71] A. Shevchenko, O. Burda, Y. Kalmykov, P. von Neumann-Cosel, V. Yu. Ponomarev, A. Richter, J. Wambach, J. Carter, R. W. Fearick, S. V. Förtsch, J. J. Lawrie, S. Mukherjee, R. T. Newman, F. D. Smit, Y. Fujita, and D. Lacroix. *Verh. Dtsch. Phys. Ges.*, 38(3):79, 2003.

[72] W. Bertozzi, M. V. Hynes, C. P. Sargent, C. Creswell, P. C. Dunn, A. Hirsch, M. Leitch, B. Norum, F. N. Rad, and T. Sasanuma. *Nucl. Instrum. Methods Phys.*, 141(3):457–476, 1977.

[73] A. Huie, D. Beavis, S. Y. Fung, W. Gorn, D. Keane, J. J. Lu, R. T. Poe, B. C. Shen, and G. Van Dalen. *Phys. Rev. C*, 27(1):439, 1983.

[74] C. Wheldon. *Derivations for two-body kinematics (both relativistic and non-relativistic)*, 2018.

[75] A. Wang, G. Audi, A. H. Wapstra, F. G. Kondev, M. MacCormick, X. Xu, and B. Pfeiffer. *Chin. Phys. C*, 36:1603, 2012.

[76] T. Kawabata. In *AIP Conference Proceedings*, volume 1235, pages 207–211. AIP, 2010.

[77] T. Kawabata, T. Adachi, M. Fujiwara, K. Hatanaka, Y. Ishiguro, M. Itoh, Y. Maeda, H. Matsubara, H. Miyasako, Y. Nozawa, T. Saito, S. Sakaguchi, Y. Sasamot, Y. Shimizu, T. Takahashi, A. Tamii, S. Terashima, H. Tokieda, N. Tomida, T. Uesaka, M. Uchida, Y. Yasuda, N. Yokota, H. P. Yoshida, and J. Zenihiro. In *AIP Conference Proceedings*, volume 1355, pages 194–199. AIP, 2011.

[78] M. Uchida, H. Sakaguchi, M. Itoh, M. Yosoi, T. Kawabata, Y. Yasuda, H. Takeda, T. Murakami, S. Terashima, S. Kishi, U. Garg, P. Boutachkov, M. Hedden, B. Kharraja, M. Koss, B. K. Nayak, S. Zhu, M. Fujiwara, H. Fujimura, H. P. Yoshida, K. Hara, H. Akimune, and M. N. Harakeh.

Phys. Rev. C, 69(5):051301, 2004.

[79] B. Bonin, N. Alamanos, B. Berthier, G. Bruge, H. Faraggi, J. C. Lugol, W. Mittig, L. Papineau, A. I. Yavin, J. Arvieux, L. Farvacque, and M. Buenerd. *Nucl. Phys. A*, 445(3):381–407, 1985.

[80] A. Kumar, S. Kailas, S. Rathi, and K. Mahata. *Nucl. Phys. A*, 776(3-4):105–117, 2006.

[81] S. Kailas. *OM-Alpha, Nuclear Physics Division*, BARC, Mumbai, 2002.

[82] *https://www.iaea.org/resources/databases/inis*. Accessed: 2018-03-20.

[83] *https://www.nndc.bnl.gov/ensdf/*. Accessed: 2019-03-12.

[84] T. Benkert, K. Franke, D. Pozitron, and R. Standish. Scidavis 1. *D005 (Free Software Foundation, Inc: 51 Franklin Street, Fifth Floor, Boston, MA 02110-1301 USA)*, 2014.

[85] Y. K. Gupta, K. B. Howard, U. Garg, J. T. Matta, M. Şenyiğit, M. Itoh, S. Ando, T. Aoki, A. Uchiyama, S. Adachi, M. Fujiwara, C. Iwamoto, A. Tammi, H. Akimune, C. Kadono, Y. Matsuda, T. Nakahara, T. Furuno, T. Kawabata, M. Tsumura, M. N. Harakeh, and N. Kalantar-Nayestanaki. *Phys. Rev. C*, 97(6):064323, 2018.

[86] MATLAB. *version 9.4.0 (R2018a)*. The MathWorks Inc., Natick, Massachusetts, 2018.

[87] D. Lagoutte, J. C. Cerisier, J. L. Plagnaud, J. P. Villain, and B. Forget. *J. Atmos. Terr. Phys.*, 54(10):1283–1293, 1992.